MODELLING AND CORRECTION OF SCATTER IN A SWITCHED SOURCE MULTI-RING DETECTOR X-RAY CT MACHINE

A thesis submitted to the University of Manchester
for the degree of Doctor of Philosophy
in the Faculty of Engineering and Physical Sciences

2011

Nicola Wadeson
School of Mathematics

Contents

Word count 22420

List of Tables

List of Figures

The University of Manchester

Nicola Wadeson
Doctor of Philosophy
Modelling and Correction of Scatter in a Switched Source Multi-Ring Detector X-ray CT machine
June 30, 2011

The RTT80 cone beam x-ray computed tomography system, developed by Rapiscan Systems Ltd, uses switched x-ray sources and fixed offset detector rings to remove the time consuming mechanical rotations of earlier imaging systems. This system produces three-dimensional images in real time. A Geant4 Monte Carlo simulation has been developed to investigate scattered radiation in the uncollimated detector machine, showing high levels of scatter behind highly attenuating objects.

A new scatter correction method is proposed which estimates scatter to each detector, in each projection, from 1cm^3 voxels of the computerised object. The scatter distributions from different materials are pre-determined using a Geant4 Monte Carlo simulation. The intensity of scatter from each voxel is based on measured data. The method is applied to two simulated test objects, a water box simulated with a monoenergetic input spectrum and a test suitcase simulated with a polyenergetic spectrum. The test suitcase is broken down into separate components to analyse the method further. The results show that the method performs well for low attenuating objects, but the results are sensitive to the intensity values. However, the method provides a good basis for a scatter correction method.

Declaration

No portion of the work referred to in this thesis has been submitted in support of an application for another degree or qualification of this or any other university or other institute of learning.

Copyright Statement

i. The author of this thesis (including any appendices and/or schedules to this thesis) owns any copyright in it (the "Copyright") and s/he has given The University of Manchester the right to use such Copyright for any administrative, promotional, educational and/or teaching purposes.

ii. Copies of this thesis, either in full or in extracts, may be made **only** in accordance with the regulations of the John Rylands University Library of Manchester. Details of these regulations may be obtained from the Librarian. This page must form part of any such copies made.

iii. The ownership of any patents, designs, trade marks and any and all other intellectual property rights except for the Copyright (the "Intellectual Property Rights") and any reproductions of copyright works, for example graphs and tables ("Reproductions"), which may be described in this thesis, may not be owned by the author and may be owned by third parties. Such Intellectual Property Rights and Reproductions cannot and must not be made available for use without the prior written permission of the owner(s) of the relevant Intellectual Property Rights and/or Reproductions.

iv. Further information on the conditions under which disclosure, publication and exploitation of this thesis, the Copyright and any Intellectual Property Rights and/or Reproductions described in it may take place is available from the Head of the School of Mathematics.

Acknowledgements

First, I would like to thank my supervisor Bill Lionheart for his guidance and patience and for having faith in me. Similarly, thank you to Ed Morton of Rapiscan System Ltd, and to Pete and Dan for answering my emails and providing information when it was needed. A big thank you to all the guys in the office, for their help and encouragement and laughs along the way. Finally, thank you to Vasileios for all his help and support and for feeding me and to my family for supporting me throughout.

Chapter 1

Introduction

In 1917 Johann Radon published a paper proving that material properties of an object could be determined from line integrals through the object. Many years later, in 1971, the first x-ray computed tomography machine, developed by Godfrey Hounsfield was installed for clinical use. Hounsfield and Allan Cormack shared the Nobel Prize in 1979 for their independent studies in developing the algorithms.

Since the first machine was introduced, x-ray CT has developed rapidly. Machines have evolved from slow parallel beam geometries, with a source and detector translated and rotated about the object, to fan beam systems and cone beam systems with helical cone beam trajectories. With developments in computer technology, reconstruction algorithms and detector technology alongside, scanning time has reduced from hours to three-dimensional object reconstruction in real time. This has led to a wide range of applicability, not only in medical science but in many other areas, as a non-destructive testing technique. Some examples are, examining porosity in rocks in the geosciences, airport baggage scanning and examining aircraft parts in the transport industry.

Artifacts arise in a reconstructed image due to factors such as aliasing, partial volume effects, beam hardening and scattered radiation. This thesis focuses on scattered radiation in cone beam CT systems. When an x-ray beam traverses an object it is subjected to physical interactions with atoms of the object material. An x-ray photon may be absorbed or scattered. When radiation is scattered into a detector element

it leads to errors in the reconstructed attenuation coefficients, leading to streaks and cupping artifacts in the image. There is a significant increase in scattered radiation in cone beam imaging systems due to greater object irradiation and subsequently more scattering points. When fixed rings of detectors are employed it is not possible to collimate the detector elements to reduce the scatter signal, as the detectors must be able to record photons from a wide range of angles.

The RTT80 cone beam CT system, developed by Rapiscan System Ltd, uses switched x-ray sources and fixed offset detector rings to remove the time consuming mechanical rotations of earlier imaging systems. This system produces three-dimensional images in real time. With an application in airport baggage scanning it is important to identify low-Z materials in the identification of suspect objects. Since detector collimation is not possible, scatter correction methods are sought to remove scatter from the reconstructed images.

The level of scattered radiation present in an image is dependent on a number of factors such as the material present, the size of the scattering objects and their proximity to the detectors. This thesis investigates scatter in the RTT80 system using a Geant4 Monte Carlo simulation. Furthermore, a new scatter correction method is proposed whereby scatter to each detector in a projection is estimated from 1cm^3 voxels of the computerised object. Angular scatter distributions from voxel samples of different materials are calculated in advance using a Geant4 Monte Carlo simulation. The algorithm is developed for inhomogeneous objects imaged with a polyenergetic beam of x-rays, with intensity values taken from the measured data.

A brief outline of the structure of the thesis is now given.

Chapter 2 provides an overview of x-ray computed tomography and presents the mathematical concepts such as the Radon transform, the Fourier slice theorem and the filtered backprojection algorithm.

Chapter 3 introduces Monte Carlo methods and gives a detailed description of the Geant4 Monte Carlo simulation used throughout the thesis. The three physics processes, photoabsorption and Compton and Rayleigh scatter, are explained in more

detail here.

In Chapter 4 the Geant4 Monte Carlo simulation is utilised to investigate scatter levels in the RTT80 machine. The objects considered are typical to medical and airport baggage scanning applications.

Chapter 5 gives an overview of the scatter correction methods that have been proposed in medical CT, and the new scatter correction algorithm is presented. The Geant4 Monte Carlo simulation of the angular scatter distributions is explained along with other pre-tabulated data required in the method.

In Chapter 6 scatter estimates are obtained, using the algorithm described in Chapter 5, for test objects that have been simulated with the Monte Carlo simulation.

These results are concluded in Chapter 7, and ideas for further work are presented.

Chapter 2

X-ray Computed Tomography

2.1 Introduction

When an x-ray beam traverses an object the initial energy is attenuated by either photoabsorption or scattering processes, that are dependent on the object material. The difference in intensity values measured at the base of the object in transmission tomography, due to different beam paths through the object, forms the basis of x-ray imaging.

Before the introduction of x-ray computed tomography, images were acquired by projecting x-rays, from one view, through an object and recording the final intensity on radiographic film. This provided a superpositional image of the different structures through the depth of the object, leading to low contrast detectability.

Tomography refers to the reconstruction of cross-sections, or slices, of an object from projection data. The idea that a cross-sectional image could be reconstructed from its line integrals was first proposed mathematically by Radon in 1917 [54]. The introduction of x-ray CT as an imaging modality only became possible in the 1970s with increases in computer technology, and the practical implementation is attributed to Hounsfield [31]. X-ray Computed Tomography yields information about the internal structure of the object.

The remainder of this chapter introduces the main concepts of x-ray CT and provides a mathematical description of the problem.

2.2 Generating x-rays

In x-ray CT an x-ray tube produces a polyenergetic beam of x-rays that are transmitted through the imaging object. In an x-ray tube a negatively charged cathode accelerates electrons towards a positively charged anode target. When the electrons bombard the target material, x-rays are created by two processes; Bremsstrahlung and k-shell emission, which results in a polyenergetic x-ray spectrum [59]. Tungsten is a popular target material due to its good conductivity and high melting point. Only approximately 1% of the energy of the electrons is converted into x-rays, with the remainder being released in the form of heat.

Bremsstrahlung radiation is also known as braking radiation. When an electron approaches a target atom the attractive force of the nucleus can cause the electron to change its direction, resulting in deceleration. The electron deceleration results in the loss of kinetic energy in the form of an x-ray photon. The x-rays created by Bremsstrahlung cover a whole range of energies, with a maximum energy equal to the original electron energy. This forms the smooth part of the x-ray spectrum.

K-shell emission produces characteristic x-rays. If the electron has energy greater than the binding energy of the k-shell of the target atom, it may knock out a k-shell electron. The atom is excited and releases the excess energy in the form of x-ray photons. The energies of these x-rays are characteristic of the target material as their energies are the difference between shell binding energies. These characteristic x-rays are the sharp peaks in the x-ray spectrum.

Fig. 2.1 provides an example of an x-ray spectrum created by bombarding a tungsten target with 150keV electrons. The characteristic peaks are clearly visible, and the maximum energy of the x-rays created by Bremsstrahlung is equal to the energy of the incident electrons.

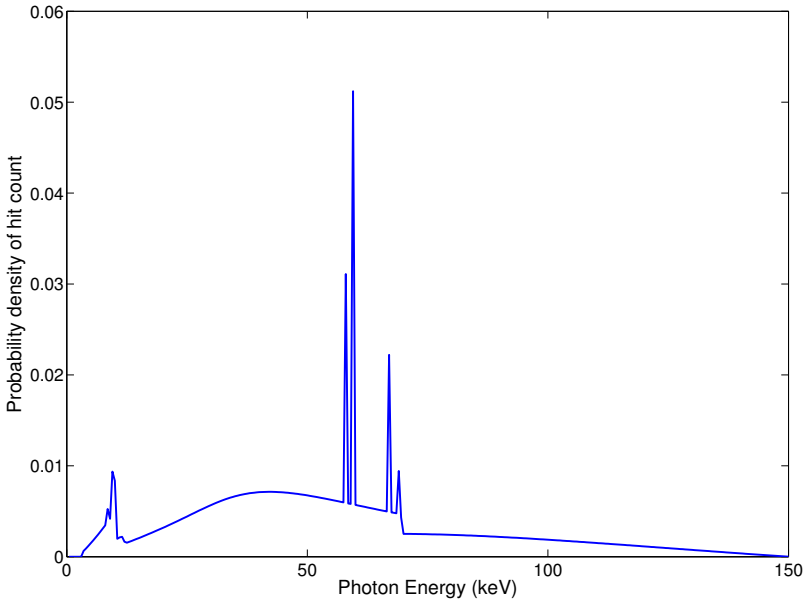

Figure 2.1: 150kVp polyenergetic x-ray spectrum from a tungsten target

2.3 Geometry

There have been many developments in x-ray CT since the first machines were introduced in the early 70s [37]. With developments in computer technology, the resolution of the reconstructed image has improved dramatically, lending itself to many areas of applicability. Changes in the geometry of the x-ray CT machine have been aimed at fast data acquisition, providing more challenges in reconstructing the data.

The first machines were based on parallel data acquisition with one source and one detector being translated and rotated about the object. These machines took a matter of hours to produce images and were impractical. Fan beam imaging system were later developed, allowing a whole projection of measurements to be collected simultaneously. With a rotating source and arc of detectors, or a rotating source and a fixed detector ring, a fan of x-ray beams is projected towards all the detectors at once, leading to significant improvements in acquisition time.

With a desire to decrease scanning time further, and with developments in detector technology, cone beam imaging systems were introduced. With multiple rows of detectors, allowing large areas of an object to be imaged simultaneously, cone beam systems allow faster acquisition. With the introduction of helical cone beam CT,

where the source is considered to have a helical path around the object, complete objects are scanned continuously and scanning time reduced even further.

The most recent developments in CT lead to the scanning of three-dimensional objects and image reconstruction in real time. By implementing a fixed ring of sources and multiple fixed rings of detectors, mechanical rotation is no longer necessary and data acquisition is instant.

2.4 Physics processes

For x-rays of energies 30-160keV considered in this application, the x-rays interact with matter through three processes. These are photoabsorption, Compton scattering and Rayleigh scattering [8].

Photoabsorption is the process by which an x-ray photon collides with an atomic electron of the traversed material and imparts all of its energy to the electron, the photon is completely absorbed. If the photon has sufficient energy it will eject the electron from the atom and may emit low energy x-rays as vacant shells are filled, a process known as fluorescence. Photoabsorption is a material and energy dependent process which decreases with increasing energy.

Compton scattering is an incoherent scattering process whereby an x-ray photon interacts with an electron, which is bound to an atom of the scattering material, and imparts some of its energy to the electron. An x-ray photon is emitted in any direction depending on the amount of energy that was lost in the scattering process. Compton scattering is less probable at low energies and small scattering angles, but is consistent at higher energies where it becomes the dominant process. Since the number of Compton scattering events is dependent upon the number of electrons present in a material, the Compton scattered photons provide information about the electron density of the scattering material.

Rayleigh scattering is a coherent scattering process whereby the x-ray photon scatters from the whole atom. All of the electrons of the atom produce scatter but the scattered amplitudes only add up in phase in the forward direction, therefore

the Rayleigh scattering process is highly forward peaked. Rayleigh scattering is the dominant scattering process at low energies, but decreases as the energy of the x-ray photon increases. The Rayleigh scattered photons provide information about the atomic structure of the scattering material.

2.5 Artifacts

Artifacts appear in the reconstructed image for a number of different reasons[29]. The main contributors are presented here.

Beam hardening is a well known effect which is the result of a polyenergetic input x-ray spectrum. Due to the energy dependence of the photoabsorption process, low energy photons are more likely to be absorbed and therefore the effective energy of the beam changes at different depths of the object. This leads to streaks and cupping artifacts in the image.

Scattered photons may be absorbed in a detector element leading to an increase in the recorded data. If the primary signal is low compared to the scattered signal this similarly leads to streaks and cupping artifacts within a reconstructed image.

The Nyquist sampling theorem states that in order for a signal to be fully reconstructed it must be sampled at twice the highest frequency. Therefore, the highest frequency that can be reconstructed is constrained by the spatial sampling rate of the imaging system. This results in some high frequency components appearing at lower frequencies causing streak artifacts within the reconstructed image.

Partial volume effects occur when a voxel is not fully covered by a structure or contains more than one contrasting structures. The reconstructed attenuation coefficient will appear as an average of the components present.

2.6 Mathematical model

The problem of mathematically obtaining a computerised image of an object from its projection data is known as an inverse problem. The direct problem, where the

object is known, is used to investigate scattered radiation in later chapters using a Monte Carlo simulation. In x-ray CT what we wish to reconstruct is the attenuation coefficient of the object. The attenuation coefficient, in the monoenergetic case, is proportional to the density of the object, and therefore distinguishes between different materials.

2.6.1 Attenuation coefficient

The attenuation coefficient $\mu(x)$ is a measure of how much energy a beam loses at a point $x \in \mathbb{R}^3$, measured in cm^{-1} and is material and energy dependent. It is equivalent to the sum of the attenuation coefficients of each of the interacting physics processes.

$$\mu(x, E) = \mu_p(x, E) + \mu_c(x, E) + \mu_r(x, E). \tag{2.1}$$

where μ_p, μ_c and μ_r are the attenuation coefficients of photoabsorption, Compton and Rayleigh scattering processes respectively and E is incident photon energy. The object is considered to be a three-dimensional distribution of the x-ray attenuation coefficient.

2.6.2 Transport equation

The transport equation governs the movement of photons through matter [6, 17]. Let $I(x, \theta, E)$ be the intensity of particles at a point $x \in \mathbb{R}^3$, moving in a direction $\theta \in S^2$ with energy $E \in [E_1, E_2]$. If $S(x, \theta, \theta', E, E')$ is the portion of particles scattering from θ', E' to θ, E at the point x and $J(x, \theta, E)$ is the intensity of internal sources, then,

$$\theta \cdot \nabla_x I(x, \theta, E) + \mu(x, E) I(x, \theta, E) = \frac{1}{4\pi} \int_{E_1}^{E_2} \int_{S^2} S(x, \theta, \theta', E, E') I(x, \theta, E')\, d\theta'\, dE' + J(x, \theta, E). \tag{2.2}$$

The equation states that the change in intensity at a point is equal to the difference between the incoming intensity and outgoing intensity.

2.6.3 Beer-Lambert law

Neglecting the scatter component, the solution to the transport equation is given by the Beer-Lambert law,

$$I = I_0 \exp\left(- \int_L \mu(x)\, dx \right), \tag{2.3}$$

which relates the measured intensity, I, to the integral of the attenuation coefficient $\mu(x)$ along the ray path, L, where I_0 is the original beam intensity. It is intuitive to divide by I_0 and take the logarithm to obtain the linear equation,

$$\ln\left(\frac{I_0}{I}\right) = \int_L \mu(x)\, dx. \tag{2.4}$$

However, since the x-ray beam is polyenergetic, what is actually measured, in the absence of noise, is

$$I = \int_E I_0(E) \exp\left(\int_L \mu(x, E)\, dx \right) dE. \tag{2.5}$$

When a polyenergetic beam is transmitted, what is actually reconstructed is $\mu(x, \bar{E})$, where $\bar{E}$ is the effective energy of the scanner. The assumption that the beam is monoenergetic leads to artifacts in the reconstructed data, previously described as beam hardening.

2.6.4 Radon transform

Johann Radon formulated, in 1917, that given all the lines through a function f, it is possible to reconstruct f. For $f \in \mathbb{L}\{\mathbb{R}^n\}$, let $\theta \in S^{n-1}$ and let $\Theta^{\perp}$ denote the hyperplane perpendicular to θ. For $t \in \mathbb{R}$, the n-dimensional Radon transform is given by,

$$Rf(\theta, t) = \int_{\Theta^{\perp}} f(t\theta + y)\, dy. \tag{2.6}$$

This gives the integral of f over the hyperplane $\Theta^{\perp}$, with signed distance t from the origin. For simplicity let $R_\theta(t) = Rf(\theta, t)$.

The inverse problem in x-ray computed tomography is to reconstruct the two-dimensional image of cross-sectional slices of $f = \mu$ given a set of discrete line integrals through an object. In two-dimensional space the Radon transform is the integral

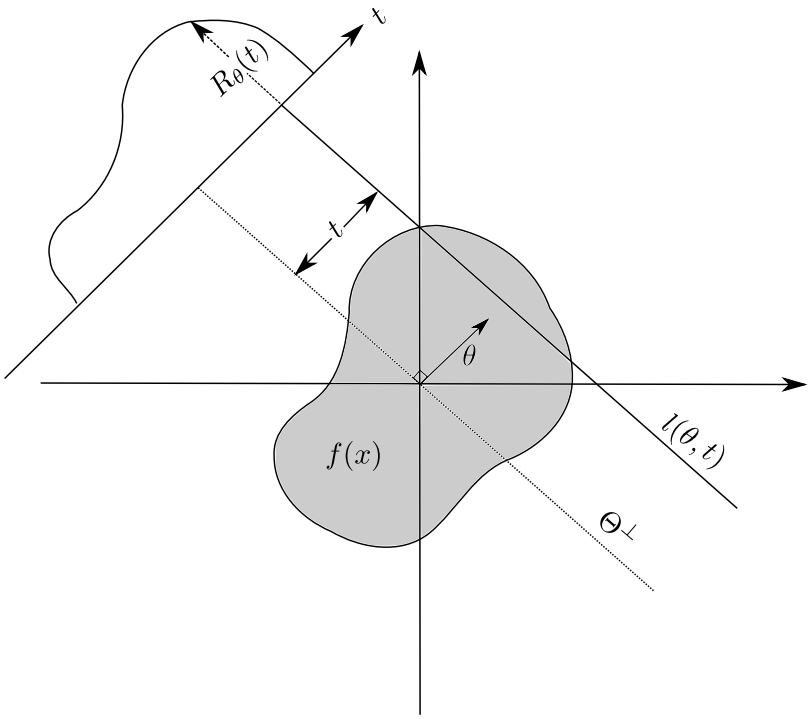

Figure 2.2: The two-dimensional Radon transform

along the lines parameterised by $l(\theta, t)$, where $\theta \in S^1$ is orthogonal to the direction of the line and $t \in \mathbb{R}$ is the distance of the line from the origin. Fig. 2.2 provides an illustration of the two-dimensional case.

The dual Radon transform of a function g, also known as the backprojection operator, is defined as,

$$R^* g(x) = \int_0^{2\pi} g(\theta, x \cdot \theta)\, d\theta. \tag{2.7}$$

The Radon transform represents all the points through a line and the dual Radon transform represents all the lines through a point [50]. This will become important later, but first it is necessary to introduce the Fourier transform of a function f and its relationship to the Radon transform.

2.6.5 Fourier transform

It is often useful to consider the frequency representation of a function [14]. This may simplify the calculations, for example the convolution operator in the space domain is a simple multiplication in the frequency domain, and the Fourier transform is crucial in the inversion of the Radon transform. Let $\hat{f}$ be the Fourier transform and $\tilde{f}$ be

the inverse Fourier transform of a function f such that,

$$\hat{f}(\omega) = \frac{1}{2\pi} \int_{-\infty}^{\infty} e^{-i\omega \cdot x} f(x)\, dx, \tag{2.8}$$

$$\tilde{f}(x) = \frac{1}{2\pi} \int_{-\infty}^{\infty} e^{i\omega \cdot x} f(w)\, d\omega, \tag{2.9}$$

where ω is a variable in the frequency domain, and x represents a point in the spatial domain.

2.6.6 Fourier slice theorem

The Fourier slice theorem relates the Fourier transform of one projection of f to its two-dimensional Fourier transform, and it also proves that the Radon transform is invertible. In this instance we have $f \in L^1\{\mathbb{R}^2\}$,

$$\widehat{R_\theta f}(\omega) = \frac{1}{\sqrt{2\pi}} \int_{\mathbb{R}} e^{-i\omega \cdot t} R_\theta f(t)\, dt$$

$$= \frac{1}{\sqrt{2\pi}} \int_{\mathbb{R}} e^{-i\omega \cdot t} \int_{\theta^\perp} f(t\theta + y)\, dy\, dt$$

Setting $x = t\theta + y$,

$$= \frac{1}{\sqrt{2\pi}} \int_{\mathbb{R}} e^{-i\omega\theta \cdot x} f(x)\, dx$$

$$= \frac{1}{\sqrt{2\pi}} \Big(2\pi \hat{f}(\omega\theta) \Big)$$

$$= \sqrt{2\pi}\, \hat{f}(\omega\theta). \tag{2.10}$$

That is, the one-dimensional Fourier transform of a parallel projection taken at an angle θ is proportional to a radial line at an angle θ of the two-dimensional Fourier transform $F(u, v)$.

2.7 Reconstruction

In theory, given enough projections of f, equation (2.10) could be inverted to solve for $f(x)$. However, this is not trivial and so more practical solutions are sought. The most popular inversion method is the filtered backprojection method. This is an accurate method, based on the Fourier slice theorem, that is suited to computational implementation. The method is described below.

2.7.1 Filtered backprojection

The method presented here is for the two-dimensional case. First, a point must be made about the Fourier slice theorem. As previously stated, the Fourier slice theorem relates the one-dimensional Fourier transform of a projection of f to a radial line of the two-dimensional Fourier transform of the function f. In practice, a discrete set of projection data is acquired leading to a discrete set of radial lines. This results in sparser sampling of the higher frequency components of the two-dimensional Fourier transform which, if inverted, would lead to blurring in the reconstructed image.

Let the Riesz potential, I^α, be defined by,

$$I^\alpha f(x) = \widetilde{|\omega|^{-\alpha}\hat{f}}(x). \tag{2.11}$$

Setting $\alpha = 0$, I^{-1} can be described as a simple ramp filter (Fig. 2.3) which accentuates the high frequencies that are missing from the two-dimensional Fourier transform. The filtered backprojection formula [53] can now be defined as,

$$f(x) = \frac{1}{4\pi} R^*(I^{-1}Rf)(x) \tag{2.12}$$

The proof is given by writing the two-dimensional inverse Fourier transform,

$$I^{-1}f(x) = \frac{1}{2\pi}\int_{\mathbb{R}} e^{iw\cdot x}|\omega|\hat{f}(\omega)\,d\omega. \tag{2.13}$$

and then changing to polar coordinates by setting $\omega = t\theta$ giving,

$$I^{-1}f(x) = \frac{1}{2(2\pi)}\int_{S^1}\int_{\mathbb{R}} e^{itx\cdot\theta}|t|^2\hat{f}(t\theta)\,dt\,d\theta, \tag{2.14}$$

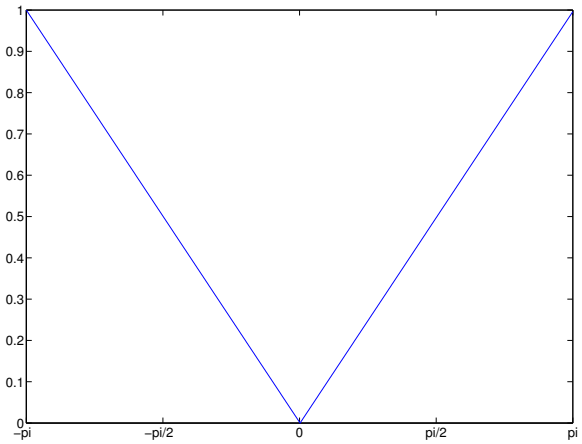

Figure 2.3: Ramp filter

where $t \in \mathbb{R}$ and $\theta \in S^1$. The factor of $\frac{1}{2}$ appears since $\hat{f}(t\theta) = \hat{f}(-t\theta)$. Then, from the Fourier slice theorem,

$$I^{-1}f(x) = \frac{1}{4\pi}\int_{S^1}\int_{\mathbb{R}} e^{itx\cdot\theta}|t|^2 \frac{1}{\sqrt{2\pi}}\widehat{Rf}(\theta,t)\,dt\,d\theta, \tag{2.15}$$

and finally using the definition of the Riesz potential,

$$f(x) = \frac{1}{4\pi}R^*(I^{-1}Rf)(x). \tag{2.16}$$

This is essentially a smearing back of the filtered projection data across the image plane. In practical circumstances applying a ramp filter to amplify the high frequencies can lead to undershoots at the object boundaries. Usually some smoothing is applied to the ramp filter to remove these artifacts.

To apply the algorithm above to fan beam data, the rays must first be rebinned by interpolation to obtain a set of parallel rays. A popular filtered backprojection algorithm for direct three-dimensional cone beam CT reconstruction is the FDK algorithm [27]. The original algorithm was proposed for a circular scanning trajectory and has since been extended to suit helical source trajectories [64]. More recently, a theoretically exact three-dimensional helical cone-beam CT formula has been proposed [40, 41, 39] that may be implemented by a filter backprojection algorithm. Alternative algorithms for helical cone beam CT reconstruction are given in [43, 63, 24, 16, 15]

2.7.2 Algebraic reconstruction techniques

Algebraic reconstruction techniques (ARTs) provide a completely different approach to image reconstruction [35]. The problem here is described as a set of simultaneous linear equations which are solved for the unknowns.

To reconstruct a tomographic slice algebraically from projection data, the unknown cross-sectional image is imagined to be discretised into small cells of constant attenuation coefficient. The set of linear equations are then formed by tracing each ray through the cells and summing over the contribution of each cell to the ray integral. Let N be the total number of cells and let M be the total number of rays over all projections, then if f_j denotes the attenuation coefficient in cell j and if g_i denotes the measured data for ray i, their relationship is given by,

$$\sum_{j=1}^{N} w_{ij} f_j = g_i, \qquad i = 1, \ldots, M, \tag{2.17}$$

where w_{ij} is the fractional area of cell j intercepted by ray integral i. This results in a system of M equations, one for each measured data value, with N unknown attenuation coefficients, one for each cell. Fig. 2.4 provides a simplified example with $N = 9$ and $M = 2$. In reality, however, M and N are large, and the larger the system of equations the more computations required to solve it.

ARTs were popular in the past when reconstruction was performed on a small grid of large voxels but, with increases in computing power and display resolution, M and N have grown very large rendering these methods computationally expensive and subsequently slow. These methods lack the accuracy of the filter backprojection method. However, in certain situations such as when only a small number of projection data can be taken, these methods are more flexible and provide a good alternative approximation. These algebraic techniques are usually solved iteratively, based on the method proposed by Kaczmarz. This method requires an initial estimate which is then projected onto the hyperplane represented by the first equation and then the second equation and so on, until a solution is found.

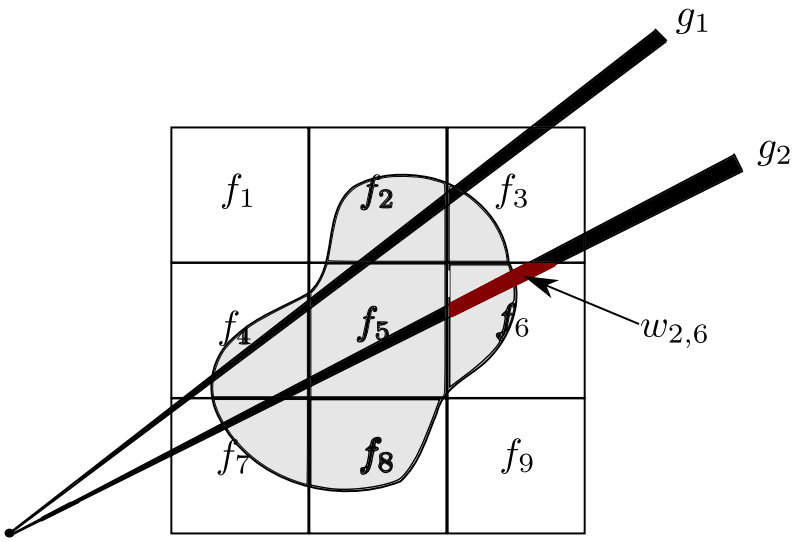

Figure 2.4: In ARTs a tomographic slice is divided into cells of constant attenuation coefficient and solved as a system of simultaneous equations.

Other general references are [29, 9, 30, 26]. This completes the general overview of x-ray computed tomography. An advantage of increases in computer technology is the ability to simulate physical problems in order to gather more information that would be difficult to gather experimentally. The remainder of the thesis focuses on scattered radiation that leads to artifacts in image reconstruction. In the following chapter a Monte Carlo simulation tool is described that will be used to investigate the problem of scattered radiation.

Chapter 3

Monte Carlo Methods and the Geant4 Simulation

3.1 Monte Carlo methods

Monte Carlo methods are computational methods that use pseudo-random sampling to solve problems that are too difficult to solve deterministically or numerically. Apart from statistical errors, the method is numerically exact. That is, given enough computing time, it would converge to the exact solution [11, 12, 49, 55].

In terms of photon transport, the Monte Carlo method is similar to the linear Boltzman Equation (2.2). Since particle interactions are inherently statistical, a Monte Carlo simulation can lead to a more realistic interpretation of physical phenomena. A Monte Carlo simulation of photon transport through matter can give more detailed information than an experimental setup, such as the separation of recorded primary and scattered radiation.

3.2 Geant4 Monte Carlo simulation

3.2.1 Introduction to Geant4

Geant4 is an object-oriented Monte Carlo toolkit for the simulation of particles through matter [1, 2]. Geant4 began from the merger of two separate studies at CERN and KEK that intended to improve the existing GEANT3 program by developing an object-oriented C++ framework code. This grew into a worldwide collaboration of scientists, due to its inherently adaptable nature. The software is freely available .

The object-oriented aspect of the framework allows it to be easily extended with additional functionality, and has led to a repository of particle interaction information that is up-to-date and constantly improving with developing research. All aspects of the simulation process are incorporation within the existing framework, and a number of user action classes, described below, allow the user to incorporate their particular machine specifications. Detailed particle tracking information at step points through the transportation process are available and can be manipulated suitably. Extensive literature validating the physics models is available in [5, 4, 45, 3, 7] to name but a few. Full details are available in the Geant4 website validation section.

The user defined action classes allow the user to implement machine specific requirements, such as geometry, physics processes and collection and storage of particle information. A Geant4 Monte Carlo simulation was implemented to emulate the RTT80 x-ray cone beam CT machine developed by Rapiscan systems Ltd. The implementation of such a large machine, with correct management of detector hits collections and manipulation of particle stacking to separate hits from different physics processes, is by no means trivial. The following section gives a brief overview of the main user defined classes used in this specific implementation.

3.2.2 User-defined classes

Detector Construction

The detector construction class is responsible for implementing the machine specific geometry. Initially, a world volume is created in which all other volumes will be placed. The size, physical position and rotation within the world volume and material of each additional geometrical entity is defined here.

Detectors: The detector positions and rotations are read in from file. Although, initially, the detector material was simulated it proved particularly time consuming and was subsequently neglected. The detector is now filled with air and all particle tracks are killed as soon as they reach a detector volume. The detector response can be incorporated separately after the data has been simulated.

Single ring or multiple ring detectors (from 1 - 8) can be created, depending on a macro command which is read in from file at runtime. The detectors are then defined to be sensitive elements in order to instigate their data collection when photons are incident upon them.

Sources: The sources are defined similarly to the detectors, as their positions and orientations are read in from file. The material is also air, but they are not sensitive elements. The sources have an area, representative of the incident area of the anode.

Source housing: An option is provided to simulate the source housing which consists of two carbon rings, a steel ring and an aluminium tunnel. This can be simulated in advance to save time, and is presented in the following chapter.

Objects: The region of interest is contained within another 'ObjectContainer' volume, which is defined to be a large cylinder filled with air. This has no impact on the data but allows any objects defined within it to be translated by the same amount if desired. Since it covers the whole region within the detector rings, translation would be in the z-direction to simulate object motion through the machine. However, this

similarly proved to be very time consuming and was subsequently ignored. With increasing processing power this would be a desirable effect.

Constructive Solid Geometry (CSG) representations and Boundary Represented Solids (BREPs) are available as solid representations. The objects used throughout this thesis are simple CSG models, such as boxes, cylinders and spheres.

Primary Generator

All the information regarding the generation of the primary particles is defined within this class. This includes the particle definition, the number of particles to be sent per unit of simulation (known as an event), the initial position, energy and direction. These values collectively determine the distribution of the x-ray beam.

The primary particles are chosen to be x-ray photons and, in this instance, a unit of simulation is chosen to be one photon per active detector for the current source projection. This does not necessarily mean that a photon is sent to each active detector, as this will depend on the algorithm chosen for the distribution of the rays.

Photon energy: The energy of the photons can be monoenergetic or polyenergetic. In the polyenergetic case, an energy is randomly sampled from the chosen input spectrum, which is read in from file.

If $p(E)$ is the probability density function of the chosen input spectrum, such that $0 \leq E \leq E_{max}$, and $F(E)$ is the cumulative distribution function of $p(E)$, then a random energy E^* is sampled by choosing a uniform random number $\xi \in [0, 1]$ such that:

$$\xi = F(E^*) = \int_0^{E^*} p(x)\, dx, \tag{3.1}$$

and

$$E^* = F^{-1}(\xi). \tag{3.2}$$

Initial photon position: The initial position of the photon is a point within the source area. This can be chosen to be either the central point of the source, as defined

in detector construction above, or a random point within the source which is defined to reflect the area of the anode.

Initial photon direction: The direction of each photon is determined by appointing a position within the active detector region. There are three options: Point detector, area detector and random sweep. Point detector is an option to send one photon to the centre of the face of each active detector, providing an even number of rays to all detectors over a number of events. The area detector algorithm results, similarly, in a photon being sent to each detector, but this can be at any random point on the detector face. The random sweep uses uniform random sampling to send all the photons in a random direction within the active detector region. This algorithm most closely reflects the behaviour of the beam experimentally, as it will not be evenly distribution unless a large number of events are simulated, and the detectors in front of the source will appear to have a larger surface area than those at the sides.

Run Action

A run is the largest unit of simulation. Within one run, the geometry, sensitive detectors and physics processes must remain unchanged. In this instance, a run is one source projection to one ring of detectors, where the number of photons to be transported through the object is set at run time.

The Run Action class determines what is to be done before and after each run. At the beginning of each run, Run Action handles the creation of data arrays to store the output data. All the details of the final output are set here, such as the output file names, the maximum histogramming energy and the number of energy bins. At the end of each run, the final histogrammed data is written to file in the required format.

Event Action

A run consists of a number of events; the smallest unit of simulation. As described previously, this is one photon per active detector, in one detector ring, for a given source projection. Event Action handles any processing required before and after an event, such as processing the detector hits results for histogramming. The Event Action class is given as an example of the code in Appendix A.

Stacking Action and Stepping Action

Stacking Action controls the order of the tracking of particles with a last in first out manner, although it is possible for the application developer to manipulate the order in which the particles are processed. When a particle is taken off the stack it is tracked until it is absorbed, killed or moves out of the world volume. Any secondary particles created are pushed onto the stack for later processing. The tracking involves small steps, determined by the mean free path of the particle, and the Stepping Action class provides particle information before, during and after each step. In order to record scatter separately, whenever Stepping Action provides the information that a scattering event has occurred, the particle track is killed and the photon pushed onto a waiting stack to await processing. Stacking Action then determines when these particles will be processed, which is chosen to be at the end of the event. This enables separate scattering collection, from Rayleigh, Compton and multiple scattering events, without additional simulations.

Physics List

All particle types, cut rates and physics processes are defined within this class. The interaction processes for this application are photoabsorption, Compton scattering and Rayleigh scattering. Detailed descriptions are presented in the following section, but first a description of how the interaction points are determined, and which of the interaction processes occurs, is given.

3.2.3 Calculating the mean free path

Particles are transported a step at a time. Each step length is based on the mean free path of the particle. For each process the mean free path of the particle is calculated separately.

Let n_i be the number of atoms per volume of the i^{th} element of a compound material with atomic number Z_i and let $\sigma_j(Z_i, E)$ be the total cross section per atom of the process j, where j is either Compton scatter, Rayleigh scatter or photoabsorption. Then, the macroscopic cross section for a photon of energy E is given by,

$$\mu_j(E) = \sum_i \big(n_i \cdot \sigma_j(Z_i, E)\big), \tag{3.3}$$

and the mean free path of the particle for process j is,

$$\lambda_j(E) = \mu_j(E)^{-1}. \tag{3.4}$$

Once the mean free path has been calculated for each process the interaction point must be determined.

3.2.4 Determining the point of interaction

The actual step length assigned to each process is randomly sampled using the mean free path. The probability of no interaction up to a point x is governed by the exponential probability law, $\exp\big(-\int_0^x \mu_j(x)\,dx\big)$. Hence, the probability an interaction occurs in the interval $x + dx$ is then,

$$P(x) = \mu_j(x) \exp\bigg(-\int_0^x \mu_j(x)\,dx\bigg), \tag{3.5}$$

and the cumulative distribution function is given by,

$$\begin{aligned} F(x) &= \int_0^x \mu_j(x) \exp\bigg(-\int_0^x \mu_j(x)\,dx\bigg)\,dx. \\ &= 1 - \exp\bigg(-\int_0^x \mu_j(x)\,dx\bigg). \end{aligned} \tag{3.6}$$

Let,

$$n_{\lambda_j} = \int_0^x \mu_j(x)\,dx = \int_0^x \frac{dx}{\lambda_j(x)} \tag{3.7}$$

be the number of mean free paths which a particle travels. Then,

$$F(x) = 1 - \exp\big(-n_{\lambda_j}\big). \tag{3.8}$$

The total number of mean free paths traversed by the photon before an interaction of process j, is sampled at the beginning of the trajectory such that,

$$n_{\lambda_j} = -\ln(\xi), \tag{3.9}$$

where ξ is a uniform random number in the interval $(0, 1)$. The shortest of $n_{\lambda_j} \cdot \lambda_j(x)$ triggers process j for which a new n_{λ_j} is sampled, and the total number of mean free paths for the remaining processes are updated accordingly for a step length Δx,

$$n^{'}_{\lambda_j} = n_{\lambda_j} - \frac{\Delta x}{\lambda_j(x)}. \tag{3.10}$$

This Geant4 implementation uses the RanecuEngine random engine from the Computing Library for High Energy Physics (CLHEP) for pseudo-random number generation. Uniformly distributed random numbers are sampled between 0 and 1 with a Multiplicative Congruential generator for the initialisation [32].

3.3 Physics Processes

3.3.1 Photoabsorption

This particular implementation of the Geant4 toolkit uses the low energy electromagnetic physics package to simulate photon absorption. This uses a parameterized photoabsorption cross section, which uses the least squares method to provide a separate fit of the coefficients a,b,c,d to the experimental data, taken from the EPDL97 data library [23], in several energy intervals. The photoabsorption cross-section is energy and material dependent and must be recalculated throughout the simulation.

$$\sigma(Z, E) = \frac{a(Z, E)}{E} + \frac{b(Z, E)}{E^2} + \frac{c(Z, E)}{E^3} + \frac{d(Z, E)}{E^4}, \tag{3.11}$$

where E is the energy of the x-ray photon and Z is the atomic number of the material. This gives the mean free path of the particle. The cross-section $\sigma(Z, E)$ is used in the calculation of the mean free path.

3.3.2 Scattering

The Compton and Rayleigh scattering processes are modelled using the Geant4 low energy Compton scattering package (G4LECS) [42]. Generally, in MC simulations, the target electron in the Compton scattering process is assumed to be at rest and in free space, when in reality the electron is bound to the atom of the traversed material. The extension package provides a slight variation on the standard Compton formula to account for Doppler broadening effects.

3.3.3 Total cross sections

The total cross-sections for the scattering processes are interpolated from the EPDL97 library, for a given energy E_0, as follows,

$$\ln(\sigma(E)) = \frac{\ln(\sigma_1)\ln(E_2/E_0) + \ln(\sigma_2)\ln(E_0/E_1)}{\ln(E_2/E_1)}. \tag{3.12}$$

where E_1 and E_2 are the closest energies below and above E_0 respectively that are available in the data library with corresponding cross-sections σ_1, σ_2 [66].

3.3.4 Sampling the scattering angle

If a Compton scattering event occurs the polar scattering angle, θ, is randomly sampled, based on composition and rejection methods, from the differential Klein-Nishina cross section multiplied by the incoherent scattering form factor interpolated from the EPDL97 data library,

$$P_s(\theta, q) = \frac{d\sigma}{d\Omega}^{\mathrm{KN}} \cdot SF(q) \tag{3.13}$$

where $q = E_0 \sin^2(\theta/2)$ is the momentum transfer and,

$$\frac{d\sigma}{d\Omega}^{\mathrm{KN}} = \frac{r_0^2}{2}\left(\frac{E'}{E_0}\right)^2\left(\frac{E'}{E_0} + \frac{E_0}{E'} + \cos\theta - 1\right). \tag{3.14}$$

The scattering process is rotationally symmetric and, therefore, independent of the azimuthal angle. The Klein-Nishina formula assumes a free electron and the form factor takes the electron binding effects into account, which effectively suppresses small angle scatter for low energy photons.

If a Rayleigh scatter event occurs the scattering angle, θ, is sampled according to,

$$P_r(\theta, q) = (1 - \cos^2\theta)\sin\theta \cdot FF^2(q). \tag{3.15}$$

The Rayleigh scattering form factor decreases rapidly as q increases, resulting in a strongly forward peaked distribution.

3.3.5 Sampling the scattering energy

There is no change in the energy of a Rayleigh scatter photon, so only Compton scattering is considered here. By the conservation of energy and momentum, the standard Compton formula from a free election is,

$$E'_{\text{free}} = \frac{E_0}{1 + (E_0/m_0c^2)(1 - \cos\theta)}, \tag{3.16}$$

where E_0 is the energy of the incident photon, E'_{free} is the energy of the scattered photon, θ is the polar scattering angle and m_0c^2 is the electron rest energy. The G4LECs approximation [56], relates the energy of the scattered photon from a bound electron to the energy of the scattered photon from a free electron by,

$$E' = E'_{\text{free}}\left(1 - \frac{p_z|\boldsymbol{k_0} - \boldsymbol{k'}|}{m_0cE_0}\right), \tag{3.17}$$

where $\mathbf{k} = |\boldsymbol{k_0} - \boldsymbol{k'}|$ is the photon momentum transfer and p_z is the component of the initial state electron momentum in the direction of photon momentum transfer [19].

With a description of the Geant4 Monte Carlo simulation complete, the following Chapter utilises the code to investigate scattered radiation in a switched source x-ray CT machine designed by Rapiscan Systems Ltd. A description of the imaging system is given, and results obtained when a number of different objects are simulated are presented.

Chapter 4

Scatter Investigation for the RTT80 Machine

4.1 The RTT80 machine

The real-time tomography (RTT) system designed by Rapiscan Systems Ltd is a baggage scanning x-ray cone-beam CT machine designed to produce 3-dimensional images in real time. It uses switched x-ray sources, positioned around a stationary ring, to reduce the time needed to scan an object compared to mechanically rotating systems. The imaging system has eight detector rings which lie out of the plane of the sources and cannot be collimated since they must be able to record photons arriving from all source projections. Incidentally, scattered photons can enter a detector from any point in the scanning region. The RTT80 machine has an 80cm diameter and is intended for airport baggage scanning.

A VRML view image of the machine is captured in Fig. 4.1. The green lines represent the x-ray photon tracks and it can be clearly seen that some of the photons are scattered out of the detector plane.

In a vacuum a pencil beam of x-rays travels in a straight line. However, when x-rays are projected in a straight line through an object some of the photons in the beam are lost. At the energies used in this application (30-160keV), this is due to either photoabsorption or x-ray scatter. The scattered photons can be sent in any

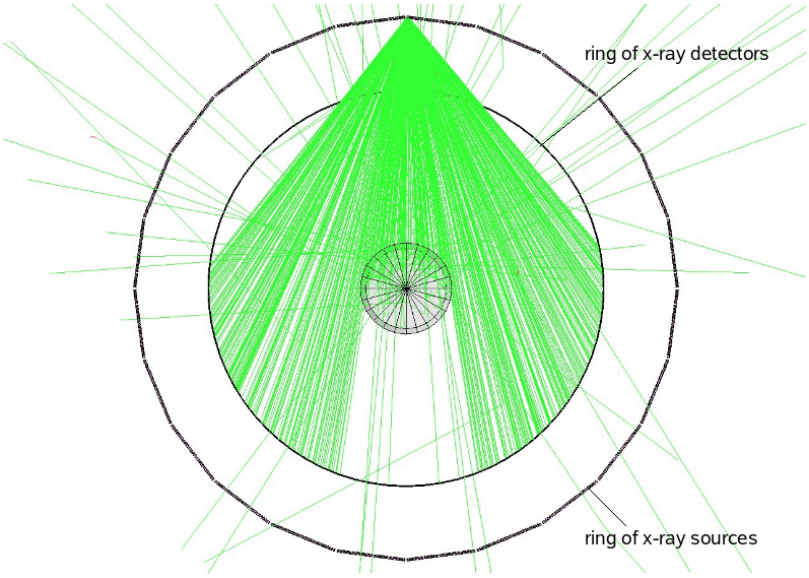

Figure 4.1: The RTT machine geometry with simulated object and photon paths

direction, according to some probability, and are unlikely to follow the same line as the original beam. When the energy of the beam is recorded in a detector after exiting the object, the resulting energy will be lower due to this attenuation.

A fan beam projection of x-rays consists of lots of pencil beams, or rays, from the source to each detector. If a photon scatters from a ray it is most likely to be scattered out of plane of the detectors. However, a scattered photon may deviate from its original beam path and be recorded in another detector, falsely increasing the recorded energy of the incident ray. This leads to degradation of the output image. It has been shown that scatter leads to streak artifacts in the image and adds to the cupping artifacts which are also attributed to beam hardening [33, 28, 34, 60]. The total amount of scatter contributing to the image is dependent upon the object material properties (atomic and electron densities), object size and distance to detectors, as well as incident photon energy. If the ratio of the scattered photons to the incident photons is high, this can seriously degrade the reconstructed image.

In conventional x-ray CT machines, with a rotating source and detector gantry (Fig. 4.2), each detector is collimated to limit the angle of scattered photons that can reach a detector. However, in the RTT system, since the detector ring is fixed, the same detector must be able to collect photons from a number of different source

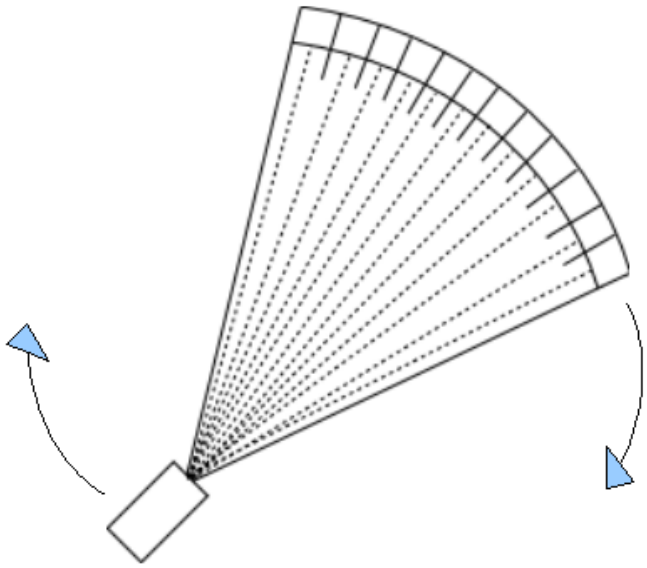

Figure 4.2: Conventional machine geometry with a rotating source and detector array.

projections travelling from a large range of angles, so this type of collimation is not possible.

Studies into scattered radiation, at these energies, are based on medical applications, where the scattered x-rays are mainly due to interactions with bone and soft tissue, the latter having a mass attenuation coefficient similar to water. Medical x-ray machines typically employ the conventional geometry, displayed in Fig. 4.2, with a rotating source and detector array, although often with a flat panel detector, for both fan beam and cone beam imaging systems. In airport baggage scanning the scattering objects are generally small in size with differing material properties.

It is, therefore, intuitive to investigate scattered radiation for both medical and airport baggage scanning applications specifically for the RTT machine geometry. The investigation is based on the Geant4 Monte Carlo simulation described in the previous chapter.

4.2 Verifying the model

4.2.1 X-ray source housing

To improve the speed of the Geant4 simulation the effect of the x-ray source housing on the initial input spectrum was determined in advance. The original input spectra are displayed in Fig. 4.3, and the source housing in Fig. 4.4. Each spectrum of x-rays in Fig. 4.3 is created by bombarding a tungsten target with electrons [22]. The incident electrons in (a), (b) and (c) have energies of 50, 100 and 150 kiloelectron volts respectively. No x-rays can be created with an energy greater than the energy of the electrons, due to conservation of energy. The graphs show the probability density function of hits recorded in energy bins, the smooth part of the spectrum is from Bremsstrahlung radiation and the peaks are due to characteristic x-rays. The characteristic x-rays are at the binding energies of the inner electron shells and are specific to the target material.

This x-ray source housing consists of a steel ring, two carbon rings and an aluminium tunnel. The attenuation of the x-ray beam after passing through the source housing was simulated and recorded in energy bins of 0.5keV, with 20000 photons being sent to each active detector. A simple analytic model was created to validate the simulation. This model traces each ray from the source to the centre of the detector, calculating the length of intersection of each ray with each of the source housing components.

4.2.2 Analytic model

Let r_{ij} denote the ray from source i to detector j, and let $N_0(E)$ be the number of initial photons at energy E such that $E = [E_1, E_2]$, , then the number of photons remaining after passing through the source housing is given by,

$$N(r_{ij}, E) = N_0 \exp\Big(- \sum_{i=1}^{4} \mu_i \cdot l_i \Big), \tag{4.1}$$

where μ_i denotes the attenuation coefficient of the i^{th} component and l_i is the length of the ray through the i^{th} component.

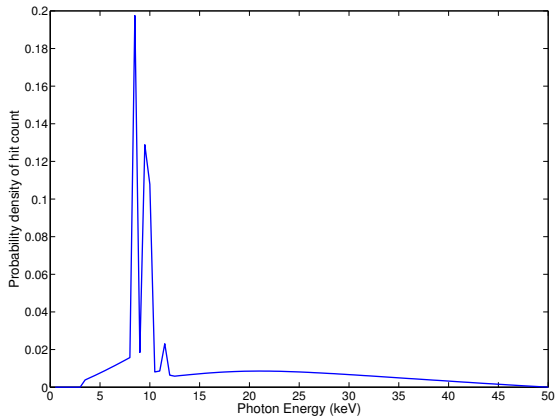

(a) 50kVp

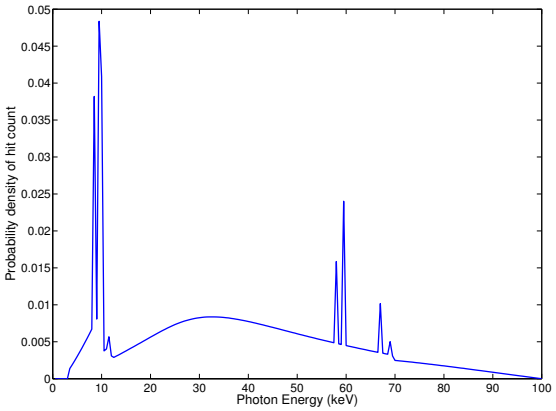

(b) 100kVp

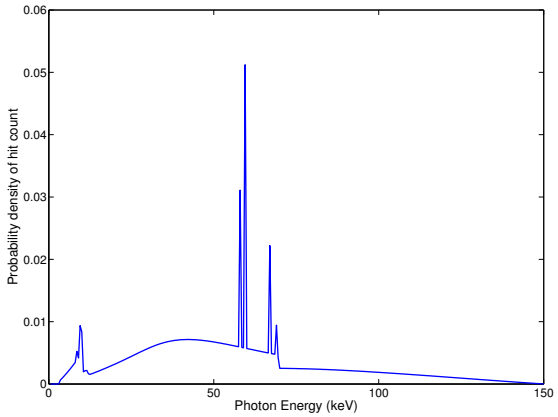

(c) 150kVp

Figure 4.3: Tungsten x-ray spectra

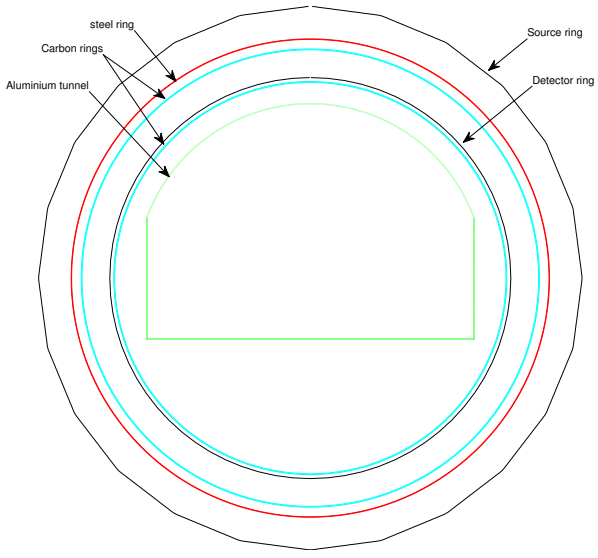

Figure 4.4: X-ray source housing

In the RTT80, the detector output is proportional to the total energy, which is given by,

$$\text{energy} = \sum_{E} N(E) \cdot E. \tag{4.2}$$

Fig. 4.5 displays the total energy remaining as a fraction of the original beam after passing through one side of the source housing, for each input spectrum and one detector ring. More of the original beam is absorbed at lower energies due to the energy dependence of the photoabsorption process. The simulated results are in excellent agreement with the analytic model, apart from the expected statistical fluctuations. The rays at the edge of the x-ray fan beam have the highest attenuation due to longer paths through the rings. The uneven distribution of the x-ray beam across the active detectors can be compensated for during calibration. It is the shift in the input spectrum to the detectors that is of interest, as all the physics processes are energy dependent.

Fig. 4.6 plots the energy spectrum recorded in three different detectors spread over the first half of the fan beam. There is little difference in the shape of each spectrum and so the new input spectrum is taken to be that which is recorded in the central detector. The amended input spectra in Fig. 4.7 show a shift to higher energies, as lower energy photons are more likely to be absorbed due to the energy dependence of the photoabsorption process.

To further verify the simulation, a 50mm radius aluminium cylinder and a 150mm radius water cylinder, relevant to the following scatter tests, were simulated and plotted against the analytic model. X-ray photons were directed to the centre of each active detector when simulating the aluminium cylinder, giving a perfect match to the analytic model, Fig. 4.8a. A very high photon count of 60000 per active detector were simulated to remove statistical fluctuations. For the water cylinder simulation the photon directions were randomly sampled within the active detector region resulting in some of the x-ray beam being lost in the gaps between the detectors, Fig. 4.8b, otherwise the comparison is good.

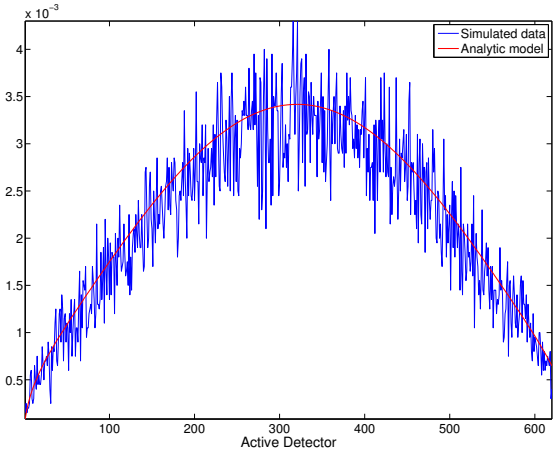

(a) 50kVp

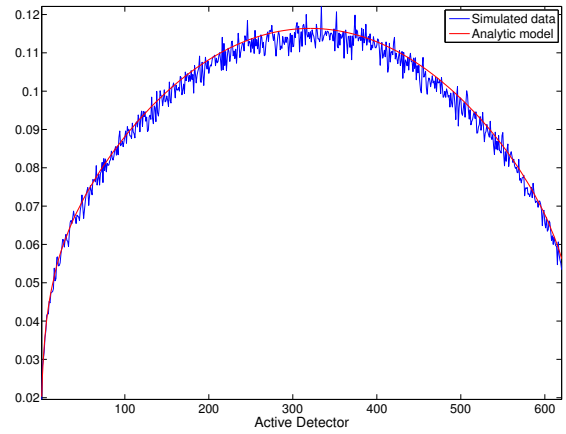

(b) 100kVp

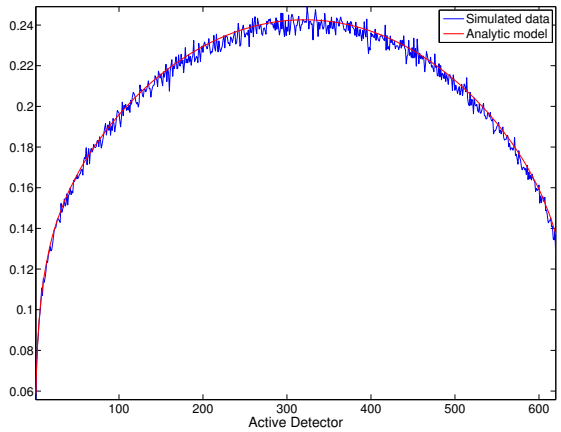

(c) 150kVp

Figure 4.5: Fraction of energy remaining after passing through the simulated source housing

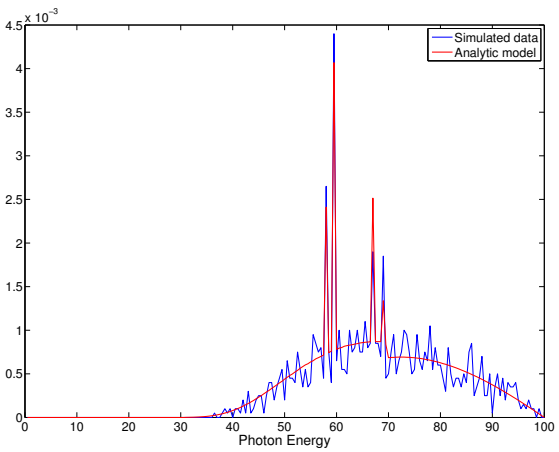

(a) Detector 300

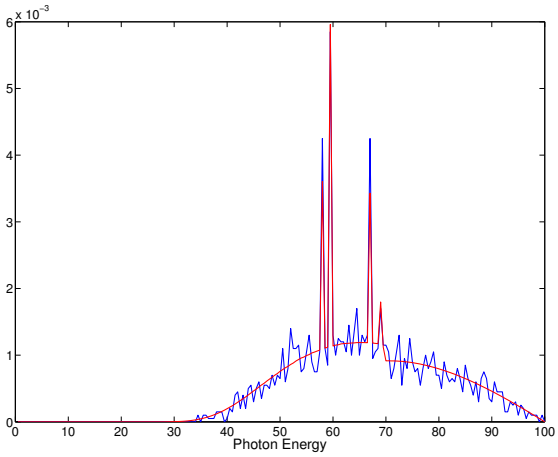

(b) Detector 400

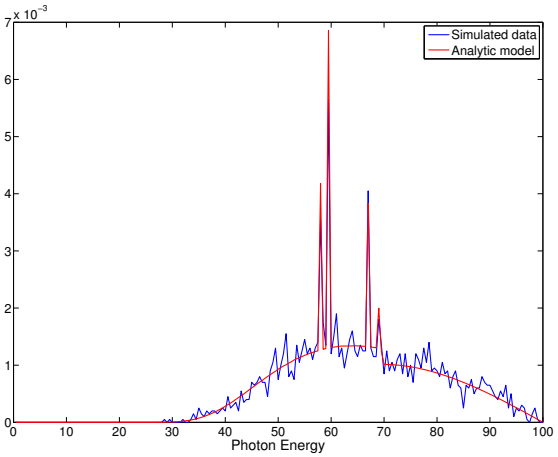

(c) Detector 500

Figure 4.6: Probability density functions of photon hits after passing through the source housing

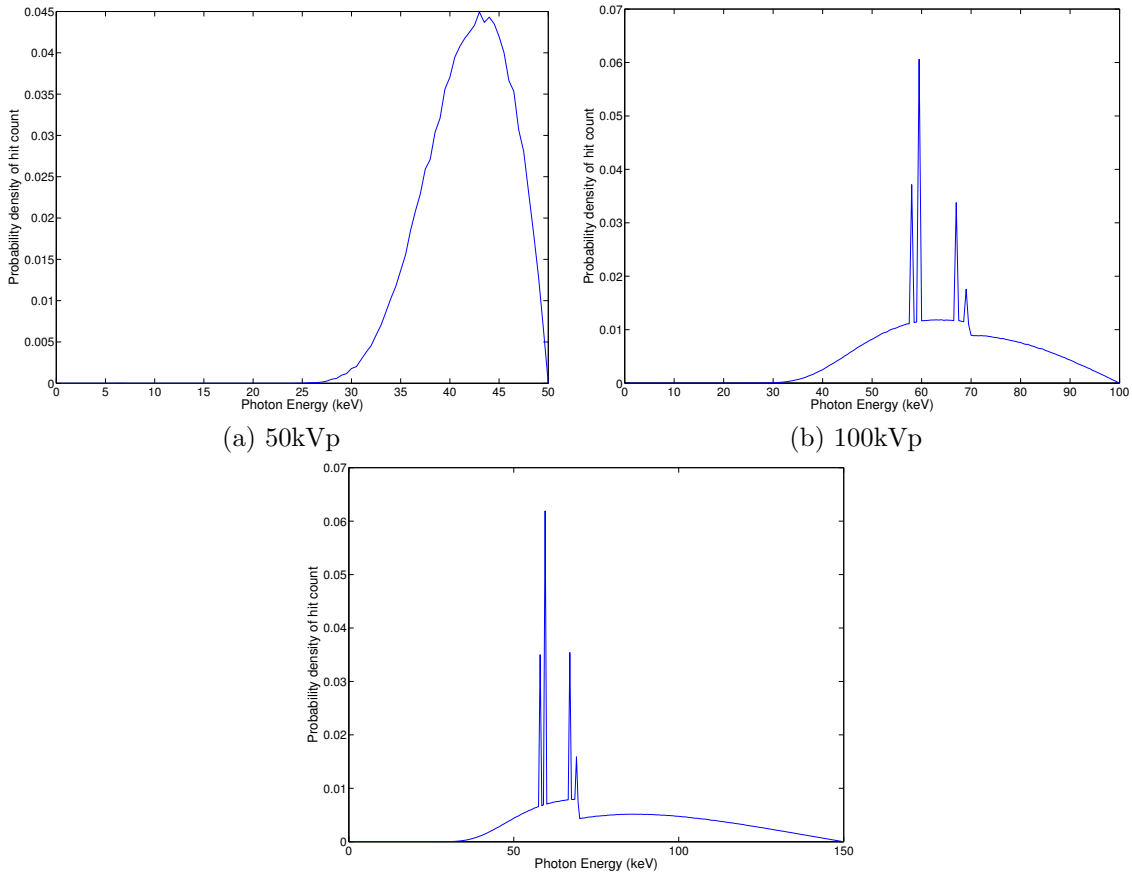

(a) 50kVp (b) 100kVp

(c) 150kVp

Figure 4.7: Tungsten x-ray spectra after passing through the source housing

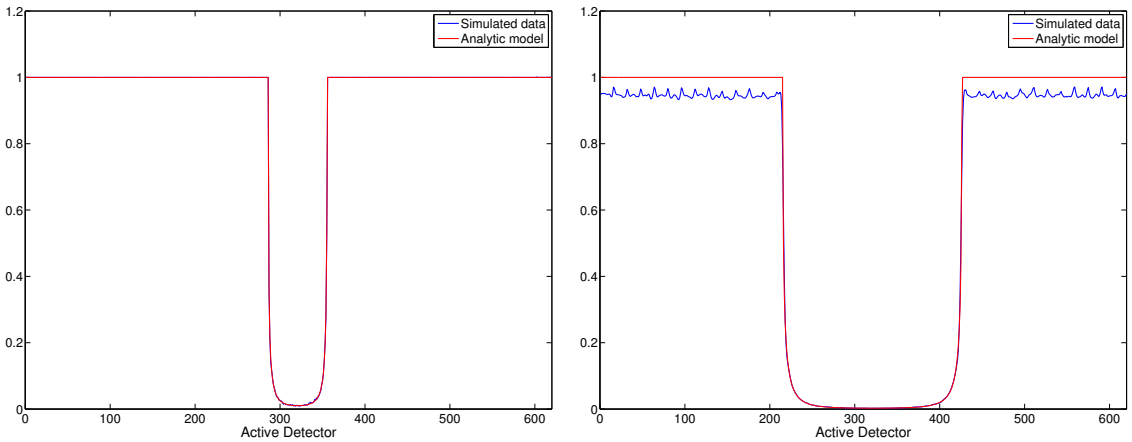

(a) 50kVp (b) 100kVp

Figure 4.8: Comparing simulated data to an analytic model

4.2.3 Real data

A comparison with real data is difficult as the RTT machine was still in the development stage throughout this study and, therefore, some approximations have been made. The number of photons depends on the peak kilovoltage (kVp), the tube current (mA), the pulse time (s), the target material and any beam filtration. As mentioned previously, the target material is tungsten (W) and the source housing, particularly the steel ring, provides the beam filtration. The remaining parameters were subject to extensive testing and are variable in real data collection with an aim towards a high current and 150kVp tube voltage. Therefore, simulated photon numbers were fixed as for a 20mA current, 150kVp tube voltage and a pulse time of 8.68×10^{-5}s giving a total of $N = 10.5\times10^{6}$ photons. This total number, N, is calculated from data provided by Rapiscan Systems Ltd, which provides tungsten x-ray spectra as a function of energy, E, for 30-150kVp tube voltages given in units of photons/(mA $\cdot$ s $\cdot$ mm^2), measured at a 750mm distance from the source.

If W_k is the tungsten spectrum for a tube voltage k, c is the current in mA and t the integration time in seconds, then the total number of photons in a projection is calculated by,

$$N = D\Big(\frac{750^2}{r^2} Atc \sum_E W_k(E) e^{-\mu \cdot l}\Big). \tag{4.3}$$

where A is the detector area, D is the number of active detectors, and r is the distance from the source to the central detector element.

Figs. 4.9 and 4.10 compare real data, on the left, to simulated data, on the right. This real data was collected with a 9.5mA current, a 100kVp polyenergetic input spectrum and an integration time of 8.68×10^{-5}s. Fig. 4.9a is a real white image, that is an image acquired with no object in the scanning region, with attenuation due only to the x-ray source housing. The data is averaged over a few runs with an averaged dark image subtracted. The dark image is the output of the system with no object and with the x-ray beam turned off. Once a dark image has been subtracted, the output of the RTT machine is proportional to the total energy of the photons absorbed by the detectors.

This real data image can be compared with Fig. 4.9b, the result of simulated Monte Carlo data, with $N = 11{\times}10^6$ based on the real data input parameters before filtering. The simulation consists of only the source housing and no object, with photons sent in any direction within the active detector region, unlike Fig. 4.5b where a fixed number of photons were directed to the centre of each active detector. The dip in the middle is due to intensity differences in the x-ray beam due to different path lengths from the source to detectors, given by the inverse square law,

$$I = \frac{I_0}{4\pi r^2}, \tag{4.4}$$

where I_0 is initial beam intensity and r is the distance from the source to the detector. Some of the beam intensity will also pass through the gaps between the detectors. A dip is also clear in the real data, and the alternating high frequencies observed in both images is due to the gaps between detector segments and the fact that the segments are straight with only the centre lying on a circle. The real and simulated outputs are clearly similar but there will be electronic noise in the real data. Another main reason for differences is due to scatter between different detector elements, since the detectors are not modelled in the Geant4 simulation there is no scatter between them. Finally, the material properties of the source housing components may not be exact.

Fig. 4.10a displays real projection data with a delrin cylinder object placed at the centre of the scanning region. For comparison, 4.10b provides simulated projection data of a delrin cylinder with N = $2{\times}10^6$, based on the real data parameters after filtering. The two sets of data provide a similar level of attenuation within the delrin region, although the material properties are not exactly known which explains a slight difference. The results outside the attenuating region for the simulated data do not provide the typical arch shape due to source housing attenuation as the input spectrum is approximated to be that given after passing through the source housing to the central detector in the projection. The real data is raw data and this uneven distribution is compensated for during calibration, however this data is not available.

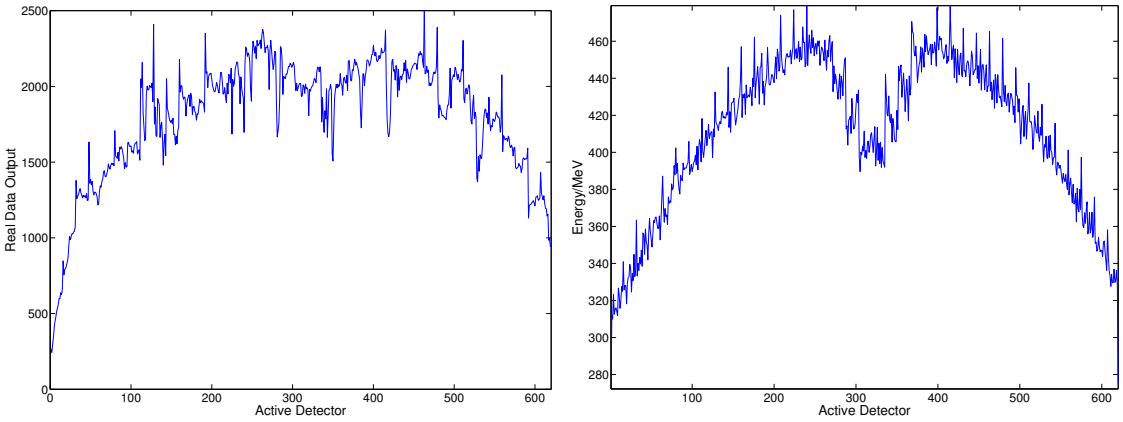

(a) Real data (b) Simulated data

Figure 4.9: No Object

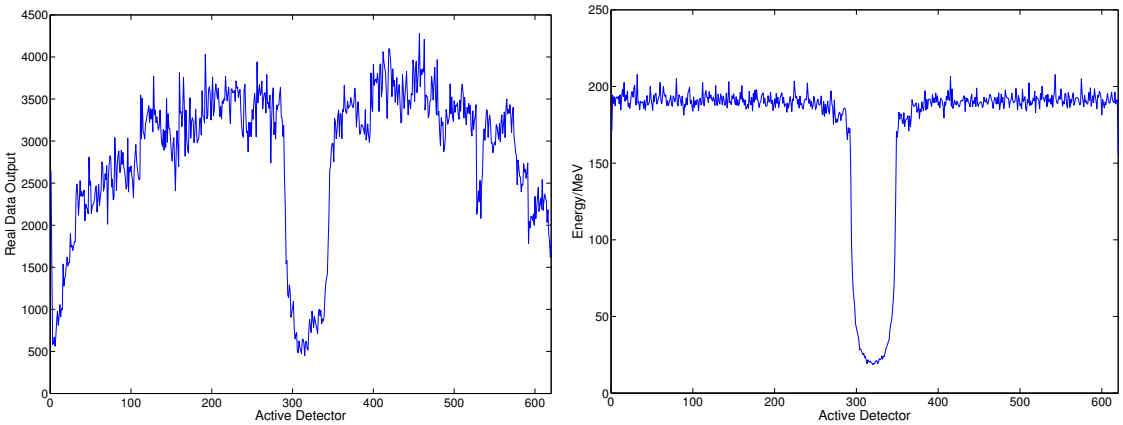

(a) Real data (b) Simulated Data

Figure 4.10: Delrin cylinder

4.3 Simulated scatter data

4.3.1 Simulated scatter objects

Four objects, displayed in Fig. 4.12, were simulated to analyse the effects of an uncollimated detector x-ray CT machine in airport baggage scanning and medical imaging. The Body Phantom is a 150mm radius cylinder of water. The Brain Phantom consists of a 90mm radius cylinder, where the outer centimetre is made of bone and the inner 80mm is made of water. The Cotton Suitcase is a box with a 2mm rim of PVC and an inner box of dimensions 450mm×250mm containing cotton, with a density of 0.2g/cm^3. The Mixed Suitcase is the same as the Cotton Suitcase but with two additional objects. A 0.5mm thick ring of aluminium with an inner radius of 29.5mm consisting of butane gas and a 1mm thick square container of PVC containing a 29mm×29mm square of water.

4.3.2 Experimental setup

The results were collected based on the amended 50kVp, 100kVp and 150kVp input x-ray spectra for a tungsten target. One source projection with both single and multiple detector rings were considered separately. The detectors lie on straight-line segments with the centre of each segment lying on a circle of radius 460mm.

Due to continuing developments, the detectors are assumed to have 100% efficiency which is a good approximation, particularly at lower energies. The detector response function for a typical scintillation detector material, LYSO, is displayed in Fig. 4.11. A detector response of 1 indicates that 100% of the photon energy is absorbed by the detector. Below 100keV almost 100% of the energy is absorbed and above 100kVp up to 80% of the energy is absorbed.

The x-ray beam is contained within the active detector region in all directions, and the depth of each object is greater than the beam coverage. A total of 10.5×10^6 photons were transmitted, as described previously, from a randomly sampled point on the source to a randomly sampled point in the active detector region. Particle cut

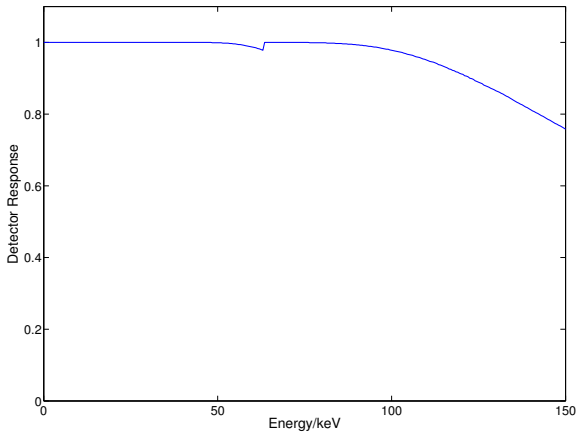

Figure 4.11: Detector response function for LYSO

rates were set to 1.0Å.

All four objects were analysed for each x-ray spectrum. The objects were placed at the centre of the scanning region, containing air, and material properties were taken from the internal Geant4 materials database, which is derived from the National Institute of Science and Technology (NIST) database [21].

Each simulation took between 3 and 8 hours to complete on a AMD opteron 2212 processor with a clock rate of 2GHz, depending on the size and material of the object.

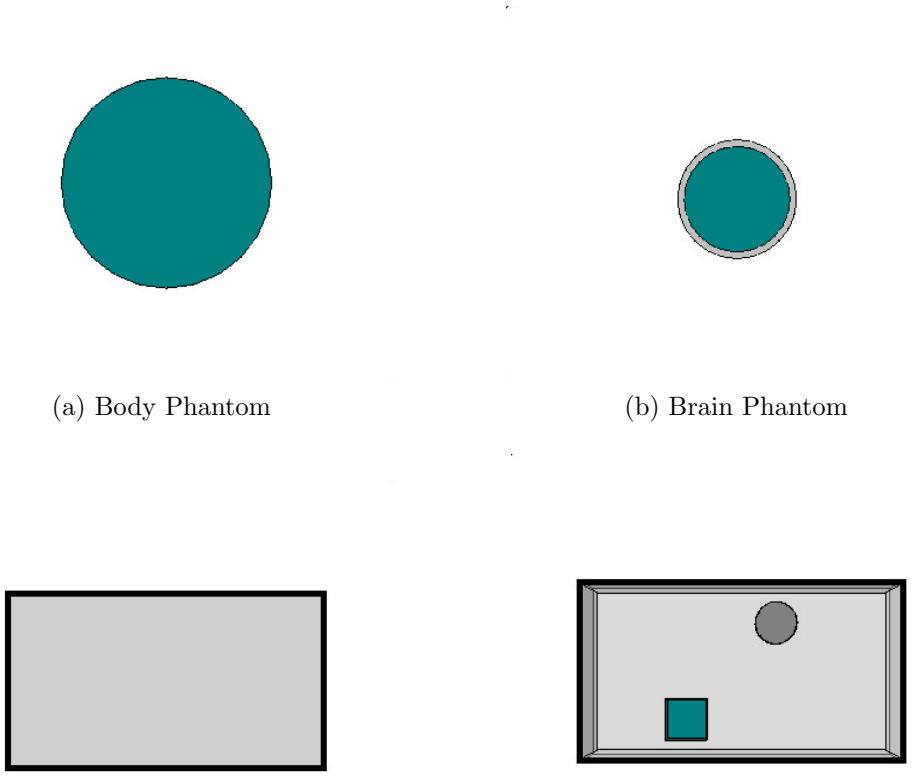

(a) Body Phantom

(b) Brain Phantom

(c) Cotton Suitcase

(d) Mixed Suitcase

Figure 4.12: VRMLview images of scattering objects

4.4 Results

4.4.1 Single detector ring data

Fig. 4.13 displays the results obtained for the Body Phantom with the 100kVp input spectrum, separated for each physics process. At lower energies and small angles Rayleigh scatter is expected to be dominant, where as at higher energies and wider angles Compton scatter is expected to dominate. This is clearly the case in this instance, which illustrates that the scattering processes behave as expected.

Figures 4.14-4.16 illustrate the results obtained for the Brain Phantom, Cotton Suitcase and Mixed Suitcase respectively for 100kVp. The Body and Brain Phantoms are more attenuating than the suitcases due to the higher density of water to cotton. The Body Phantom is more attenuating than the Brain Phantom since it has a larger radius creating a longer path for the photons to travel through the object.

The total energy of scattered photons recorded in each detector for the two suitcase objects is generally higher than the scattered energy recorded for the Body and Brain Phantoms.

The change in the reconstructed attenuation coefficients from the true attenuation coefficients due to scattered radiation depends on the fraction of the recorded signal as scatter. If the total signal is much higher than the scattered signal then the change will be minimal. If, however, the recorded signal is low, the change will be significant. The fractional contribution of scattered energy to the image is found by dividing the total scatter recorded in each detector by the total energy recorded. The results for each energy spectrum are displayed in Figures 4.17-4.19 and summarised in Table 4.1, which displays the maximum percentage of scatter contributing to the image for this projection.

Scatter levels are found to be highest for each of the objects when the lowest input spectrum (50kVp) is used. Low energy photons are highly absorbing so less primary beam is recorded. The Body Phantom projection contains very high levels of scatter, reaching 37% in this instance.

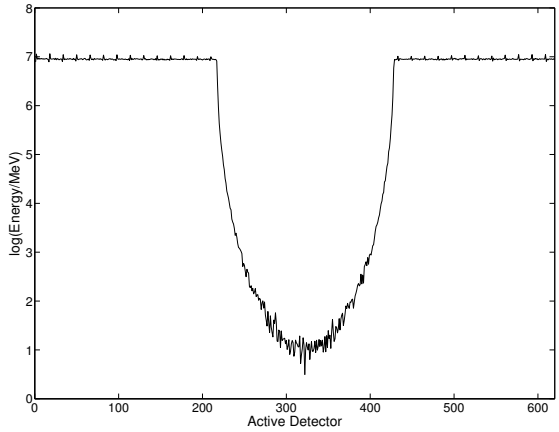

(a) Primary Photons

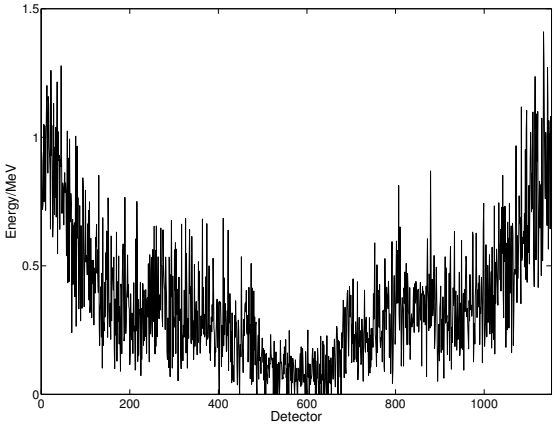

(b) Total Scatter

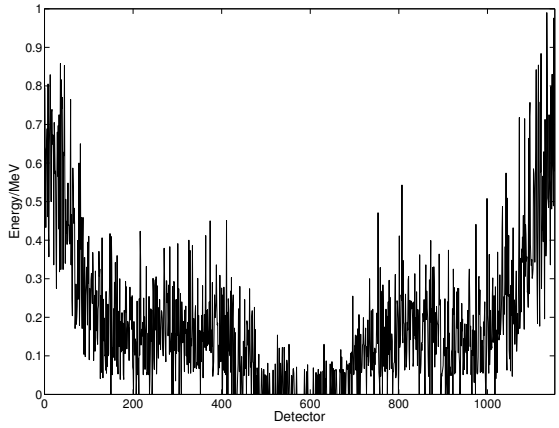

(c) Compton Scatter

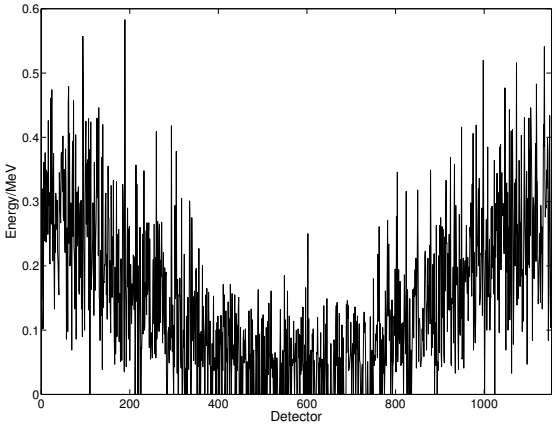

(d) Rayleigh Scatter

Figure 4.13: Simulation results for the Body Phantom at 100kVp.

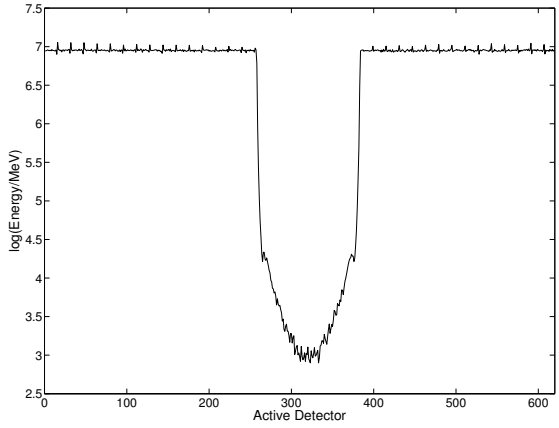

(a) Primary Photons

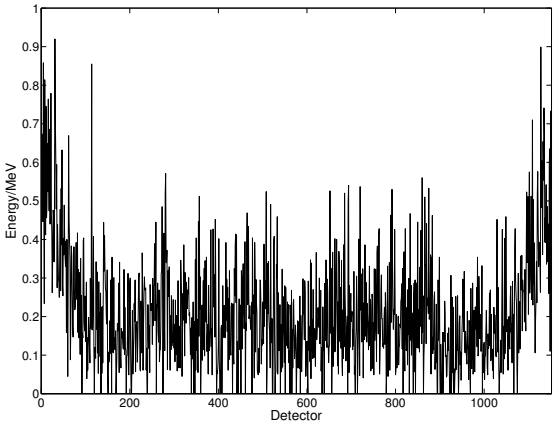

(b) Total Scatter

Figure 4.14: Simulation results for the Brain Phantom at 100kVp.

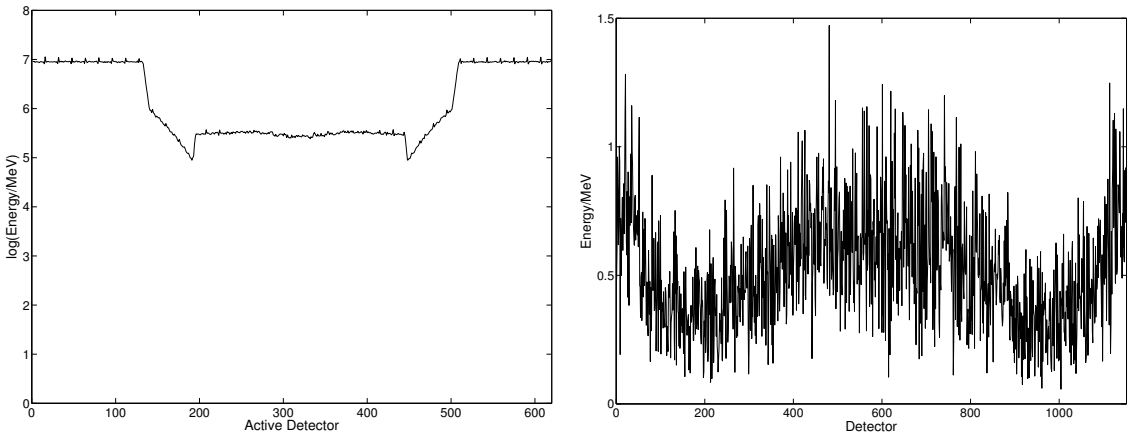

(a) Primary Photons (b) Total Scatter

Figure 4.15: Simulation results for the Cotton Suitcase at 100kVp.

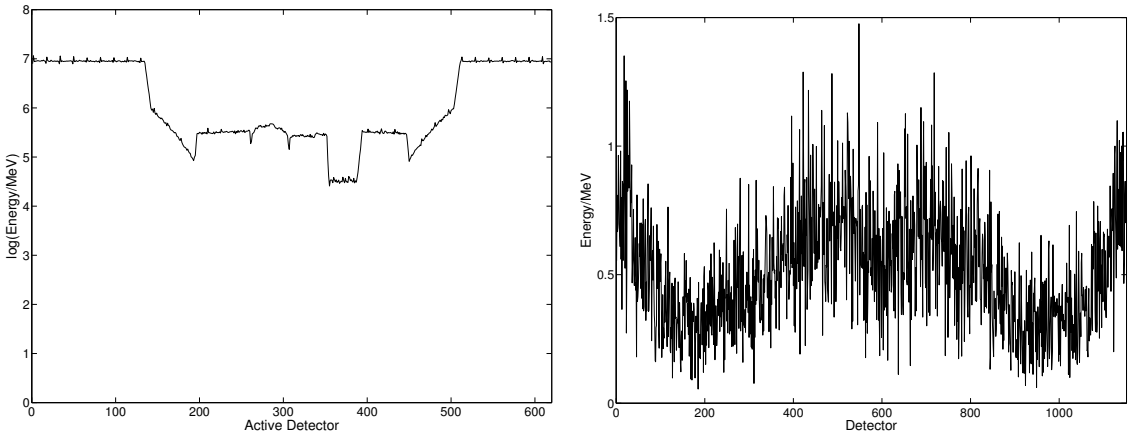

(a) Primary Photons (b) Total Scatter

Figure 4.16: Simulation results for the Mixed Suitcase at 100kVp.

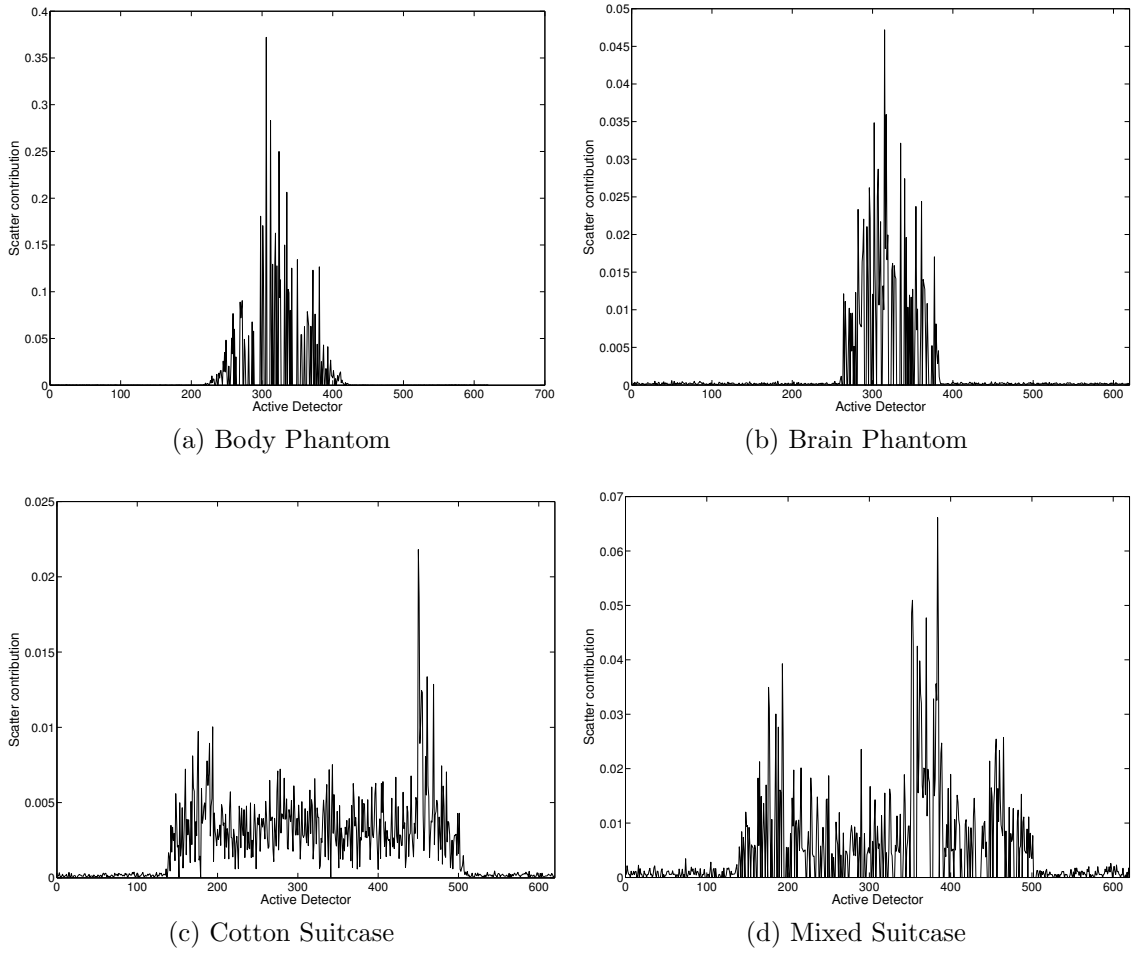

(a) Body Phantom

(b) Brain Phantom

(c) Cotton Suitcase

(d) Mixed Suitcase

Figure 4.17: Scatter contribution to the image for all objects at 50kVp

For each input spectrum the Body Phantom projection contains the highest percentage of scatter. As the x-ray energy of the input spectrum increases the levels of scatter contributing to the image decrease for each object considered. For 100kVp and 150kVp both of the suitcase objects have scatter levels of less than 1%.

A number of algorithms have been proposed for the removal of scatter from reconstructed x-ray CT images. These algorithms are usually based on single scatter approximations as it is possible to determine the location of the scatterer in this instance. When x-rays have been scattered multiple times, the origins of the scattering event are difficult to determine, so it is interesting to show a breakdown of the total scatter into single and multiple contributions, Table 4.2.

For large dense objects, where single scattered photons may have a long path through the object, the scattered photons are more likely to scatter again. If the

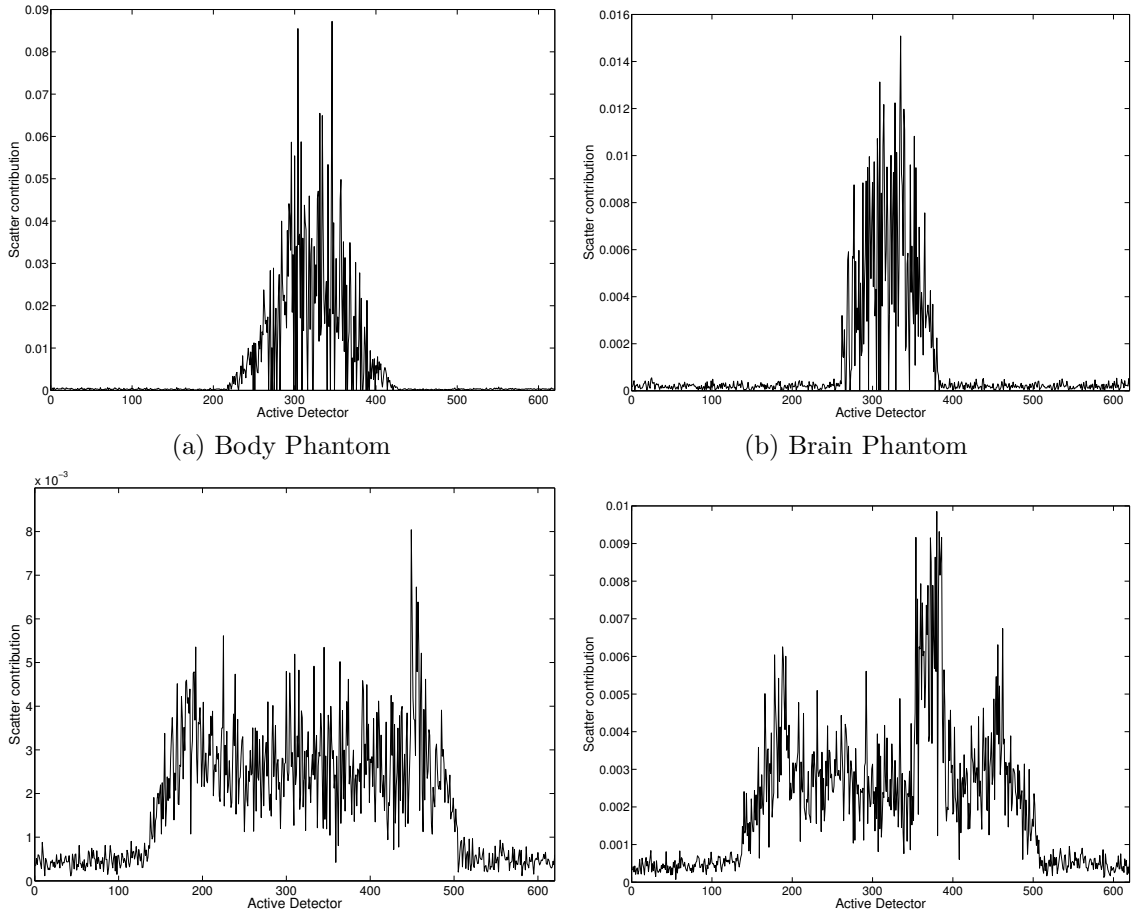

(a) Body Phantom

(b) Brain Phantom

(c) Cotton Suitcase

(d) Mixed Suitcase

Figure 4.18: Scatter contribution to the image for all objects at 100kVp

Table 4.1: Comparison of scatter contributions

	Max Scatter Contribution (%)		
Object	50kVp	100kVp	150kVp
Body Phantom	37.21	8.72	6.77
Brain Phantom	4.72	1.51	1.24
Cotton Suitcase	2.18	0.8	0.56
Mixed Suitcase	6.61	0.99	0.83

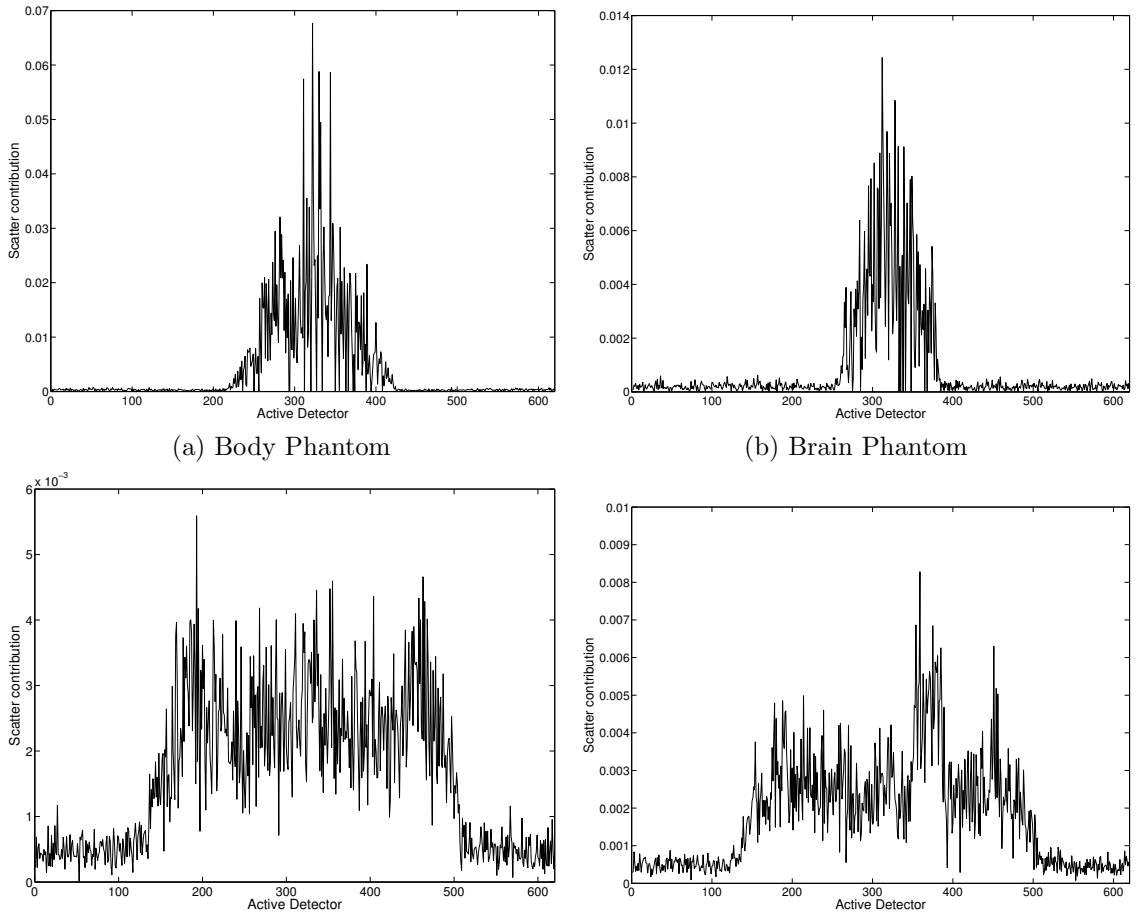

(a) Body Phantom

(b) Brain Phantom

(c) Cotton Suitcase

(d) Mixed Suitcase

Figure 4.19: Scatter contribution to the image for all objects at 150kVp

Table 4.2: Single and multiple scatter contribution as a percentage of total scatter

	Single (%)			Multiple (%)		
Object	50kVp	100kVp	150kVp	50kVp	100kVp	150kVp
Body Phantom	69.57	60.24	55.14	30.43	39.76	44.86
Brain Phantom	90.63	78.50	76.90	9.37	21.49	23.10
Cotton Suitcase	75.35	77.19	77.16	24.64	22.81	22.84
Mixed Suitcase	58.96	75.85	75.87	41.04	24.15	24.13

scattering material is not highly absorbing, these photons may emerge from the object and be recorded in the detector region. Approximately twice the percentage of multiple scatter is recorded for the Body Phantom compared with the other objects, that are relatively consistent, at 100kVp and 150kVp. Scatter correction methods are discussed in the next chapter.

4.4.2 Multiple detector ring data

Simulated data was similarly obtained for a cone beam imaging system with eight detector rings. Scattered radiation in a cone beam system is expected to be higher than fan beam systems due to a larger irradiation of the object. With greater object coverage there are more possible scattering locations and, with no detector collimation, the increase will be significant.

The detector rings are labelled from one to eight, depending on their proximity to the source ring, with ring one being the closest. Fig. 4.20 displays the multi-ring data for rings one, four and eight. The results differ slightly due to the small difference in ray path lengths through the object to each ring, but are similar nevertheless. Fig. 4.21 illustrates the large change in scatter contribution for all objects when changing from a fan beam to a cone beam imaging system.

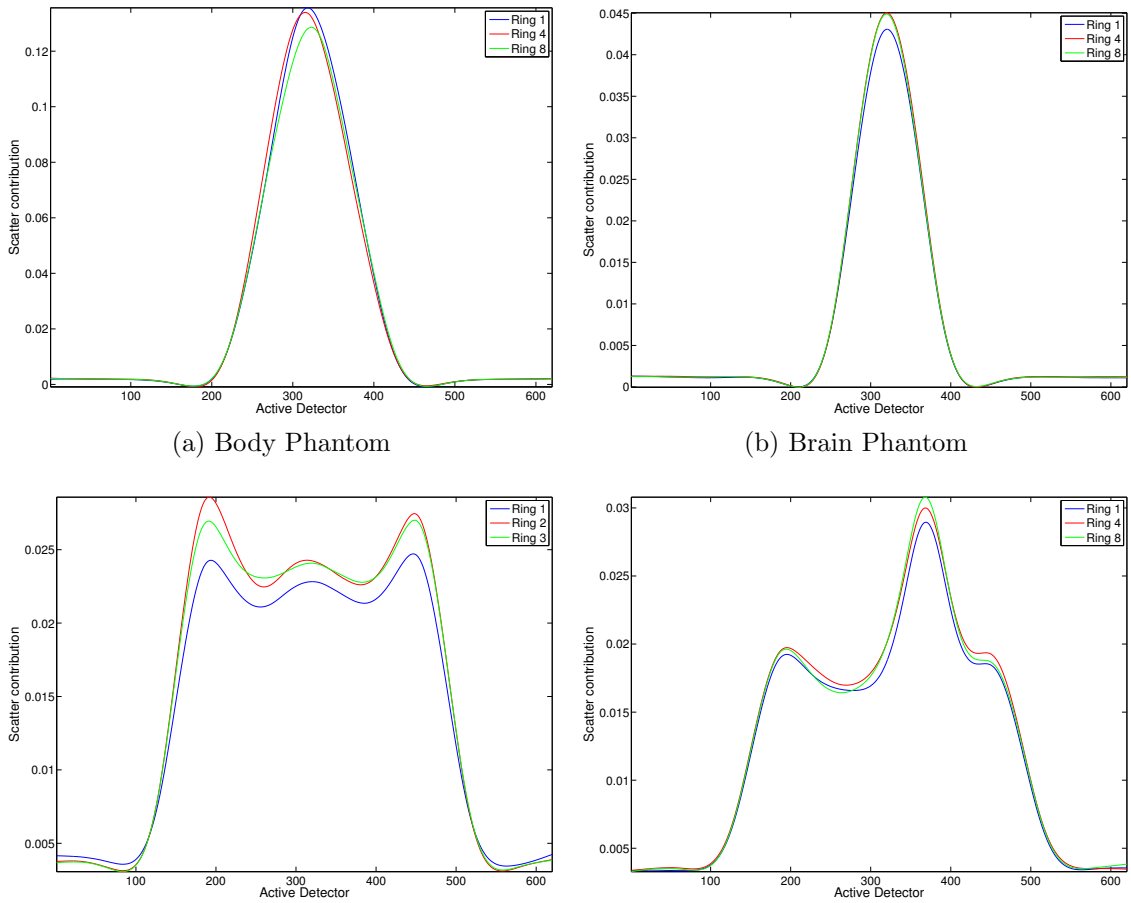

(a) Body Phantom

(b) Brain Phantom

(c) Cotton Suitcase

(d) Mixed Suitcase

Figure 4.20: Smoothed 8 ring scatter contribution at 100kVp

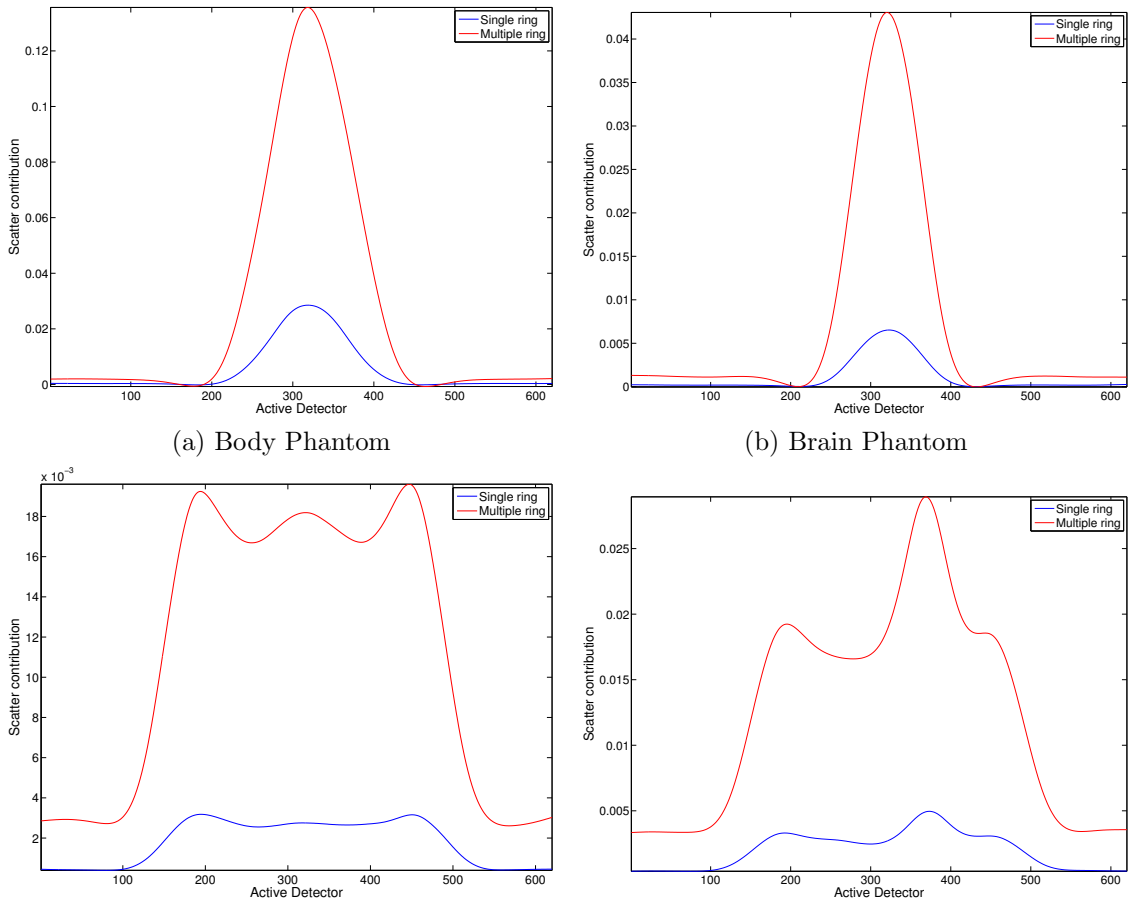

(a) Body Phantom

(b) Brain Phantom

(c) Cotton Suitcase

(d) Mixed Suitcase

Figure 4.21: Comparing single and multiple detector ring scatter at 100kVp

4.5 Summary

For the fan beam imaging system applied to medical scenarios, an uncollimated x-ray CT machine could lead to high levels of scatter in the image if the object being scanned was large. For a large water based object, such as the human body, most of the primary beam in the shadow of the object is absorbed, leaving a high level of the recorded data due to scattered photons. Advanced scatter correction methods would be required to reconstruct an acceptable image. Since the majority of space in a suitcase typically consists of clothing, which has a very low density, scatter contribution compared to primary beam is negligible. For small scattering objects, in this instance, the absence of detector collimation does not unduly compromise image quality. [62].

However, for the cone beam imaging system, scattered radiation contributes significantly to the image for all the simulated objects, for both medical and airport applications. In baggage scanning, identifying certain materials is a priority and so it is important to ensure accuracy in reconstructed density. An advanced scatter correction algorithm is, therefore, necessary.

In the next chapter, an overview of the current correction algorithms proposed in medical x-ray CT are presented. A new correction is subsequently proposed with the intention of providing a fast correction method for inhomogeneous objects imaged with a polyenergetic input spectrum.

Chapter 5

Scatter Correction

5.1 Scattered radiation in x-ray imaging systems

Scattered radiation has posed a difficult problem in all x-ray imaging systems and has been investigated extensively. However, the vast majority of literature, at the energies and object sizes considered throughout this thesis, are based on medical applications. In radiographic imaging, x-ray fan beam CT and x-ray cone-beam CT, scattered radiation has been shown to result in a decrease in the measured attenuation coefficient and consequently the introduction of streaks and cupping artifacts in the reconstructed image. Studies analysing these effects in radiography are [18, 36, 13], in fan-beam imaging systems [33, 34, 28, 38], and in cone-beam CT [25, 60].

Many of these studies, based on Monte Carlo simulations have shown that scattered radiation in an x-ray image is dependent on object size, thickness and material, as well as the detector field size, object-to-detector distance and the primary intensity of the x-ray beam. There is a significant increase in recorded scatter in cone beam imaging systems, where scatter-to-primary ratios of over 100% have been demonstrated for large objects and cone angles [60].

Although scattered radiation still causes artifacts in x-ray fan beam imaging systems with a rotating source and detectors, it is possible to collimate the x-ray source allowing only a small coverage of the imaged object and, similarly, to collimate the detectors to limit the number of angles from which they can receive the x-ray beam.

Although scatter is not completely eradicated, it is significantly reduced by these methods.

However, the introduction of fixed detector rings removes the possibility of detector collimation, as the detectors must record x-rays which are incident from many different angles. Cone beam imaging systems are particularly desirable as they allow imaging of large objects with isotropic resolution, and decrease the scanning time significantly. However, without scatter correction methods, cone beam CT provides much poorer quality images for low contrast objects than conventional CT machines due to an increase in the scattered radiation recorded [25]. This is due to a lack of source collimation leading to greater irradiation of the object and therefore more possible scattering locations.

For a cone-beam imaging system with fixed detector rings, such as the RTT80 imaging system, scattered radiation will be particularly high.

5.2 Scatter correction methods

Many methods have been proposed for the removal of x-ray scatter in CT images. One method proposes scatter suppression during the imaging process by inserting anti-scatter grids in front of the detectors; a method commonly used in radiography [25, 65]. However this method also removes some of the primary signal, reducing the signal-to-noise ratio, and would not be possible in a fixed detector ring system.

In flat panel imaging systems, the beam stop method requires that an array consisting of small lead discs be placed between the x-ray source and object [51]. Two projections are required with and without the beam stop array in place. The measured signal in the shadowed area of the lead discs is assumed to be entirely from scattered radiation and scatter distributions are estimated by interpolation from the scattered data. This method is impractical as it requires additional data acquisition.

[68, 60] have proposed extensions to this method. In [68], the method is based on an array of moving lead blockers, such that different detector elements are blocked throughout the acquisition and the missing primary is estimated by interpolation.

This method only requires one set of acquisition data, but still results in a decrease in the measured primary signal. It was proposed in [60] that collimators be placed at the edge of the source beam so that a shadow is cast on the edge of the detector plane, and the scattered distribution is estimated from the detectors in the shadow. The performance of this method is strongly object dependent, particularly for highly asymmetric phantoms. The beam stop method and it's extensions are not suitable for the RTT80 system geometry.

Methods in [28, 10] are based on the assumption that, for round phantoms, the scatter background is uniform, in either one projection or for the whole image. This is obviously impractical for irregular-shaped heterogeneous objects.

A number of methods have been proposed that produce scatter estimates based on simplified physics models and simplified geometrical descriptions [47, 52, 61, 58]. The convolution filtering method assumes the scatter distribution is a blurred version of the primary signal, implying a spatially invariant scatter distribution. The method was originally proposed for radiographic imaging in [47], in which a pre-determined scatter kernel, based on experimental acquisition with the beam stop method, is chosen to provide the smallest root-mean-square percentage error in a number of images. The scatter kernel is essentially a low pass filtered version of the detected primary distribution, which is unsuitable for a heterogeneous object.

[52] similarly provides a method based on the convolution of the weighted and windowed projection data, assuming a spatially invariant scatter convolution kernel, as a means to remove scatter from rotating detector and fixed detector fan beam systems. The scatter kernel in this instance is based on Monte Carlo scatter distributions, and requires prior knowledge of the object to be imaged. [58] proposes a similar method.

The scatter kernel superposition (SKS) method used in megavoltage image [61] has been adapted in [48] to be used in kilovoltage imaging where the scatter-to-primary ratios are much higher. The acquisition data recorded in each detector element is mapped to a water equivalent thickness (WET), and the scatter kernels are chosen based on these values. WET maps are described in [34] and are specific to medical

applications as they make the assumption that only soft tissues are present such that the mass attenuation coefficient is close to that of water and the material only differs in density.

The method in [57] is similar to the convolution filtering methods but provides an extension to account for the object heterogeneities. Calibration scatter kernels are generated by homogeneous objects of different thicknesses, estimated experimentally using the beam stop method with PMMA phantoms chosen for its similarity to soft tissue. After data acquisition, scatter kernels are obtained for each tomographic projection by interpolating the pre-determined calibration scatter kernels closest to the mean gray value of the tomographic projection. These scatter kernels are then adapted to take into account the inhomogeneities of the object in terms of a analytic single scatter model which is expressed as a function of the acquisition data. Multiple scatter is assumed to be the same for the object as for the calibration plate. Again, this is specific to medical imaging, but the idea that the single scatter component can be obtained as a function of the acquisition data is useful.

Monte Carlo methods have been utilised successfully in scatter analysis but the large computational time required for these methods restricts their use in correcting scatter [25, 36, 18, 13]. The Monte Carlo method to investigate scatter in [36] was implemented to speed up the conventional Monte Carlo simulation by using lookup tables for equiprobable scatter angles, originally proposed by Hemmings [36]. [20, 67] both propose methods to speed up the Monte Carlo simulation for scatter correction purposes. The first proposes a speed up of the Monte Carlo simulation with a forced detection algorithm and curve fitting procedure, leading to a speed increase of two orders of magnitude based on conventional Monte Carlo simulations. The second proposes a Monte Carlo simulation of the scatter element, based on the reconstructed image, to be obtained using a low photon count and then de-noised by a three-dimensional fitting of Gaussian basis functions, shortening the simulation time by three to four orders of magnitude. Even with these speed increases a Monte Carlo simulation of scatter for correction is still too slow for practical purposes.

A final method to be discussed combines deterministic and Monte Carlo calculations [44]. A deterministic method describes the contribution of single scatter events, from voxelised regions of the object, to the measured signal along with a coarse Monte Carlo method to determine the multiple scatter component. Essentially a integration over energy and volume is performed to calculate the single scatter intensity reaching a specific element for each scattering process. The Monte Carlo simulation for multiple scatter uses lookup tables for equiprobable scatter angles as described in [36]. This method provides a good approximation to the scatter component for inhomogeneous objects, and is easily adapted for different machine geometries. However, a deterministic method for computing the single scatter element would still be slow for practical purposes.

In summary, the algorithms described above are not achievable for the RTT80 geometry, make assumptions about the object that are not practical for this application or are too slow in practice. For airport baggage scanning applications the material properties and dimensions are completely unknown, unlike medical applications where some prior knowledge of the object scattering materials are known.

5.3 Scatter correction algorithm

It is desired to develop a fast scatter correction algorithm that works well for inhomogeneous objects, that are completely unknown prior to the data acquisition, and that is suitable for the unusual RTT machine geometry with a polyenergetic input spectrum. By first reconstructing the image and thresholding, it is possible to identify the scattering regions of the object and to estimate the scattering material based on the reconstructed attenuation coefficient. In order to obtain a fast algorithm, minimal calculations are required to estimate the scatter signal after the initial reconstruction.

The algorithm proposed in this thesis aims to approximate the scattered signal in each tomographic projection using pre-determined scatter distributions from small material samples, based on a Geant4 Monte Carlo simulation.

When a reconstruction is performed on the data the result is a three-dimensional

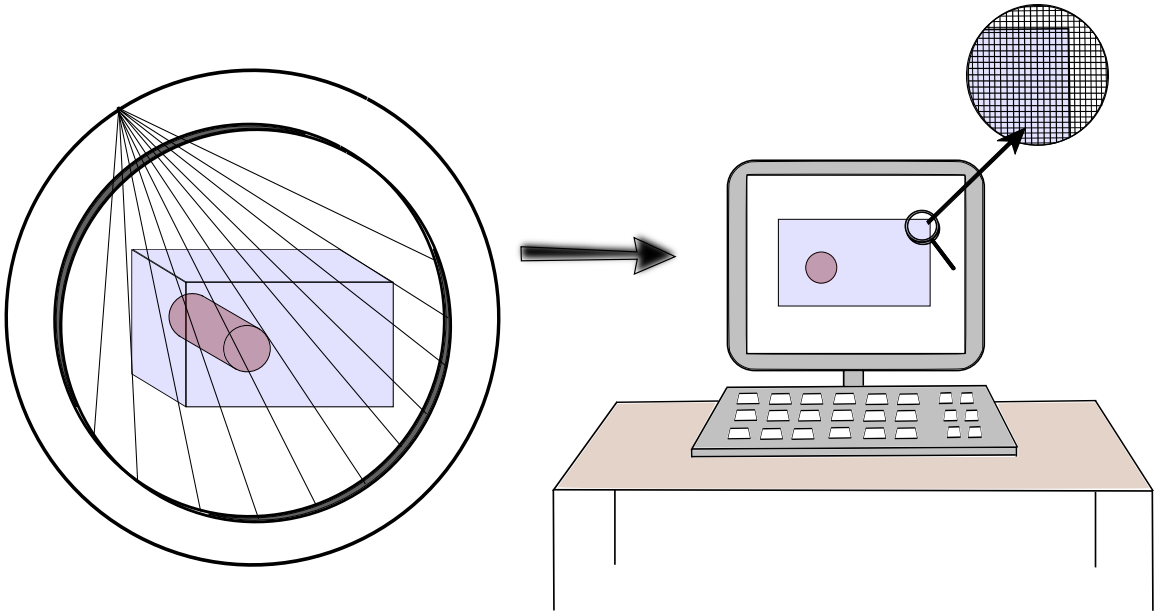

Figure 5.1: The object is scanned, reconstructed and displayed as a 2-D computer image. Each value in the image represents a small region of the object where μ is assumed to be constant.

computer array of attenuation coefficients, representing different slices of the object as the third dimension is traversed. Each value of the array represents a small region of the object where the attenuation coefficient is assumed to be constant. This sequence is illustrated in Fig. 5.1 for a simple suitcase object containing one scattering cylinder. The size of this region indicates the resolution of the system as any object smaller than this cannot be resolved. In this sense, the region of interest (ROI) within the scanner can be imagined to be discretised into small voxel elements representing a single attenuation value in the reconstructed computerised image. These voxels will be referred to as reconstruction voxels.

Once the scattering points have been identified within the computer image, the size and position of the scattering objects within the ROI are known. If the scatter signal originating from these objects could be determined it could be subtracted from the original data to give an almost scatter free image. There would still be a low background scatter component but the majority would be removed.

Ideally, the scatter objects could be re-created within a Monte Carlo simulation, however current computer processing power would not allow a fast approximation. The time that it takes to simulate projection data depends on the size and material

properties of the desired object as well as the computer processing power available. For those described in Chapter 4 each projection took between 3 and 8 hours to complete for only one detector ring. When multiple detector rings are used and many object rotations are required with simulated object motion, the simulation would require many months on many processors.

It is desired to provide a good approximation to the scatter component by performing as few calculations as possible. If scatter distributions from material samples of a certain size were pre-calculated, they could be utilised to approximate the single scatter signal.

To determine the algorithm, it is intuitive to imagine that the ROI is discretised into voxels that are larger than the reconstruction voxels in order to reduce the computation time. These voxels will be referred to as scatter voxels and denoted by v. Fig. 5.2 illustrates this for the simple suitcase object. Alternatively, think of each voxel as a value in a three-dimensional computer array which represents small regions of the object assumed to have constant scattering coefficient. These regions are larger than those represented in the reconstruction, therefore the array is smaller, and so there are multiple reconstruction voxels contained within each scattering voxel.

In this instance the voxels are chosen to be 1cm^3 in size which imposes a limit on the smallest size of a scattering object. The scattering voxels to be used in the scatter correction method are chosen to be those that have their centre lying in a scattering region of the reconstructed image. All other voxels are set to zero.

5.3.1 Scatter from a point

The algorithm is derived by first determining scatter from one scattering point, $\xi \in \mathbb{R}^3$, in source projection α to a detector β_s (see Fig. 5.3). The ray passing through ξ travels in the direction of the detector β_p, where the primary data is recorded. Let l_1 be the path of the ray through the object to ξ and let l_2 denote the path of the ray from ξ through the object in the direction of β_s. The primary path of the ray through

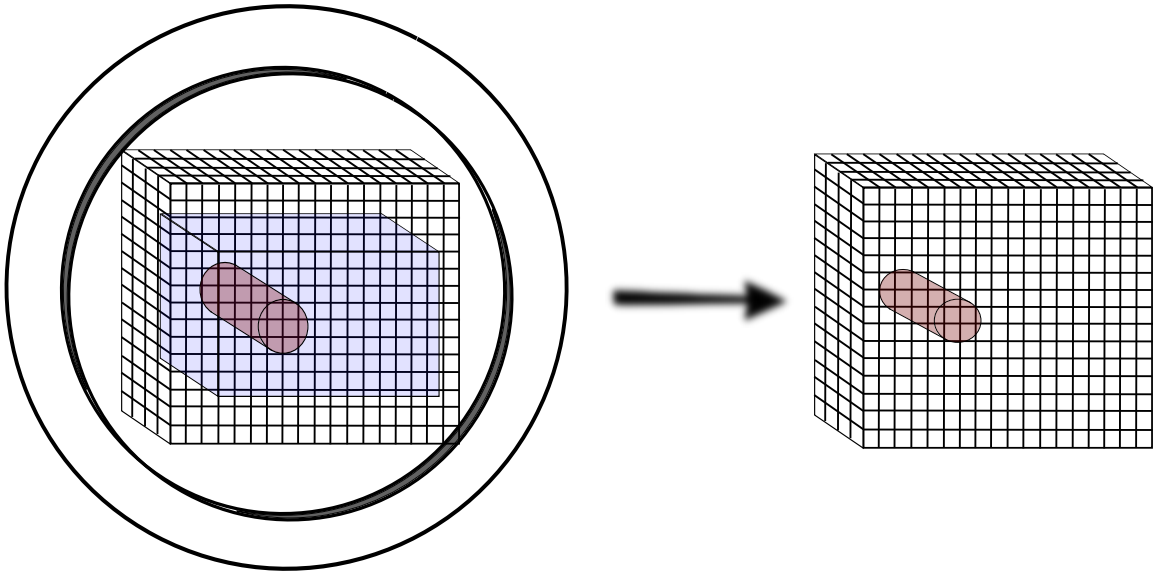

Figure 5.2: The ROI is imagined to be discretised into scatter voxels. A voxel with its centre lying in a scattering region is set to 'scattering' and all others are set to zero.

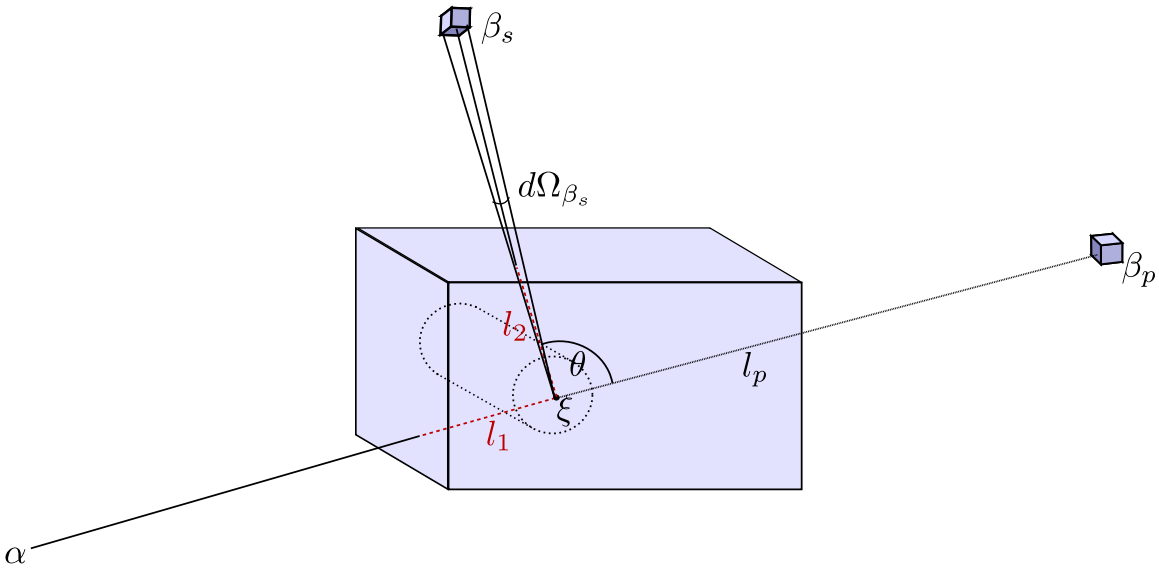

Figure 5.3: Scatter from a point ξ to detector β_s in source projection α

the object is denoted by l_p. Then the single scattered energy reaching detector β_s from the ξ in source projection α is given by,

$$I_s^{\alpha}(\beta_s,\xi) = \sum_g \int_E \Bigg[N_0(E) \exp\Big(- \int_{l_1} \mu(E,x)\,dx \Big) \frac{d\sigma_g}{d\Omega}(\theta,E,Z) E' \cdot \exp\Big(- \int_{l_2} \mu(E',x)\,dx \Big) d\Omega_{\beta_s} \Bigg] dE, \quad (5.1)$$

where, $N_0(E)$ is the number of initial photons at energy E, E' is the scattered photon energy, θ is the scattering angle, and $d\Omega_{\beta_s}$ is the solid angle subtended by the detector β_s at the the point ξ. The differential scatter cross-section is denoted by $\frac{d\sigma_g}{d\Omega}$ for process $g = \{\text{Compton, Rayleigh}\}$, μ is the attenuation coefficient and Z is the atomic number.

To minimise calculations the measured data will be utilised. With this in mind and since the majority of scatter is in the forward direction, the attenuation of the ray after the scattering event is approximated to be equal to the attenuation of the ray in the forward direction, $\theta = 0$, such that,

$$\exp\Big(- \int_{l_p} \mu(E,x)\,dx \Big) = \exp\Big(- \int_{l_1} \mu(E,x)\,dx \Big) \exp\Big(- \int_{l_2} \mu(E',x)\,dx \Big). \quad (5.2)$$

Using the Beer-Lambert law,

$$\frac{I_p(E)}{I_0(E)} = \exp\Big(- \int_{l_p} \mu(E,x)\,dx \Big), \quad (5.3)$$

equation 5.1 simplifies to,

$$I_s^{\alpha}(\beta_s,\xi) = \sum_g \int_E \Bigg[N_0(E) \frac{I_p(E)}{I_0(E)} \frac{d\sigma_g}{d\Omega}(\theta,E,Z) E' d\Omega_{\beta_s} \Bigg] dE. \quad (5.4)$$

The differential cross-section gives the probability that a photon will be scattered into angle θ. Let,

$$\frac{d\gamma}{d\Omega} = \sum_g \frac{E'}{E} \frac{d\sigma_g}{d\Omega}, \quad (5.5)$$

then $\frac{d\gamma}{d\Omega}$ gives the total energy scattered into angle θ per unit initial energy. Substituting this into equation 5.4,

$$I_s^{\alpha}(\beta_s,\xi) = \int_E \Bigg[I_p(E) \frac{d\gamma}{d\Omega}(\theta,E,Z) d\Omega_{\beta_s} \Bigg] dE, \quad (5.6)$$

since,

$$I_0(E) = N_0(E)E. \tag{5.7}$$

Define $\bar{I}_p$ as follows,

$$\bar{I}_p(E) = \frac{I_p(E)}{\int_E I_p(E)\,dE} = \frac{N(E)E}{\int_E N(E)E\,dE}, \tag{5.8}$$

where $N(E)$ is the number of photons remaining after object propagation and, therefore, $\bar{I}_p$ is the normalised output energy spectrum. Then,

$$I_p(E) = \bar{I}_p(E)\int_E I_p(E)\,dE = \bar{I}_p(E)I_p, \tag{5.9}$$

where I_p is the total primary energy after propagation. Assuming that the fraction of photons remaining at energy E after passing through the object are equal to the fraction sent, thus ignoring beam hardening effects, equation 5.9 can be written in terms of the probability density function of the input x-ray spectrum, $\bar{N}_0(E)$, such that,

$$\bar{I}_p(E) = \frac{\bar{N}_0(E)E}{\int_E \bar{N}_0(E)E\,dE}, \tag{5.10}$$

where,

$$\bar{N}_0(E) = \frac{N_0(E)}{\int_E N_0(E)\,dE}. \tag{5.11}$$

So $\bar{I}_p(E)$ can be calculated in advance from the input spectrum, and since the recorded primary data, I_p is unknown, an approximation is given by $I_{\tilde{p}}$ which is the measured energy data from primary and scattered photons,

$$I_{\tilde{p}} = I_p + I_s. \tag{5.12}$$

In terms of the measured data the total scattered energy from a point, ξ, is given by,

$$I_s^{\alpha}(\beta_s, \xi) = I_{\tilde{p}} d\Omega_{\beta_s} \int_E \bar{I}_p(E)\frac{d\gamma}{d\Omega}(\theta, E, Z)\,dE. \tag{5.13}$$

5.3.2 Scatter from a voxel

A voxel contains many scattering points so it is necessary to sum the contributions from each of these scattering points to determine the scatter contribution from a voxel,

v. Let ξ_v be the set of scattering points inside the voxel, v, such that $\xi_v = \{\xi : \xi \in v\}$, then the single scatter energy approximation from a voxel is,

$$I_s^{\alpha}(\beta_s, v) = \int_{\xi_v} \left[I_{\tilde{p}} d\Omega_{\beta_s} \int_E \bar{I}_p(E) \frac{d\gamma}{d\Omega}(\theta, E, Z)\, dE \right] d\xi. \tag{5.14}$$

Since v is small, the change in $d\Omega_{\beta_s}(\xi)$ is negligible and is assumed to be constant over ξ_v. Instead of treating scatter from each point in ξ_v separately it is intuitive to imagine that the voxel is one scattering point and that a ray of photons covers the voxel (see Fig. 5.4). In this sense equation 5.14 can be approximated by,

$$I_s^{\alpha}(\beta_s, v) = d\Omega_{\beta_s} \int_{\xi v} I_{\tilde{p}}\, d\xi \int_{\xi_v} \left[\int_E \bar{I}_p(E) \frac{d\gamma}{d\Omega}(\theta, E, Z)\, dE \right] d\xi$$

and by changing the order of integration,

$$= d\Omega_{\beta_s} \int_{\xi v} I_{\tilde{p}}\, d\xi \int_E \left[\bar{I}_p(E) \int_{\xi_v} \frac{d\gamma}{d\Omega}(\theta, E, Z)\, d\xi \right] dE. \tag{5.15}$$

If the probabilities of energy scattering into detector β_s for each point in ξ_v are grouped together, this gives an overall probability of energy scattering from the voxel v into detector β_s, per unit initial energy. Denote this by $\frac{d\gamma_v}{d\Omega}$ such that,

$$\frac{d\gamma_v}{d\Omega}(\theta_v, m) = \int_{\xi_v} \frac{d\gamma}{d\Omega}(\theta, Z)\, d\xi, \tag{5.16}$$

where θ_v is the angle between the line passing through the centre of the voxel and the line from the centre of the voxel to the centre of the detector β_s. Since $\frac{d\gamma_v}{d\Omega}$ depends on the number of scattering points as well as the atomic number, Z, this is now a function of $m(Z, \rho)$, where m represents the material and ρ is the density.

The integral over $I_{\tilde{p}}$ is the sum of all the measured data in the shadow of the voxel on the detector plane. That is, all lines passing through the voxel, which will be denoted by I_v and referred to as intensity for the remainder of the study, where,

$$I_v = \int_{\xi v} I_{\tilde{p}}\, d\xi. \tag{5.17}$$

Substituting $\frac{d\gamma_v}{d\Omega}$ and I_v into equation 5.15 gives,

$$I_s^{\alpha}(\beta_s, v) = I_v d\Omega_{\beta s} \int_E \bar{I}_p(E) \frac{d\gamma_v}{d\Omega}(\theta_v, E, m)\, dE. \tag{5.18}$$

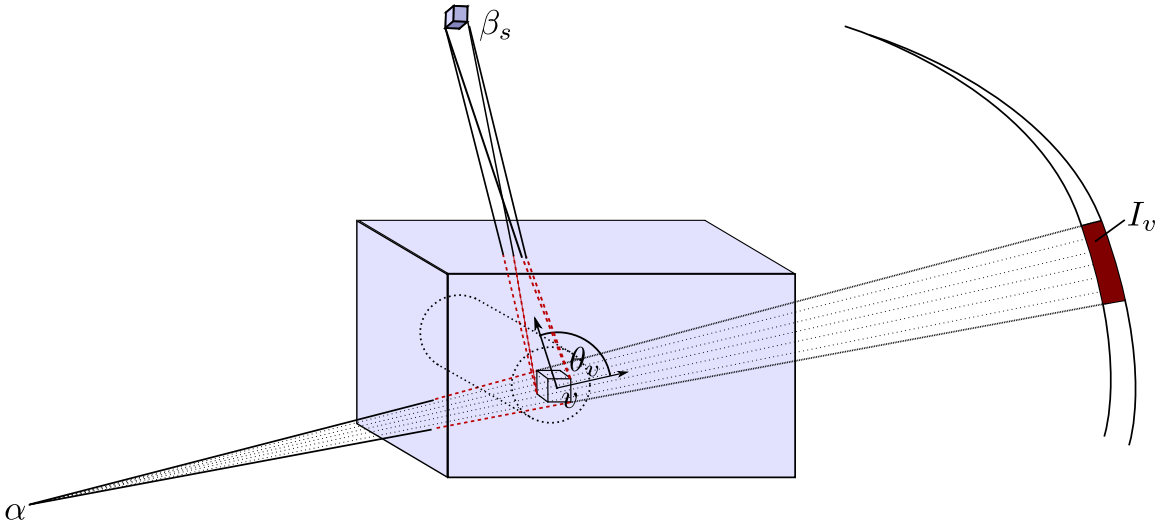

Figure 5.4: Scatter from a voxel v to detector β_s in source projection α

It is possible to determine $\frac{d\gamma_v}{d\Omega}$ in advance using a Monte Carlo simulation whereby a voxel of the desired size and material is illuminated with monoenergetic photons, which will be described in more detail in the following section. Similarly, $d\Omega_{\beta_s}$, θ_v and $\bar{I}_p$ can all be pre-calculated and stored in look-up tables to improve the algorithm efficiency. The detectors in the shadow of each voxel are also known, but I_v cannot be calculated until the projection data has been acquired. Since the geometry specific elements are calculated in advance, this is easily adapted and suited to any machine geometry.

In reality, E is binned into a discrete number of energy bins, $E = [E_1, E_2]$, and so the energy dependent data can be combined giving,

$$S(\theta_v, Z) = \sum_E \bar{I}_p(E) \frac{d\gamma_v}{d\Omega}(\theta_v, E, m)\, dE, \tag{5.19}$$

which can be substituted into equation 5.18 to give,

$$I_s^\alpha(\beta_s, v) = I_v d\Omega_{\beta s} S(\theta_v, m). \tag{5.20}$$

5.3.3 Scatter from an object

Once a reconstruction has been performed the scattering regions must be identified and the corresponding scatter voxels set to 'scattering'. Let the indicator function

χ_s represent this acceptance such that,

$$\chi_s(v) = \begin{cases} 1 & \text{if } v \text{ is scattering} \\ 0 & \text{if } v \text{ is not scattering} \end{cases}$$

then the total scatter to a detector in a projection is the sum of all the contributions of scatter from each scattering voxel. That is,

$$I_s^{\alpha}(\beta_s) = \sum_v \chi_s(v) I_v d\Omega_{\beta s} S(\theta_v, Z). \tag{5.21}$$

The speed of the scatter algorithm will depend on the size and number of scattering objects present. Once a scatter estimate is obtained, for each source projection, this can be subtracted from the original data and a second reconstruction performed.

5.3.4 Pre-calculated data

For the remainder of this study the object is assumed to be static, however the algorithm could be extended to incorporate a moving conveyor. Considering one source rotation of the object a sub-region of the ROI is discretised into four rows in the z-direction, or cross-sectional slices, each consisting of 50 by 50 voxels of 1cm^3 in size. This covers a sub-region of 500mm by 500mm by 40mm. The x-ray cone beam is considered only to cover the eight-ring active detector area and is contained within the four slices.

Scatter distributions

The scatter distributions were obtained by sending monoenergetic photons from a point source through both a sphere and a cylinder of radius 5mm and recording the scattered energy in detectors at angular intervals from 0 - 180°. The beam completely covered the samples. Although this is essentially a single scatter calculation, some multiple scatter was also recorded in the process and contained within the distributions.

The source lies 400mm from the sample and results are obtained for detectors at both a 200mm and a 400mm radius in an arc around the sample sphere, where air is

Table 5.1: Material

Material	Atomic No.	Density (g/cm^3)
Water	7.42	1
Aluminium	13	2.7
Stainless Steel	26	7.88
Lead	82	11.34

modelled in the experimental region. Results are also obtained with the experimental region as a vacuum. The source, sample and detectors all lie in the same plane. Since scatter is rotationally symmetric it is independent of the azimuthal angle so values at polar angles from 0° - 180° are all that are required. Since scatter is a slowly varying function, 2° angular samples are taken and interpolated to provide a good approximation.

Angular scatter distributions were simulated for 15 energies from 10keV to 150keV and four materials; water, aluminium, lead and steel. Their properties are displayed in Table. 5.1, and corresponding cross-sectional data taken from the NIST XCOM database in Fig. 5.5.

The experimental set-up is illustrated in fig. 5.6, although it is not to scale. Let N_0 be the number of photons sent from a monoenergetic source, with energy E, in any direction through the sample and let $T(\theta_v)$ be the total scattered energy recorded in detector $\beta(\theta_v)$. The scattered angle θ_v is the angle made between the line from the source through the centre of the sample and the line from the centre of the sample in the direction of the centre of the detector β. Then define T_A to be the average energy scattered per photon sent such that,

$$T_A(\theta_v) = \frac{T(\theta_v)}{N_0}. \tag{5.22}$$

The value of T_A will depend on how many photons are sent but eventually $\frac{dT_A}{d\Omega}$ converges, where $d\Omega$ is the solid angle subtended by a detector with the centre of the source. The scatter distribution can then be defined as,

$$\frac{d\gamma_v}{d\Omega}(\theta, E, m) = \frac{1}{E}\frac{dT_A}{d\Omega}, \tag{5.23}$$

which gives average energy scattered into angle θ_v for material m, per unit initial energy, E, per unit solid angle [46].

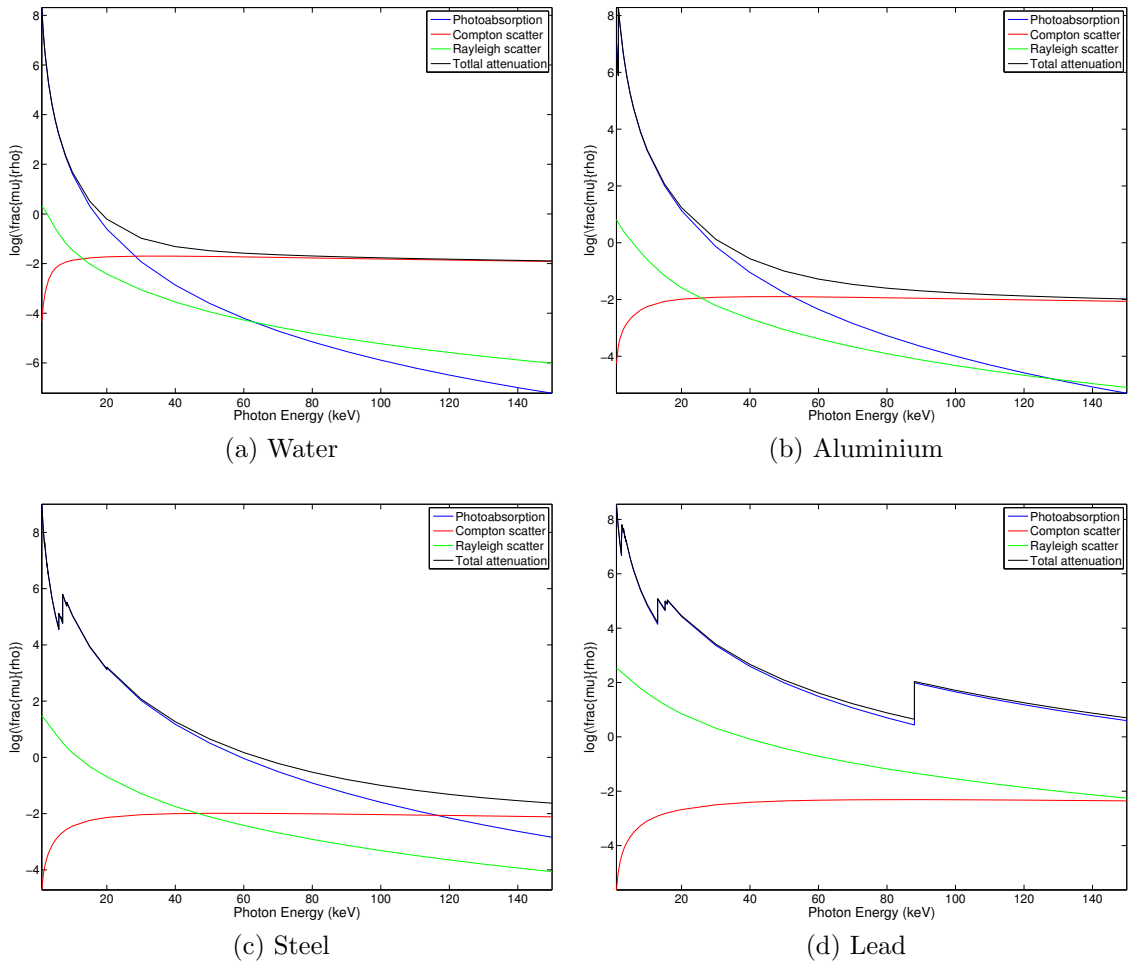

(a) Water (b) Aluminium

(c) Steel (d) Lead

Figure 5.5: Cross sectional data

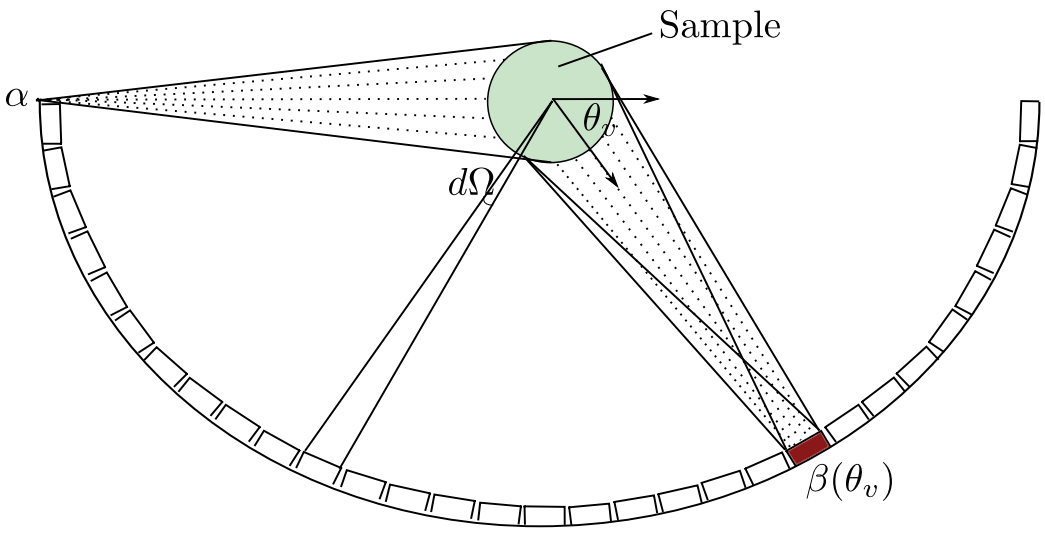

Figure 5.6: Scatter distribution from a spherical voxel

Figures 5.7, 5.8 and 5.9 display the angular scatter distributions for each sample material for sphere and cylinder samples in 400mm of air and the cylinder sample in a vacuum respectively. Although the scattered energy in the distributions changes slightly depending on the sample shape and whether the experimental region is a vacuum or filled with air, the overall trend is the same, illustrated in Fig. 5.10 for the sphere in 400mm of air. The results agree with the NIST reference data, Fig. 5.5.

The scattering distributions in the correction method are from an area and not a point. This implies that they will depend both on scattering and photoabsorption cross sections. The scattered energy increases for each material as the photoabsorption cross-section decreases. When scatter becomes the dominant process, at approximately 30keV, 50keV and 110keV for water, aluminium and stainless steel respectively, the scattered energy becomes almost constant. Photoabsorption, at these energies, is always the dominant process for lead and so there is little change in the scattered energy.

When the scattering cross-section dominates for each material, the energy differences are due to the density. Aluminium is more dense than water and so becomes the most scattering material at 50keV and stainless steel is more dense than aluminium, becoming the most scattering material above 110keV.

Changing the sample from spherical to cylindrical has an effect on the distribution energies as the cylinder covers a larger area of the scattering voxel. If scattering is the dominant process for a material at a particular energy, then the larger area will slightly increase the scattered energy. If photoabsorption is the dominant process then the scattered energy will decrease slightly as more of the photons are absorbed.

Changing from an experimental region with air to a vacuum lowers the energy slightly due to increased scatter from air molecules.

Calculating the solid angles

The solid angle that a detector subtends with the centre of a voxel is effectively a measure of how much the voxel 'sees' of the detector face. This will depend on the position of both the voxel, $v_c \in \mathbb{R}^3$, and the detector, $\beta \in \mathbb{R}^3$ and must be calculated

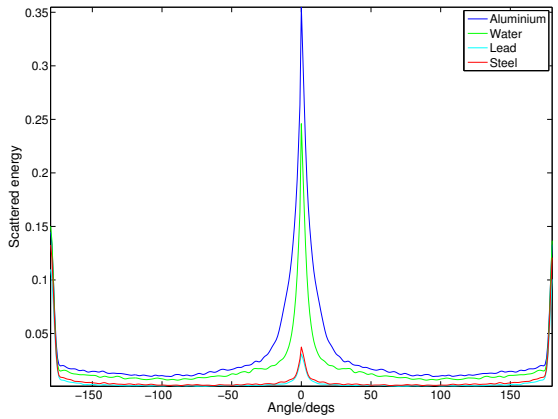

(a) 50keV

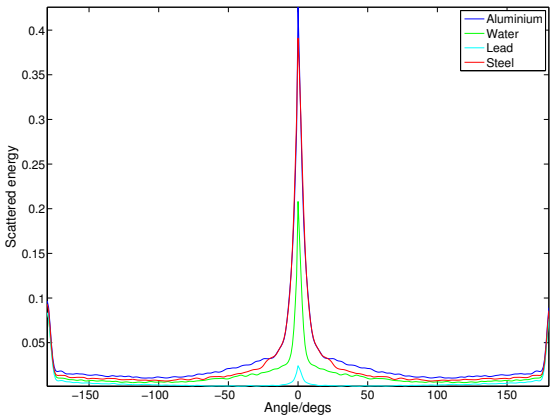

(b) 100keV

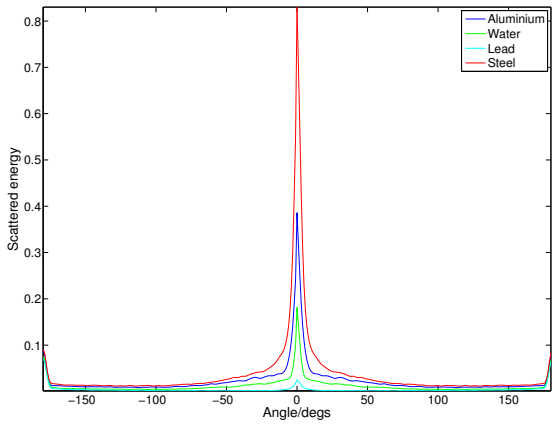

(c) 150keV

Figure 5.7: Angular scatter distributions for a spherical sample in air

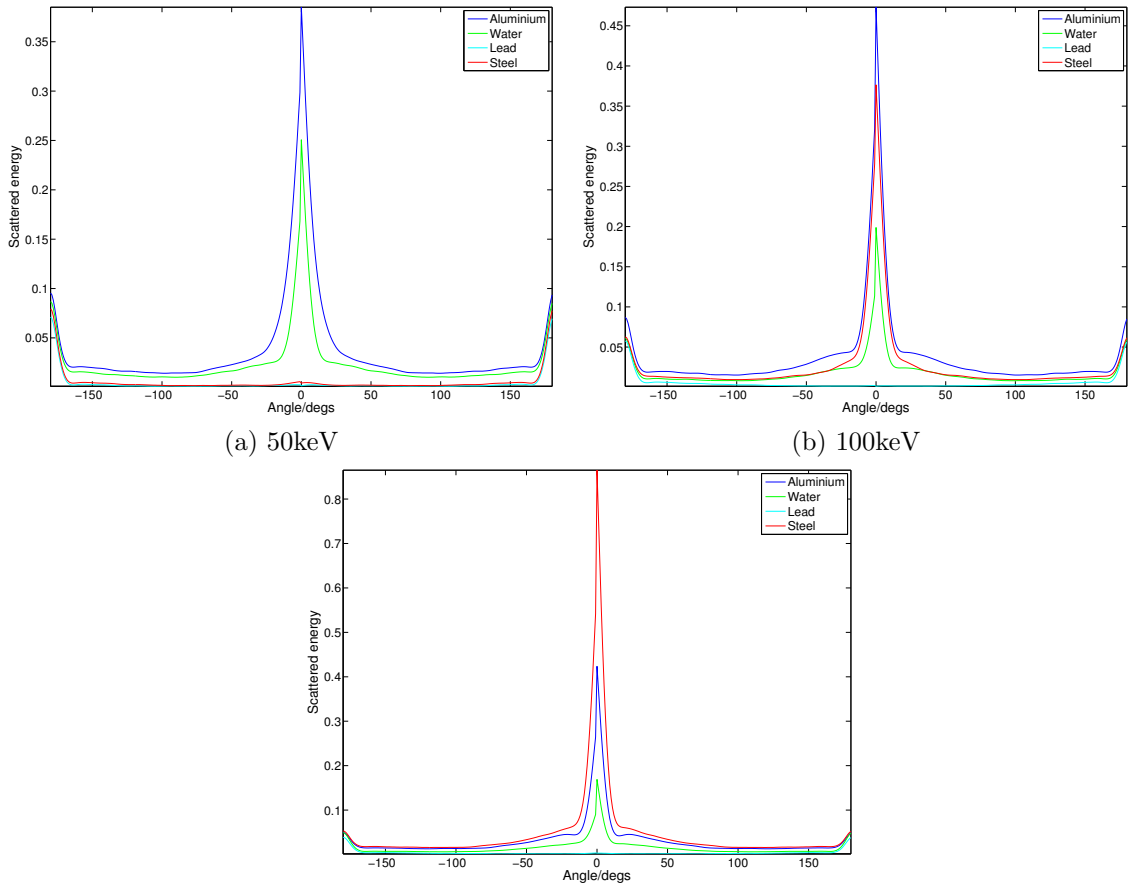

(a) 50keV

(b) 100keV

(c) 150keV

Figure 5.8: Angular scatter distributions for a cylindrical sample in air

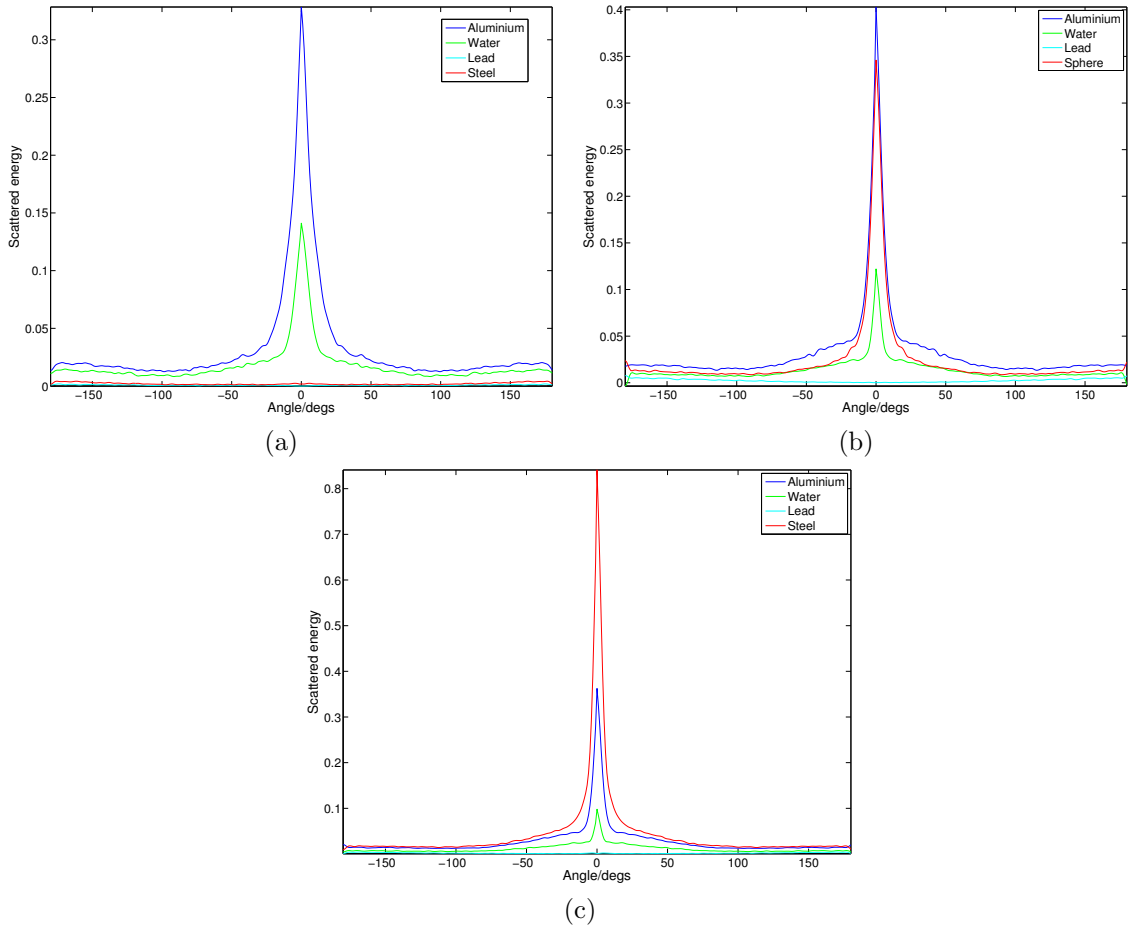

Figure 5.9: Angular scatter distributions for a cylindrical sample in a vacuum

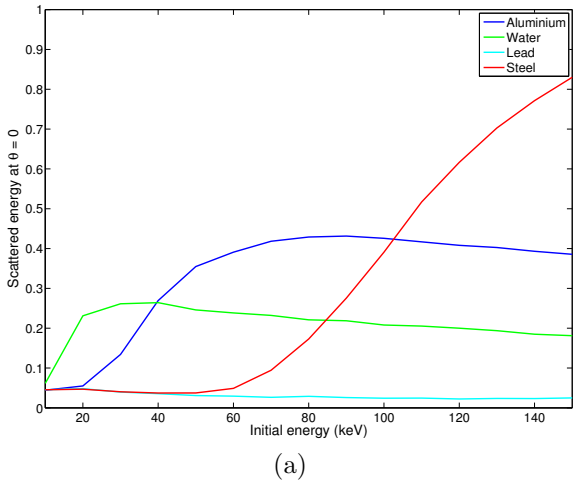

Figure 5.10: Scattered energy at $\theta = 0$

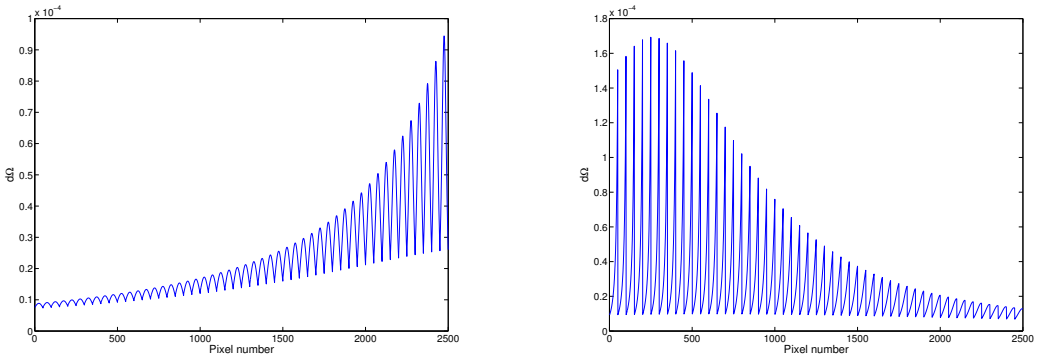

(a) Detector 1 (b) Detector 384

Figure 5.11: solidAngles subtended by a detector to all voxels

for each voxel-detector pair. $d\Omega_{\beta_s}$ does not change over the source projections.

For a large voxel-to-detector radius, r, and a small detector area, A, the subtense can be approximated by:

$$d\Omega_{\beta s}(\beta, v_c) = \frac{A\cos(\phi(\beta, v_c))}{r(\beta, v_c)^2}, \tag{5.24}$$

where $A\cos\phi$ is the projection of the detector face onto the plane parallel to the line from the centre of the voxel to the centre of the detector face. Fig. 5.11 illustrates the solid angle that two of the detectors subtend with all the voxels.

Calculating the scatter angles

Scatter angles are calculated in each source projection for each voxel-detector pair. As mentioned previously, this is the angle made at the centre of the scattering voxel between the ray from the source and the scattered ray in the direction of the centre of the detector.

If the source position is given by $\alpha \in \mathbb{R}^3$, then two unit vectors θ_1 and θ_2 are calculated such that,

$$\theta_1 = (\alpha - v_c)/r_1,$$

$$\theta_2 = (v_c - \beta)/r_2,$$

where,

$$r_1 = \sqrt{\sum (\alpha - v_c)},$$
$$r_2 = \sqrt{\sum (v_c - \beta)}, \tag{5.25}$$

and,

$$\theta_v(\alpha, \beta, v_c) = \arccos(\theta_1 \cdot \theta_2). \tag{5.26}$$

Calculating the scatter intensity

The intensity of scatter, I_v, that each voxel contributes to the image will depend on the acquisition data as it is equal to the sum of all the intensities recorded in the shadow of a voxel on the detector plane. The detectors in each voxel shadow are consistent for each imaged object and can be determined in advance, minimising the calculations of the scatter correction method after acquisition. The voxels are considered to be spherical for these calculations, making an elliptical shadow on the detector plane. Some of the voxels will only be partly covered by the x-ray beam and others will not be covered at all.

In summary, this method approximates scatter from 1cm^3 voxels, rather than using a point scatter approximation. The scatter distributions are calculated in advance using a Geant4 Monte Carlo approximation, and the intensity of scatter from each voxel is based on the acquisition data. By approximating scatter from a small voxel rather than a point, the number of calculations required to estimate the scatter is reduced. Similarly, by making the assumption that the scattered rays are attenuated like those in the forward direction, this removes the computationally expensive task of calculating ray paths through the object. If there are few scattering regions within a section of the object, there will be few calculations to compute.

In the following chapter scatter estimates are calculated, using the method described

here, from a few test objects which were simulated with the Geant4 Monte Carlo code described in Chapter 2.

Chapter 6

Results of the Scatter Correction Method

The scatter correction method is applied to two test objects, a water box and a test suitcase. The objects were simulated with the Geant4 Monte Carlo code described in Chapter 2, with a similar experimental set-up as for the scatter test objects in Chapter 3. A full rotation of each object was simulated for every fourth source projection of the RTT machine, with multiple detector rings.

In Chapter 3, large bodies of water were shown to be highly scattering and so provide a good initial test object for the scatter correction method. The method is initially tested under ideal conditions, where the object is homogeneous, the initial photon energy is monoenergetic and the scattering object fits exactly within the discretised scattering voxels. The test object is a 200mm×200mm box of water, extending infinitely (that is, extending beyond the beam coverage) in the third-dimension, placed at the centre of the scanning region, and each photon has an energy of 100keV to remove the effects of beam hardening.

The second test object is simulated under more difficult conditions to test the robustness of the algorithm. The simulated object is inhomogeneous and consists of a 450mm×450mm box filled with cotton, with a 2mm outer rim of PVC. This suitcase is filled with four objects displayed in Fig. 6.1. A 120mm×70mm box of aluminium, a 100mm×100mm box of water, a 80mm×80mm box of stainless steel and a lead

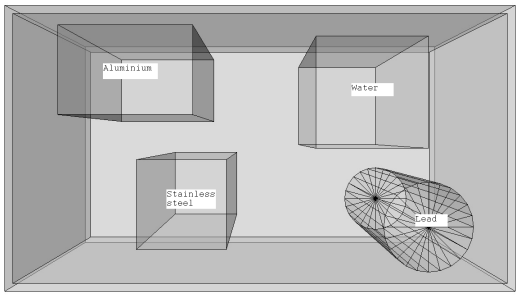

(a)

Figure 6.1: Test suitcase

cylinder with a 80mm radius. Again all objects are extended infinitely in the third dimension. The object is placed slightly above the isocentre, where the conveyor belt would be and the objects are positioned so they do not fit exactly within in the scattering voxels.

The scatter correction estimate is obtained for the four inside objects only, assuming that scatter from the cotton and thin PVC rim is low. To simulate all the pixels would be computationally expensive. In order to further analyse the method, the test suitcase is broken down into separate components, and simulated for three projections, equally spaced around the source ring. First, the cotton and PVC rim are removed, leaving only the four internal objects. Then each of the four objects is simulated separately for close analysis. The scatter estimates took less than three seconds to compute per projection and there is room for further optimisation. The normalised x-ray energy spectrum, $\bar{I}_p(E)$, was assumed to start at 40keV.

6.1 Water box

All the scattering voxels within the water box are included in the scatter correction. First the intensity of each scattering voxel, I_v, is found, in each projection, by summing the total recorded energy in the detectors in the voxel shadows from the simulated projection data. This must be calculated for each scattering voxel in each of the four cross-sectional slices. Fig. 6.2 illustrates the voxel slice numbering and

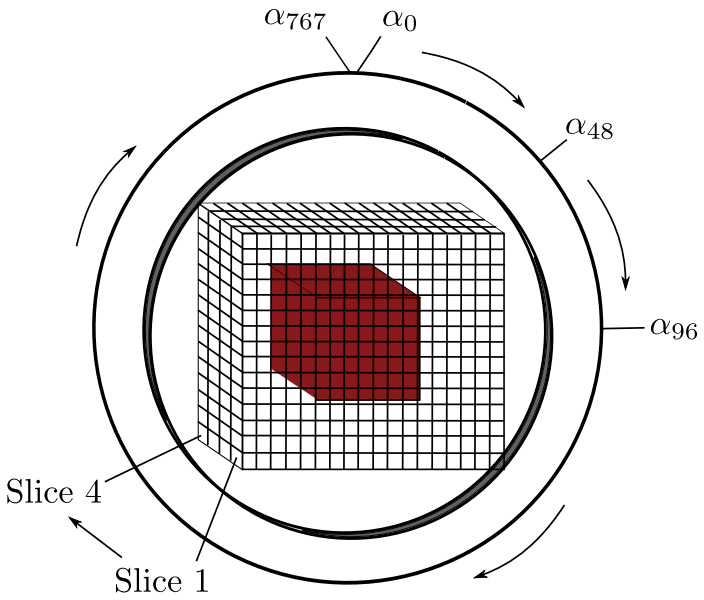

Figure 6.2: Test suitcase

the position of each source projection. There are a total of 768 source projections, denoted here by α_i with $i = 0. \ldots, 767$.

The results of the voxel intensities in the whole discretised scattering region are displayed in Fig. 6.3 for each voxel slice for source projection 0. There are few voxels covered by the beam in slices one and four, and in the area of the water box, Fig. 6.4 there is no coverage at all. So only slices two and three are considered in this instance. For the remainder of this section the results are displayed for three projections equally spaced in the first quarter of the source ring (α_0, α_{48} and α_{98}), more results are available in Appendix B. The results are similar in each quarter as the box is placed at the centre. For voxels outside of the attenuating region, where no rays have passed through the object, it is apparent in Fig. 6.3, that the intensity in the voxels closer to the source have a higher beam coverage due to the inverse square law drop off of the intensity of the beam.

Fig. 6.5, shows the intensity each voxel contributes to the scatter correction, with the intensity of all voxels outside of the water box set to zero. Results for voxel slice two are along the top and voxel slice three along the bottom. It is the edges of the object, depending on the source rotation, that contribute the most scatter to the correction. The rays passing through the corners of the box have the shortest path

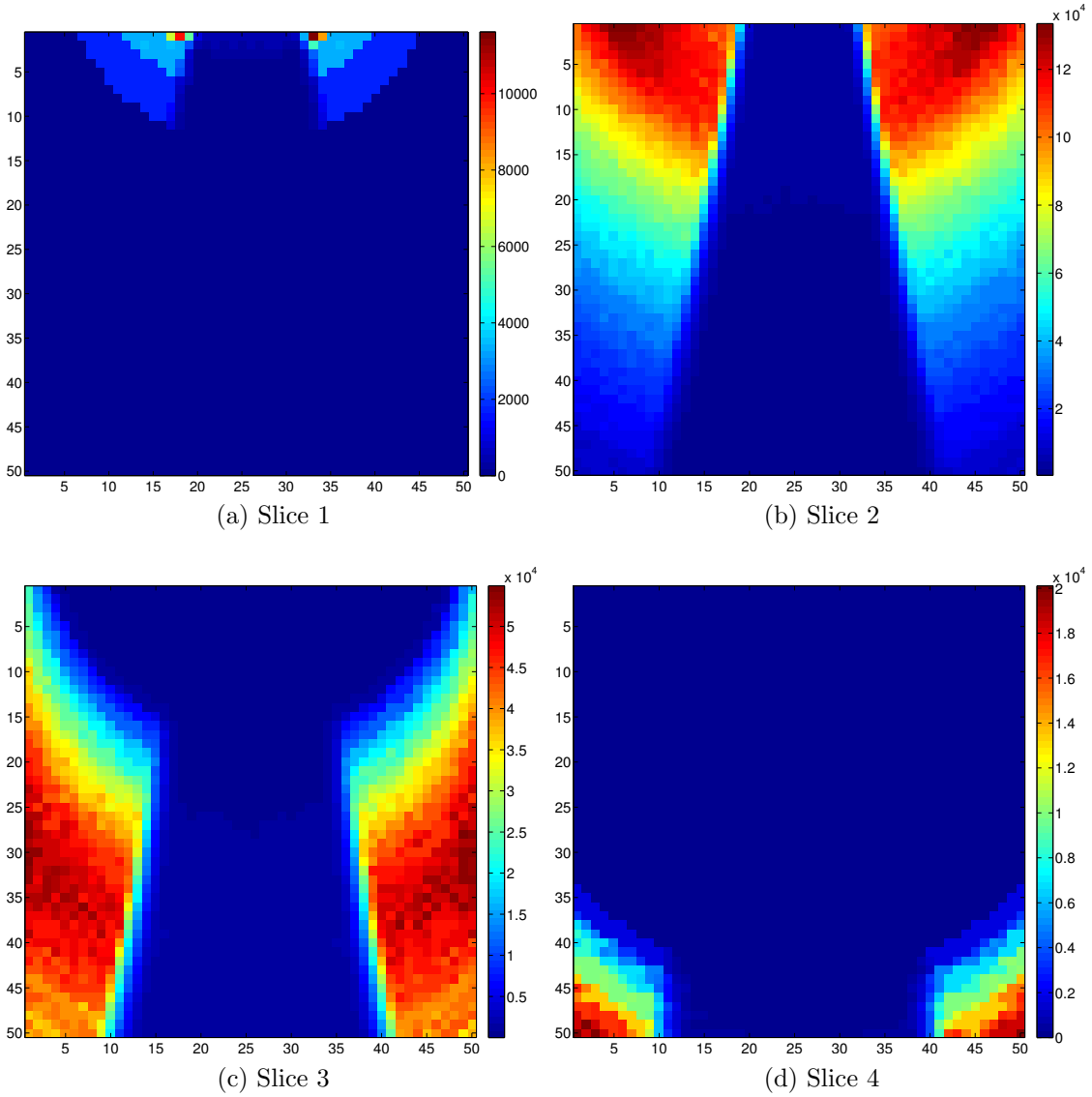

(a) Slice 1

(b) Slice 2

(c) Slice 3

(d) Slice 4

Figure 6.3: Water box: Voxel intensities for source projection 0

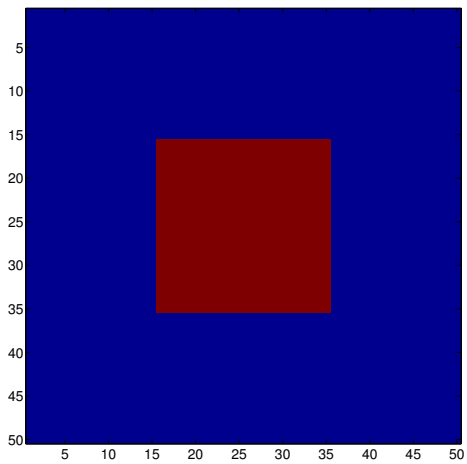

Figure 6.4: Water box scattering voxels

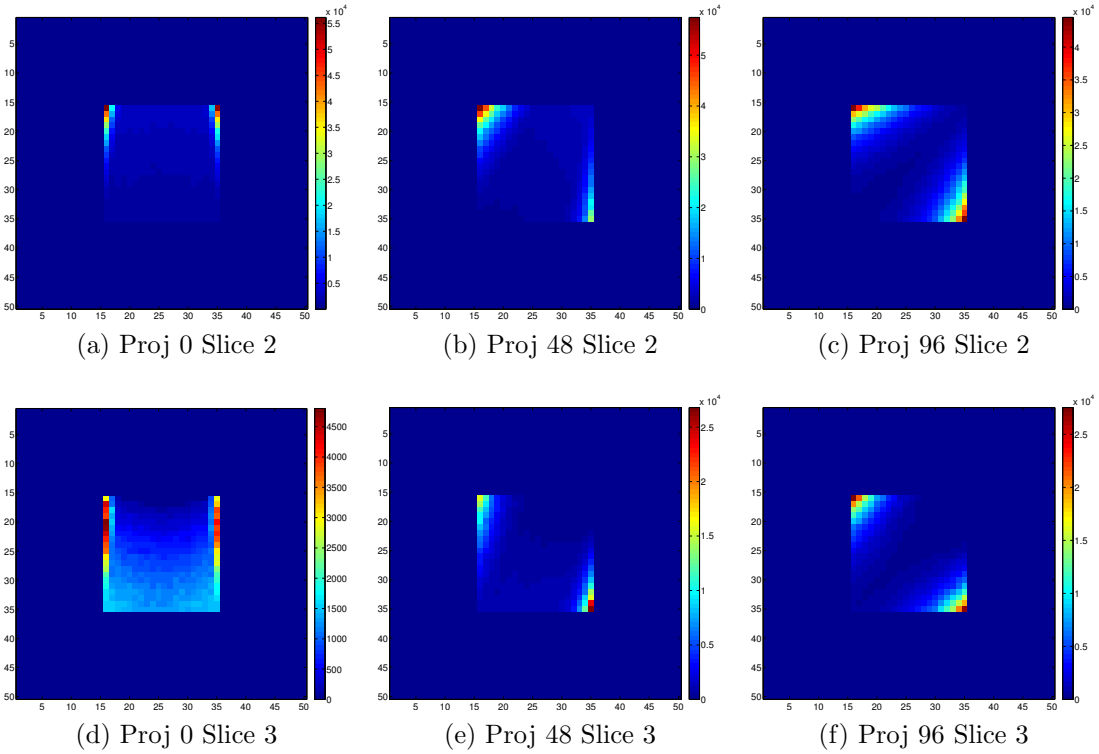

(a) Proj 0 Slice 2 (b) Proj 48 Slice 2 (c) Proj 96 Slice 2

(d) Proj 0 Slice 3 (e) Proj 48 Slice 3 (f) Proj 96 Slice 3

Figure 6.5: Water box: Scattering voxel intensities

through the object and are attenuated the least. The high intensity voxels do not necessarily contribute the most to the reconstructed image, as it is the scatter rays in areas of low attenuation, that lead to the largest error. It is the area in the shadow of the object that we are concerned with, where photoabsorption is higher.

The results of the simulated data are displayed in Figures 6.6, 6.7 and 6.8, where image (a) shows single, multiple and total scatter recorded for each projection. The data is statistical in nature but a clear pattern can be seen in each case and a smoothing spline has been applied for easier comparison. Image (b), in each figure, plots the log of the primary along with the single scatter component, to illustrate which part in each projection we are interested in. It is only the areas where the photoabsorption is high that scatter will cause significant errors in the image. Detectors need only be considered in the active region.

The results of the scatter correction method applied to the water box are displayed in Fig. 6.9, for both the spherical and cylindrical water samples at 200mm and 400mm in air. The results show a good approximation to the single scatter component, for

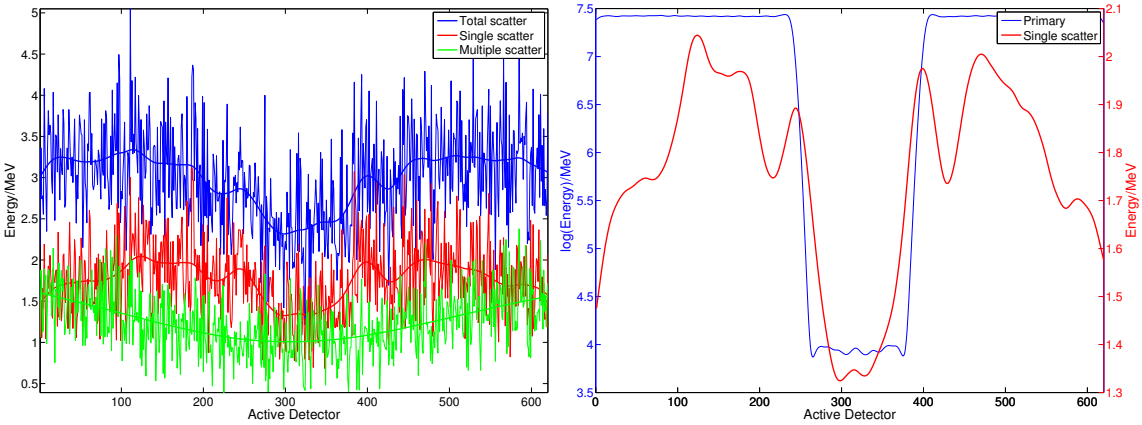

(a) Scatter and smoothed scatter (b) Primary and single scatter

Figure 6.6: Water box: Simulated data for source projection 0

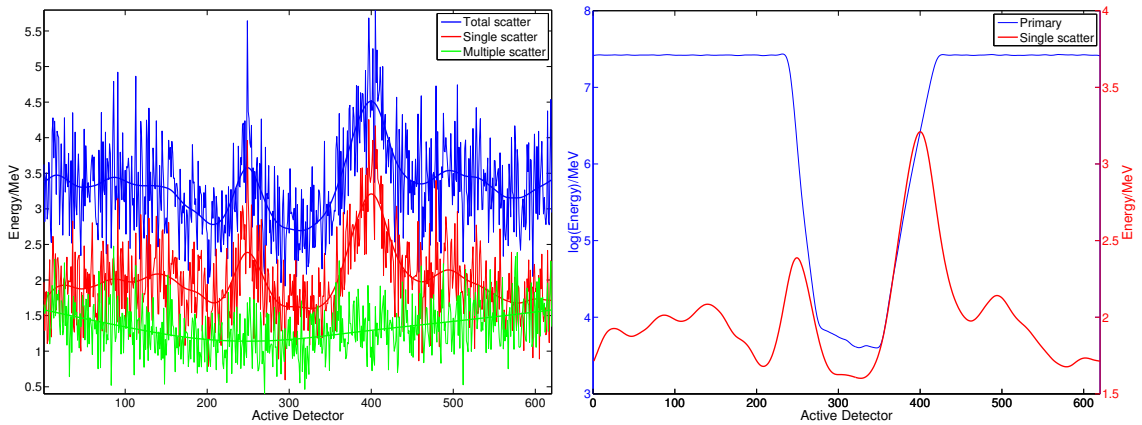

(a) Scatter and smoothed scatter (b) Primary and single scatter

Figure 6.7: Water box: Simulated data for source projection 48

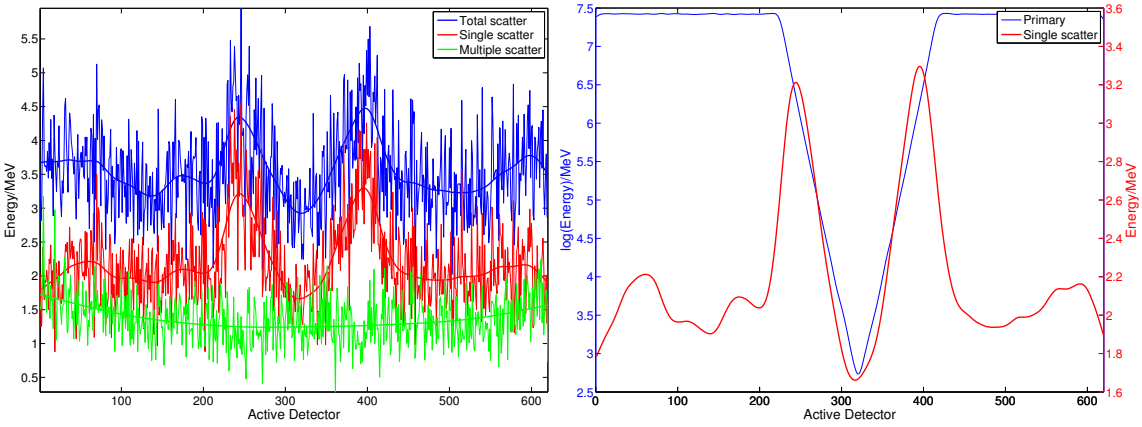

(a) Scatter and smoothed scatter (b) Primary and single scatter

Figure 6.8: Water box: Simulated data for source projection 96

all projections in the area behind the object. Let x_{sim} denote the simulated total scatter signal and x_{est} denote the scatter estimate by a cylinder sample with a 200mm detector distance, then the error ϵ is defined as.

$$\epsilon = x_{sim} - x_{est}, \tag{6.1}$$

The percentage of the total scatter signal that is reproduced by the scatter algorithm is given by $(1 - \epsilon)$ and displayed in Fig. 6.10 for projection 0. The approximation reproduces over 60% of the simulated total scatter signal in the most attenuating regions behind the object, and is similarly above 60% for all other projections.

The cylinder sample in 200mm of air provides the closest approximation to the single scatter component, and the cylinder in 400mm of air is the closest approximation to the total scatter. For these results it is clear that both the size of the sample, and the length of the scattered rays through air in the scatter distributions can make a significant difference. The cylindrical 400mm estimate is higher than the single scatter component, as multiple scattered photons from the small sample are contained within the scatter distribution.

The peaks in the data are due to scattering from voxels at the edges of the object, which were shown previously to contribute a greater intensity. It is assumed that the missing scatter at the edges of the active region is due to the assumption that all rays after scattering are attenuated like those in the forward direction. For rays passing all the way through the object close to the edges, a scattering event near the top of the object can lead to a very short subsequent attenuation path through the object. The ray in the forward direction, however, will have a much longer journey and will be much more highly attenuated than the scattered ray. This assumption however, does not compromise the scatter correction method as it is the area behind the object where a good approximation is desired.

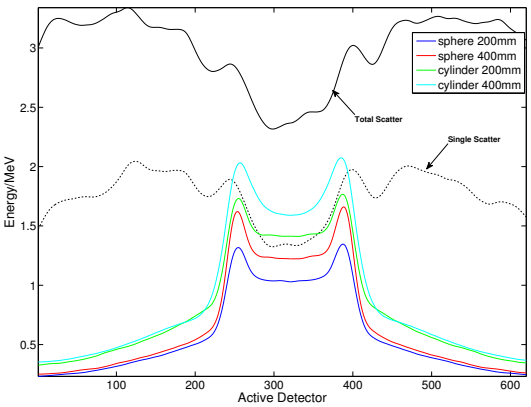

(a) Projection 0

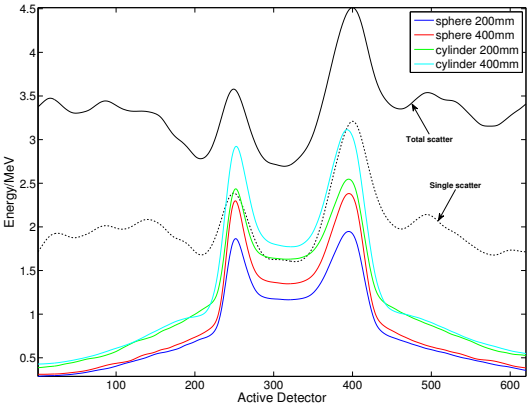

(b) Projection 48

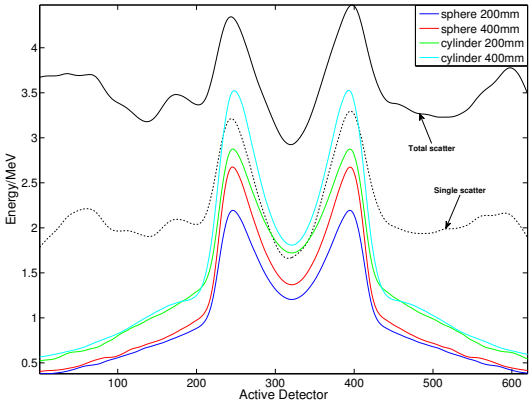

(c) Projection 96

Figure 6.9: Water box: Scatter approximation

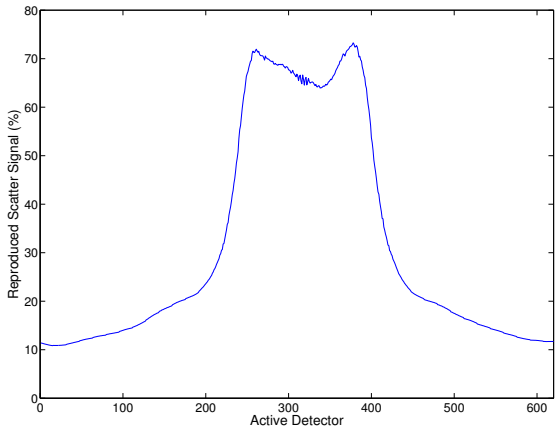

Figure 6.10: Reconstructed scatter signal

6.2 Test suitcase

The scatter correction results for the test suitcase, simulated with a 150kVp polyenergetic spectrum are presented here. The intensites of each voxel for the test suitcase, Fig. 6.11, for source projection 0, show that more voxels are affected by the object attenuation than for the water box. Similarly, voxel slices one and four contribute little to the data, but a few projections do incorporate slice four. Only the four objects are considered within the scatter correction method and the suitcase itself is ignored. Fig. 6.12 shows the scattering pixels that contribute to the correction method. A voxel is chosen to be scattering if its centre lies within a scattering region, and as the objects do not perfectly fit within these pixels their shapes change slightly. This is clearly evident for the lead cylinder.

The intensities to the chosen scattering voxels only, with all other set to zero, are displayed in Fig. 6.13 for three source projections equally spaced around the source ring (α_0, α_{256} and α_{512}), for voxel slice two at the top and voxel slice three at the bottom. The contribution each voxel makes is very different for each source projection and voxel slice. This depends on the how many objects each ray passes through, and therefore how much it is attenuated. Still, it is the corners of the objects that provide the highest intensities, these highest intensites being much lower than those for the water box.

The simulated data for each of the three projections is displayed in Figures 6.14, 6.15 and 6.16. Image (a) in each figure displays separate scatter contributions for each projection and image (b) shows the primary with the single scatter to illustrate the regions of interest. The single and total scatter contributions have a clearly defined shape, differing over the projections. The total scatter recorded is lower than the water box, but the primary beam is also much lower. The large majority of scatter in this instance is due to single scattering events and there is little primary signal.

Fig. 6.17 displays the scatter estimate against the smoothed simulated scatter data, for the sphere and cylinder samples in 400mm of air. More results are available in Appendix B. The cylinder sample proved to be the best approximation for the water

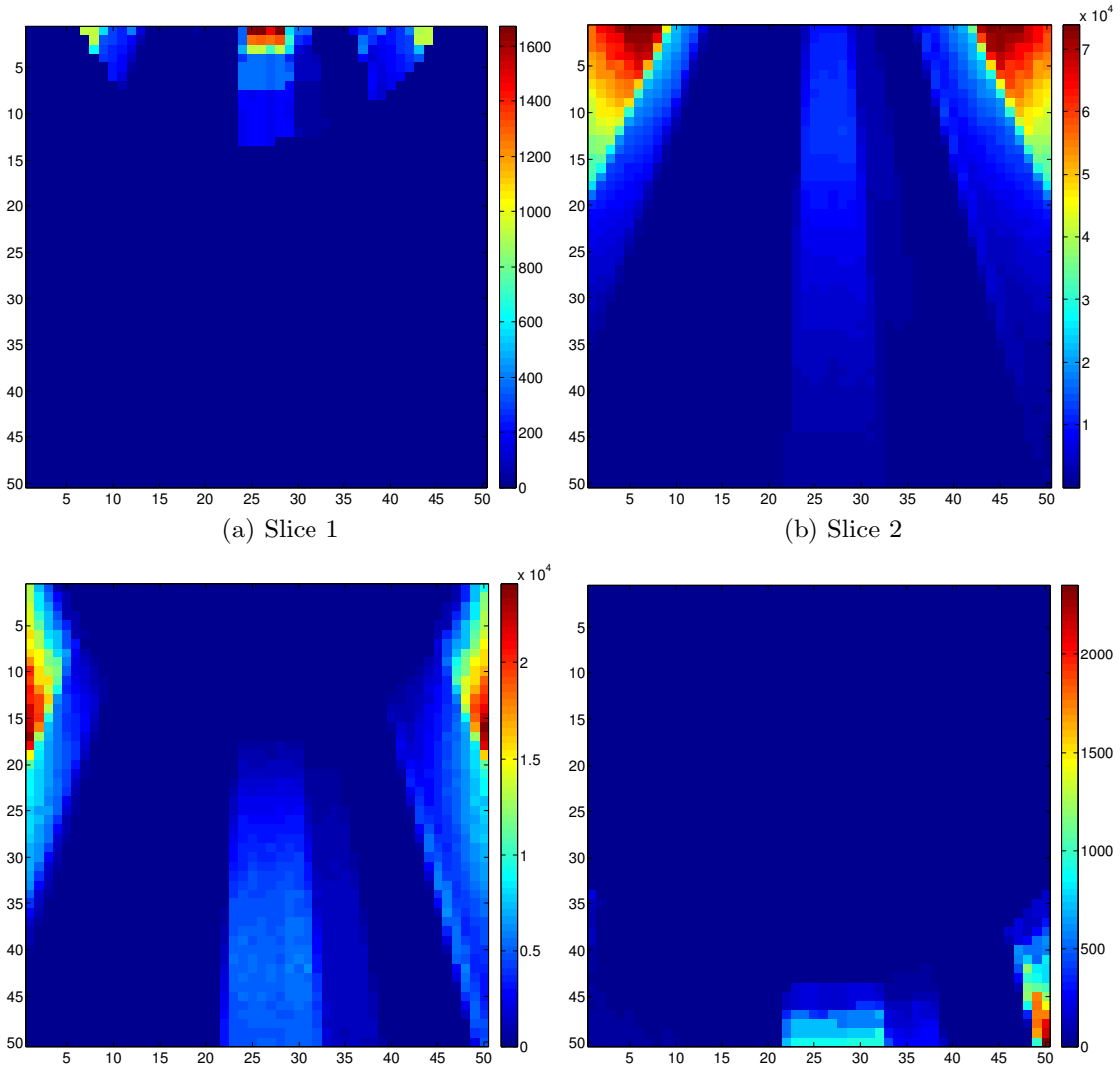

(a) Slice 1 (b) Slice 2

(c) Slice 3 (d) Slice 4

Figure 6.11: Test suitcase: Voxel intensities for source projection 0

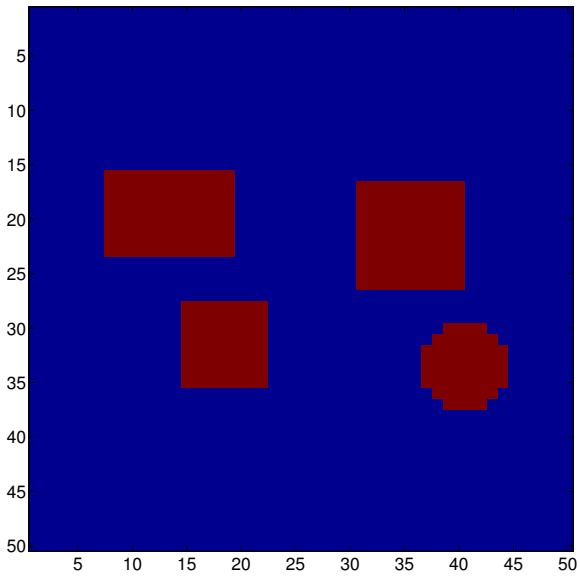

(a)

Figure 6.12: Test suitcase scattering voxels

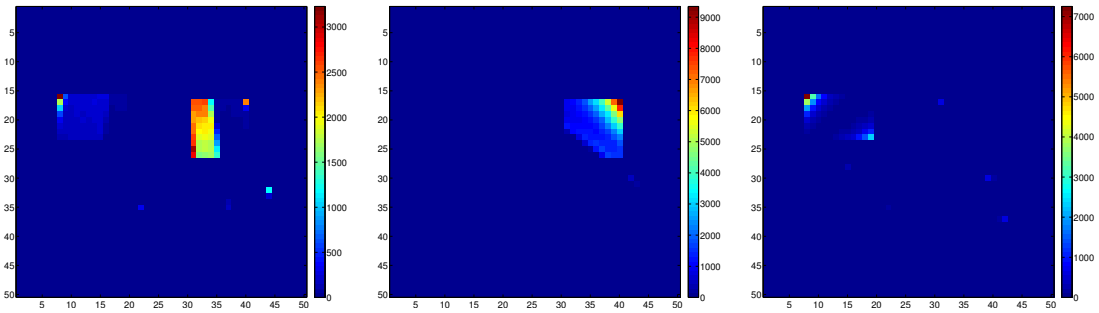

(a) Projection 0 (b) Projection 256 (c) Projection 512

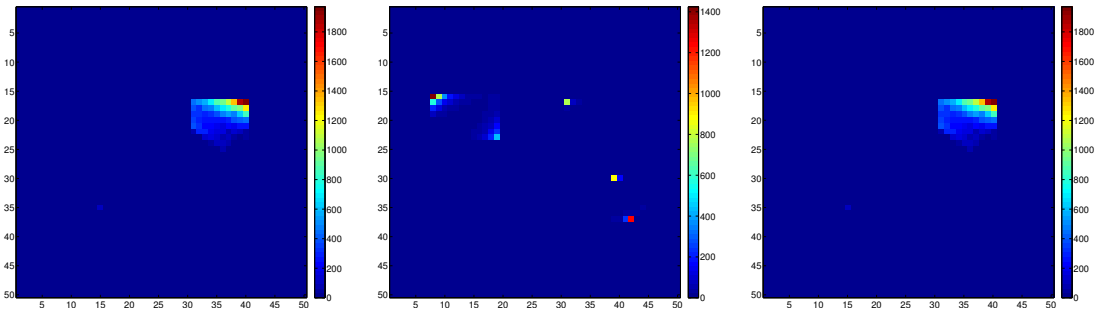

(d) Projection 0 (e) Projection 256 (f) Projection 512

Figure 6.13: Test suitcase: Scattering voxel intensities

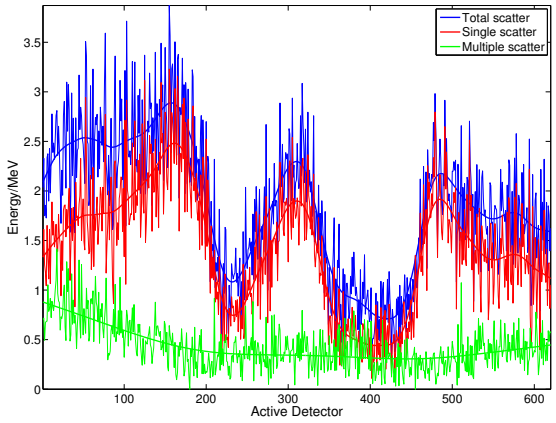

(a) Scatter and smoothed scatter

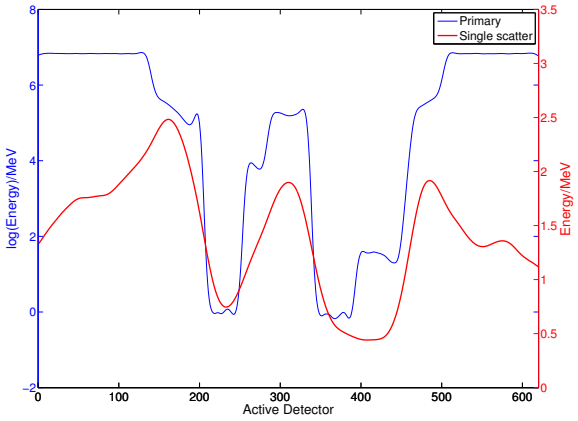

(b) Primary and single scatter

Figure 6.14: Test Suitcase: Simulated data for source projection 0

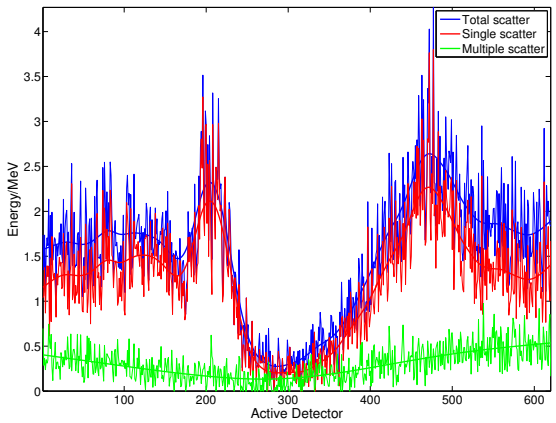

(a) Scatter and smoothed scatter

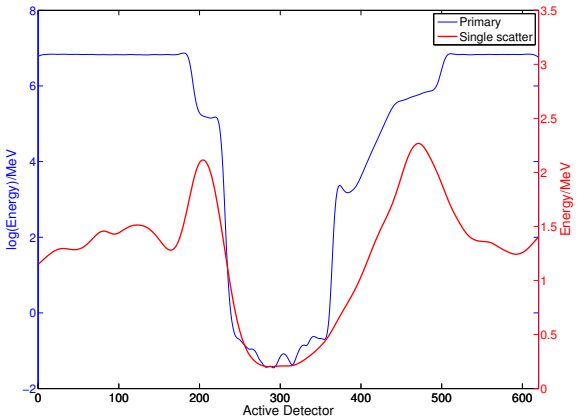

(b) Primary and single scatter

Figure 6.15: Test Suitcase: Simulated data for source projection 256

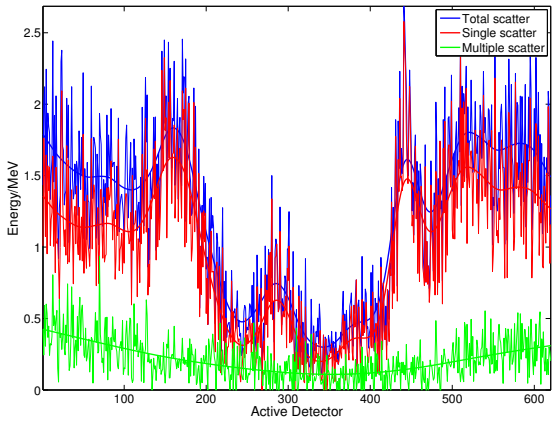

(a) Scatter and smoothed scatter

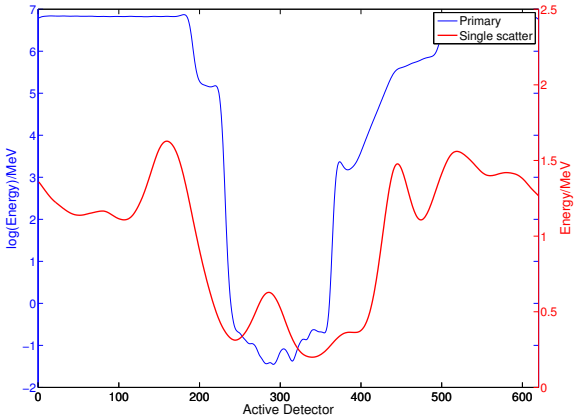

(b) Primary and single scatter

Figure 6.16: Test Suitcase: Simulated data for source projection 512

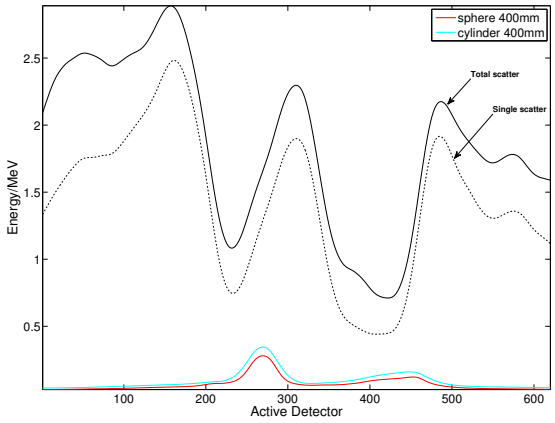

(a) Projection 0

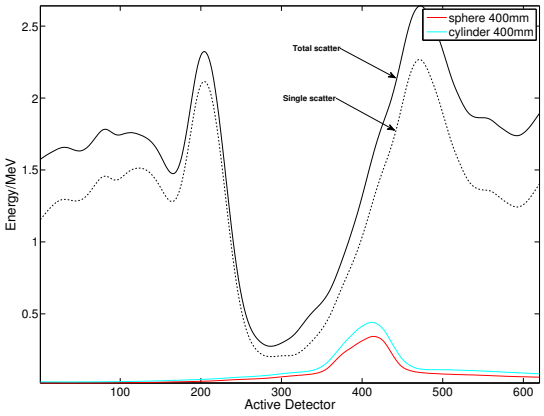

(b) Projection 256

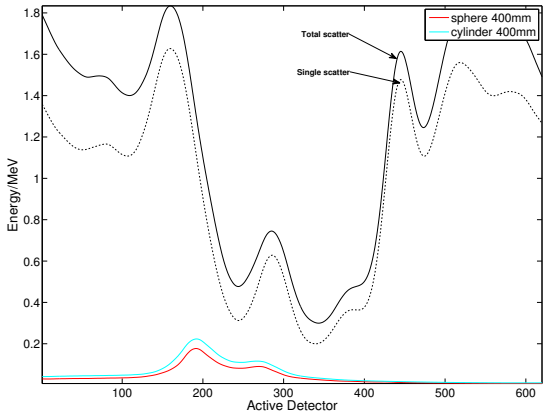

(c) Projection 512

Figure 6.17: Test suitcase: Scatter approximation

box, and the sphere sample is plotted to illustrate the differences due to sample size. Although the estimate follows a similar trend to the simulated data, it is much too low and does not provide a good approximation. Between 12% and 30% of the total simulated scatter signal is reproduced by the estimate, is highly attenuating areas. There are two main problems that are thought to affect the results. First, the objects do not fit exactly within the scattering voxels, this results in an increase in the voxel intensity if the size has been extended and a decrease if the size has been reduced. Second, the shadows of the voxels are assumed to be cylindrical which is the shadow of spherical voxels on the detector plane. This was calculated for simplicity, and to avoid over-estimating the voxel scatter intensity if the detector is not fully cover by the shadow.

To analyse these results further and to investigate the conditions under which the

scatter correction method provides good results, the following sections break down the test suitcase into separate components.

6.3 Four objects no suitcase

In order to investigate the errors caused by ignoring the suitcase and cotton, the four objects were simulated in air, without the surrounding. The intensity values to the scattering pixels, Fig. 6.18, are much higher in this instance compared to the test suitcase. When comparing the two total simulated intensities for the projection 0, it is clear that the rays are much more attenuated when they pass through the cotton suitcase, Fig. 6.19. The scatter component within the acquired data, in this instance, is also much lower than the test suitcase, Fig. 6.20. It is clear, from this analysis, that the suitcase can not be ignored.

The scatter correction compared to the simulated data provides a much better estimate when the suitcase is removed, Fig. 6.21. Projections 0 and 512 provide good approximations to the single scatter component in the areas behind the objects, reproducing up to 80% and 57% respectively. Projection 256 however, over-compensates for scatter. This is possibly due to the change in the object shapes. If a voxel is set to scattering and it is not fully covered by the scattering object the intensity value will be incorrect. Particularly if the rays passing by the edge of the object are not highly attenuated.

Results were also collected for the simulated four objects in a vacuum, to analyse the effects air has on the results. Fig. 6.22 displays the data for projections 256 and 512. The multiple scatter component appears to remain unchanged. However, there is significant change in the single scatter component, especially outside the object region where the rays are unattenuated by the object. There is a drop of approximately 8% at the peaks and as much as 35% at the edge of the active detector region.

The results of the scatter approximation obtained with sphere and cylinder samples similarly in a vacuum are display in Fig. 6.23. The estimate is even slightly lower than for the four objects in air, implying that either the scatter distributions or the

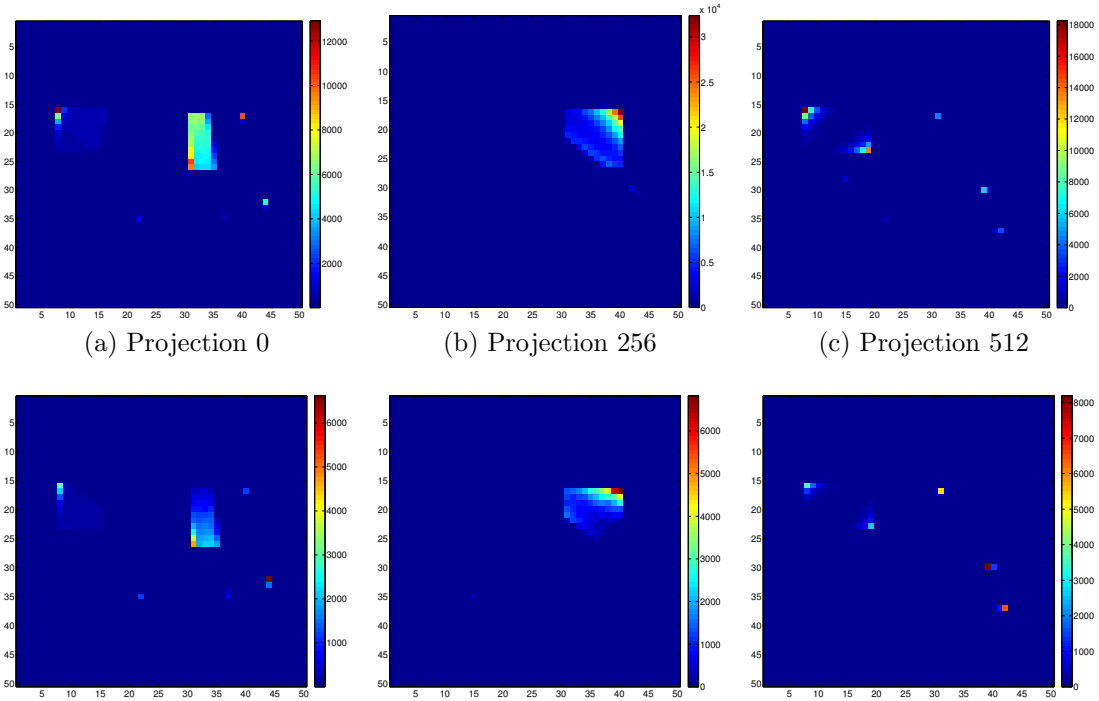

(a) Projection 0 (b) Projection 256 (c) Projection 512

(d) Projection 0 (e) Projection 256 (f) Projection 512

Figure 6.18: Four objects in air: Scattering voxel intensities

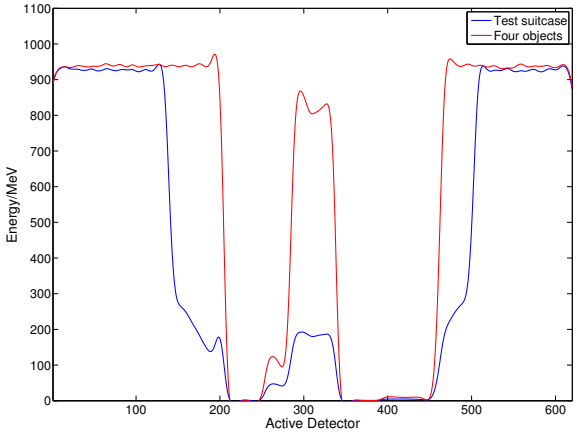

(a) Projection 512

Figure 6.19: Simulated total energy for test suitcase and four objects with no suitcase

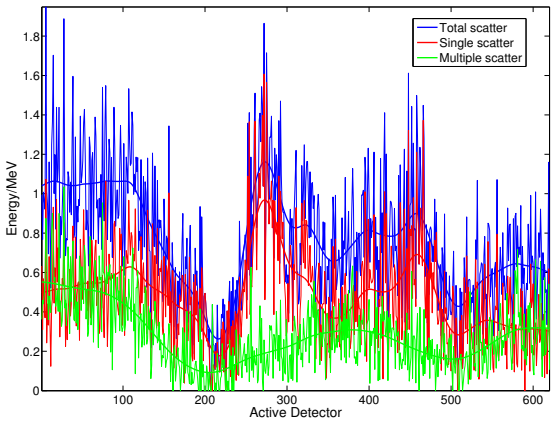

(a) Projection 0

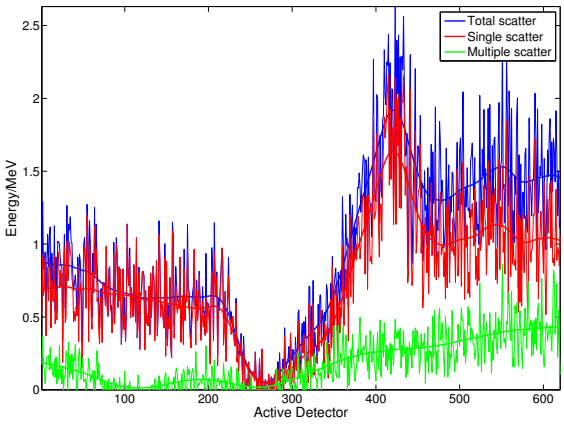

(b) Projection 256

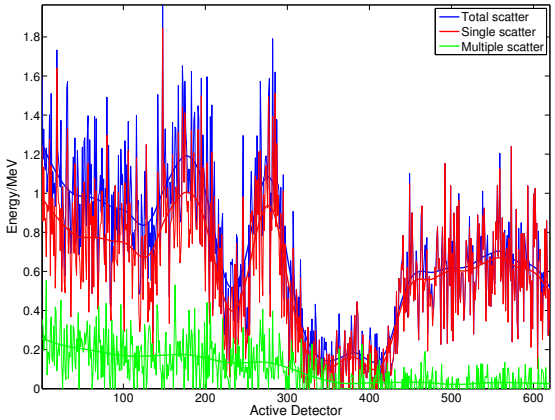

(c) Projection 512

Figure 6.20: Four objects in air: Simulated and smoothed scatter data

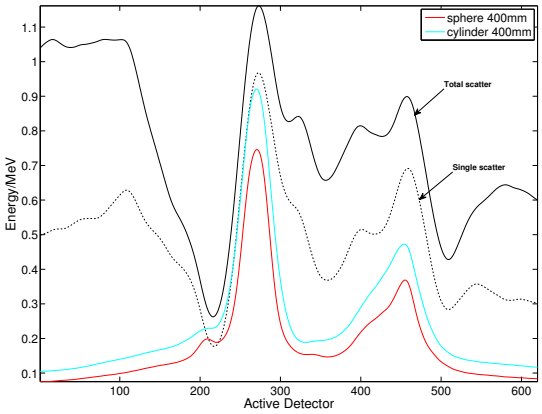

(a) Projection 0

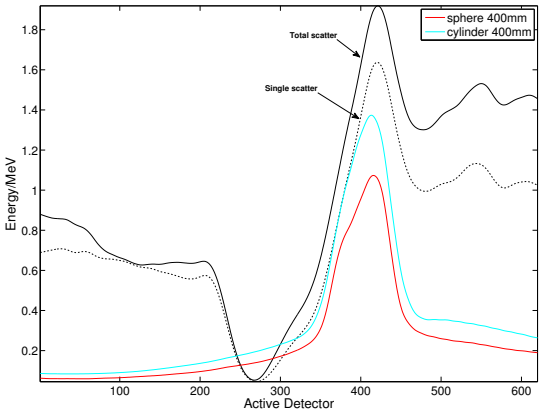

(b) Projection 256

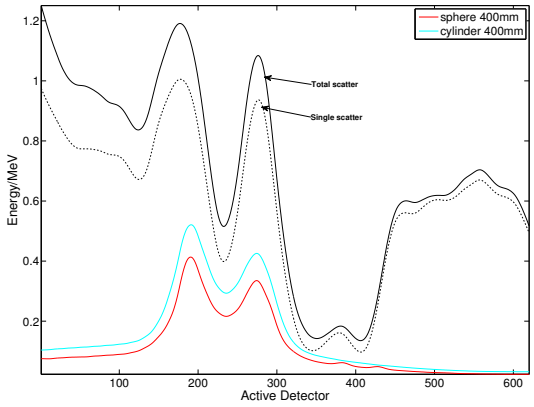

(c) Projection 512

Figure 6.21: Four objects in air: Scatter approximation

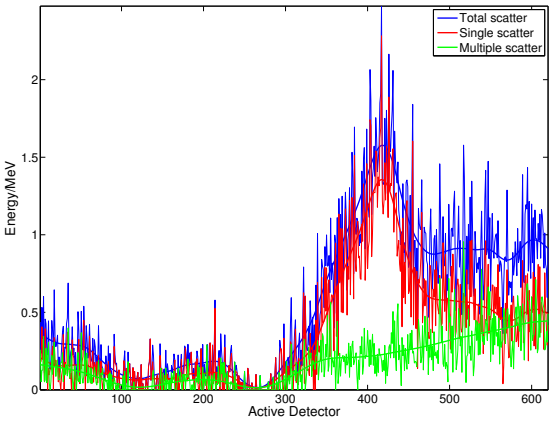

(a) Projection 256

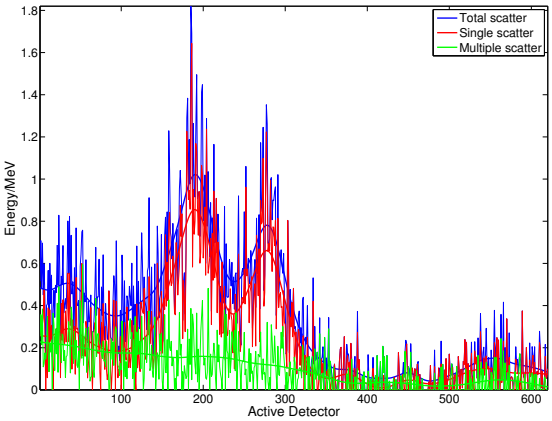

(b) Projection 512

Figure 6.22: Four objects in a vacuum: Simulated and smoothed scatter data

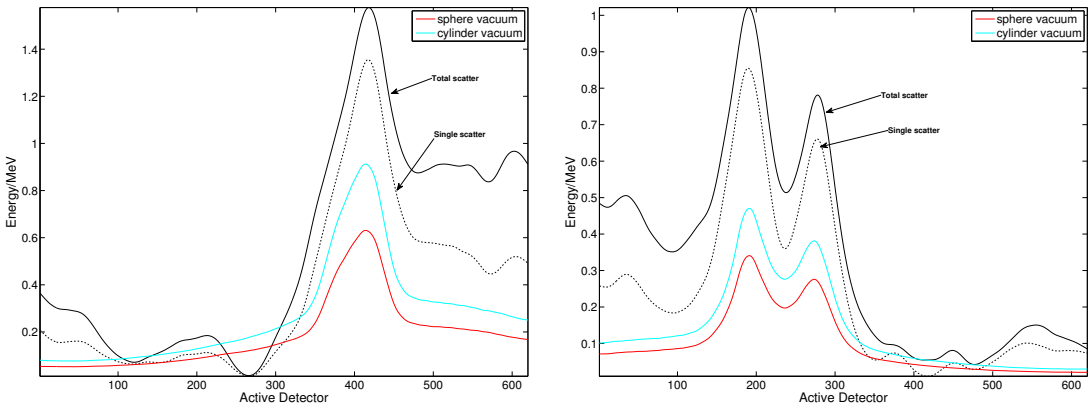

(a) Projection 256 (b) Projection 512

Figure 6.23: Four objects in a vacuum: Scatter approximation

intensity values are too low. Since the scatter distributions provided a good approximation to the water box it is likely that the intensity values are not correct. To investigate this further, scatter estimate are obtained for the four objects simulated separately.

6.4 Aluminium object

The aluminium object is simulated separately in air and in a vacuum. The voxel intensities shown in Fig. 6.24 show that the highest scattering points will be from the corners of the object. Figures 6.25, 6.26 and 6.25 show the separate scatter components, image (a), and the primary against the single scatter component, image (b), for the three projections in air. In the scatter data there at two peaks associated with the edges of the object.

The scatter estimate was obtained for the object in air and in a vacuum for the cylindrical sample in air and in a vacuum respectively. The estimate for the aluminium object in air is display in Fig. 6.28, and in a vacuum in Fig. 6.29. The estimates are still too low but they follow the general trend of the simulated scatter data in the area behind the object. Still, approximately 65%, 57% and 45% of the simulated scatter component is reproduced for projections 0, 256 and 512 respectively. Since the approximation is low in the vacuum case, it is the intensity that causes the

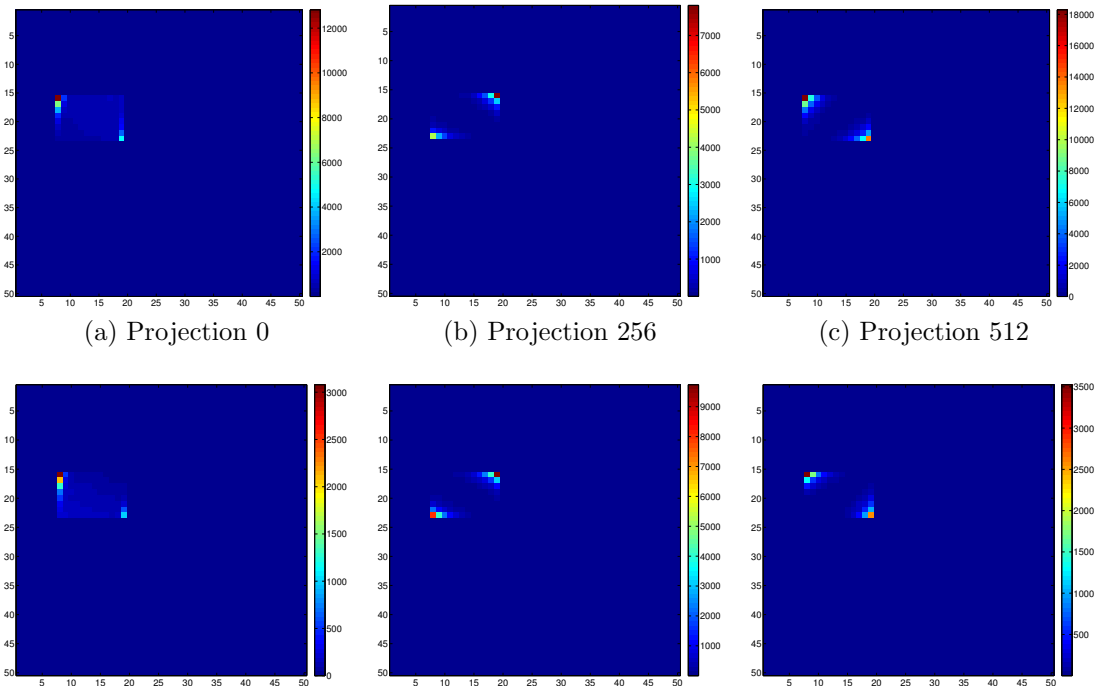

(a) Projection 0 (b) Projection 256 (c) Projection 512

(d) Projection 0 (e) Projection 256 (f) Projection 512

Figure 6.24: Aluminium object in air: Scattering voxel intensities

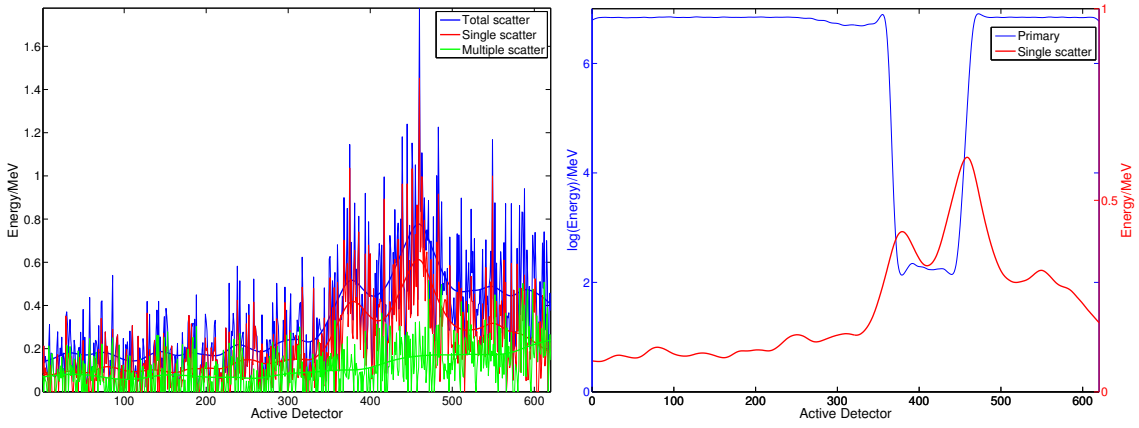

(a) Scatter and smoothed scatter (b) Primary and single scatter

Figure 6.25: Aluminium object in air: Simulated data for source projection 0

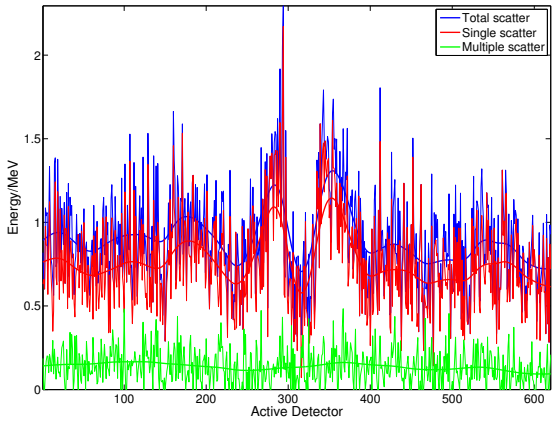

(a) Scatter and smoothed scatter

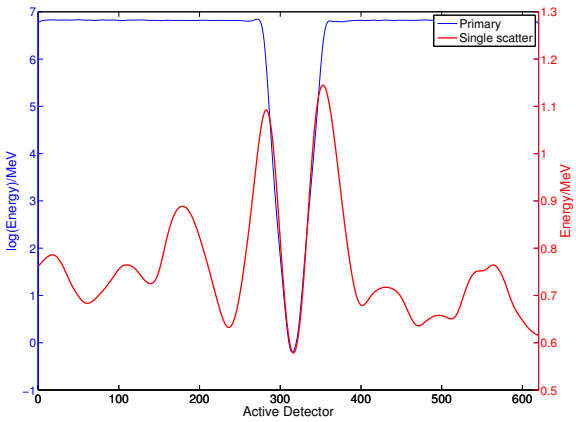

(b) Primary and single scatter

Figure 6.26: Test Suitcase: Simulated data for source projection 256

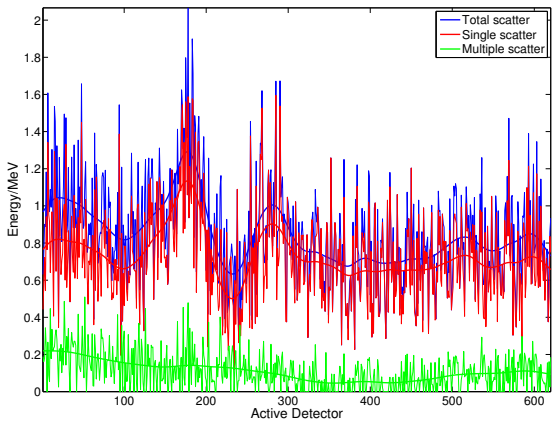

(a) Scatter and smoothed scatter

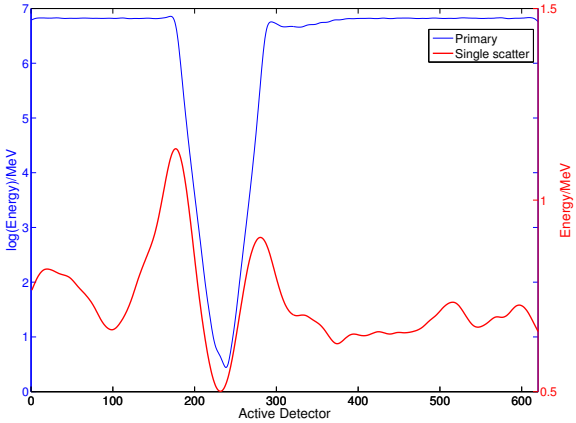

(b) Primary and single scatter

Figure 6.27: Test Suitcase: Simulated data for source projection 512

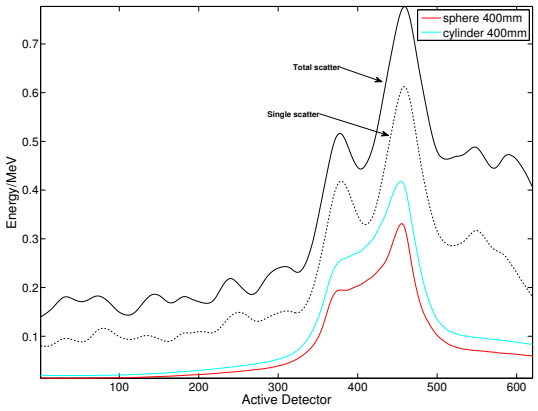

(a) Projection 0

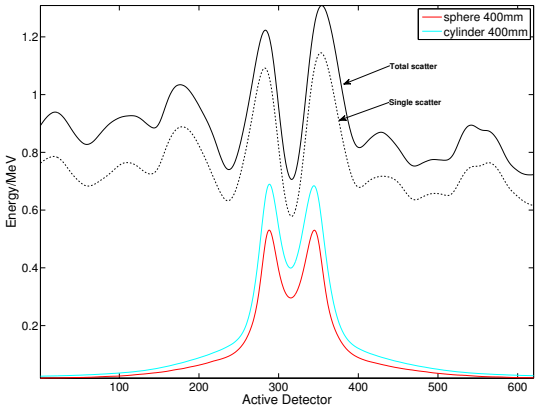

(b) Projection 256

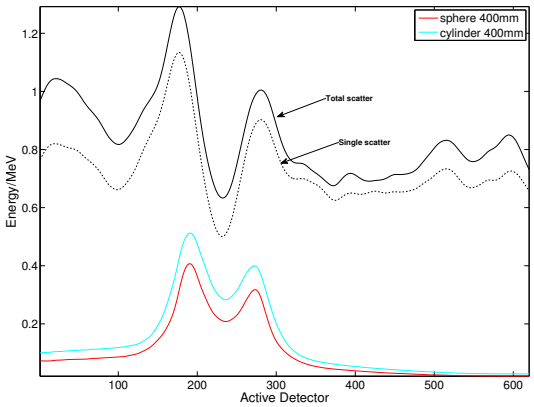

(c) Projection 512

Figure 6.28: Aluminium object in a air: Scatter approximation

problem here.

In Fig. 6.28a one of the peaks from scatter at the edge of the object is missing in the estimate. It can be seen from Fig. 6.24a that the right bottom corner voxel of the box has an intensity less than half that of the top left corner. The aluminium object fits exactly horizontally but not vertically within the scattering voxels. There is a slight shift upwards, which results in the top of the box being extended slightly and the bottom of the box reduced due to the size of the scattering voxels. Therefore, intensity is gained in the top left corner from rays that are unattenuated by the box and is reduced in the bottom right corner as not all rays that have passed through the edge of the object are included in the intensity calculations. It is clear that the scatter estimate is very sensitive to the intensity values.

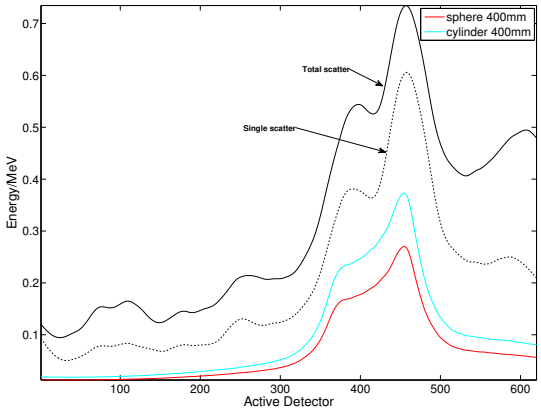

(a) Projection 0

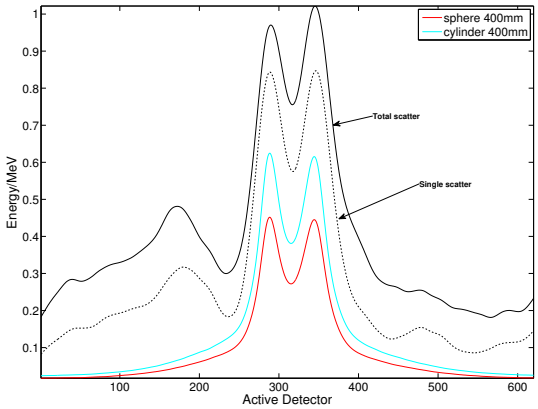

(b) Projection 256

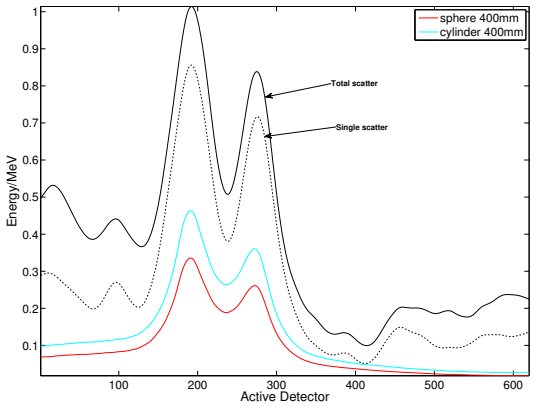

(c) Projection 512

Figure 6.29: Aluminium object in a vacuum: Scatter approximation

6.5 Water object

The water object in the test suitcase is simulated separately in air and an estimate to the scatter provided with the voxel intensities for each voxel slice displayed in Fig. 6.30. More voxels contribute to the intensity than the aluminium object as there is less attenuation through the object. Similarly to the aluminium object, the water object is shifted slightly in the y-direction and so does not fit exactly within the scattering voxels. This provides a good comparison to the large water box with a polyenergetic input x-ray spectrum.

The primary and separate scatter components obtained from the simulation are displayed in Figures 6.31, 6.32 and 6.33, and the scatter estimate displayed against the simulated scatter data are given in Fig. 6.34. Again the scatter estimate applied to a water object provides a good approximation to the single scatter element, especially for a cylinder sample. In the areas behind the object the reproduction of the total scatter component is as good as 90% in projection 0, 73% in projection 256 and 80% in projection 512. One reason for this compared to the aluminium object may be that more of the scattering voxels contribute significantly to the estimate, as it is less attenuating, and therefore it is less sensitive to errors in the intensity measurements at the edges.

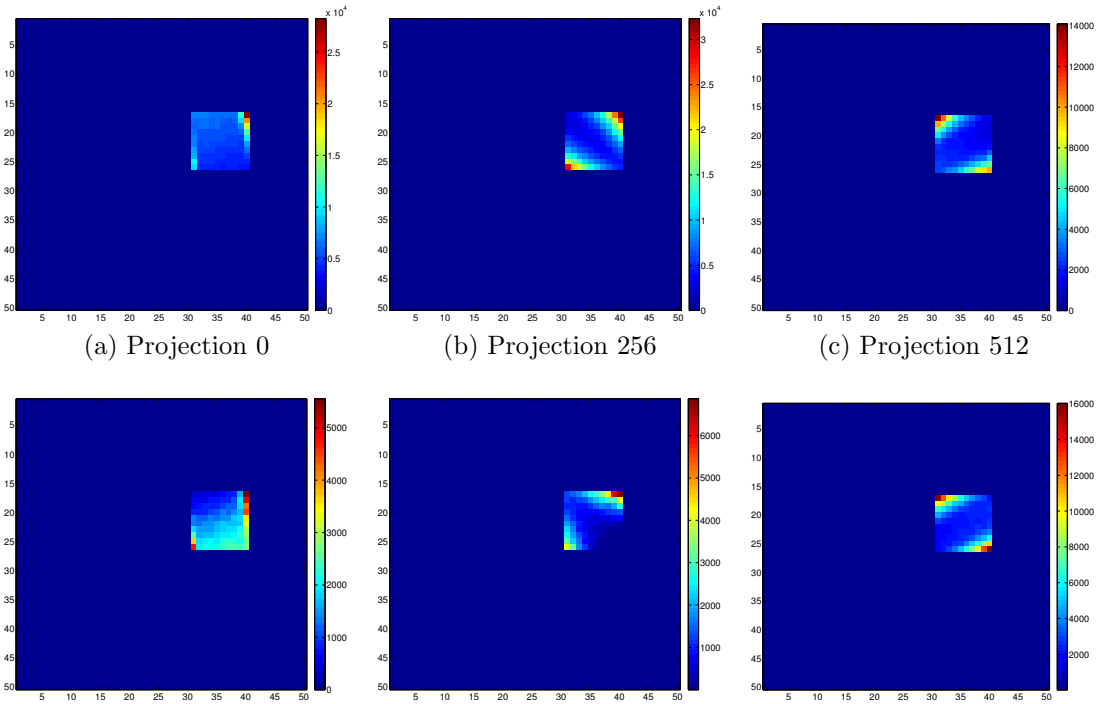

(a) Projection 0 (b) Projection 256 (c) Projection 512

(d) Projection 0 (e) Projection 256 (f) Projection 512

Figure 6.30: Water object in air: Scattering voxel intensities

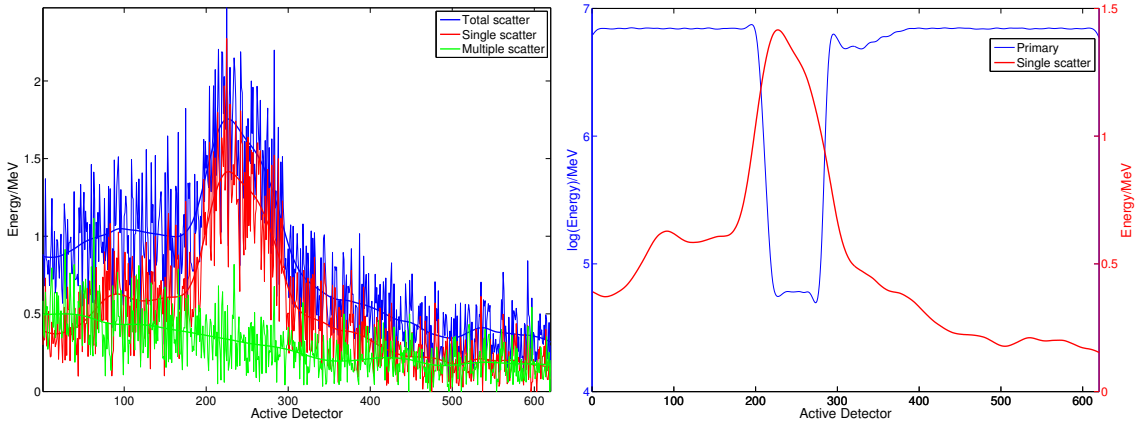

(a) Scatter and smoothed scatter (b) Primary and single scatter

Figure 6.31: Water object in air: Simulated data for source projection 0

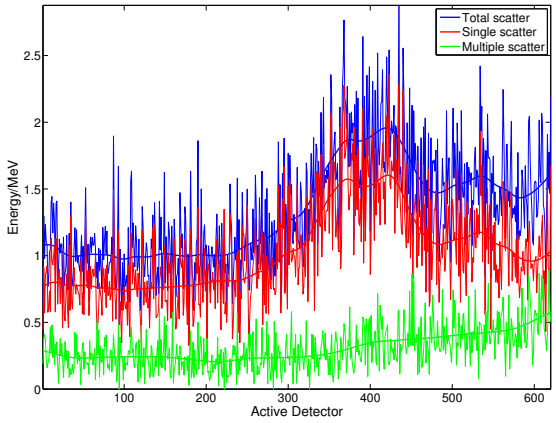

(a) Scatter and smoothed scatter

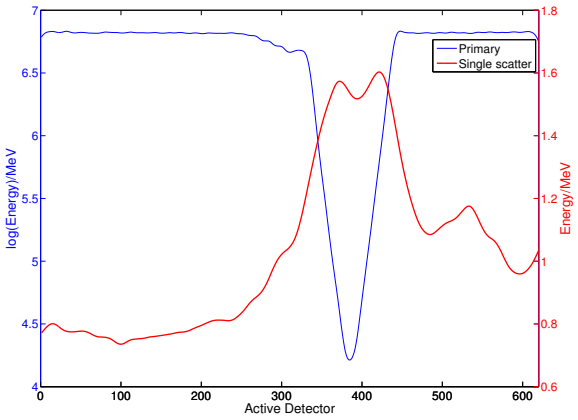

(b) Primary and single scatter

Figure 6.32: Water object in air: Simulated data for source projection 256

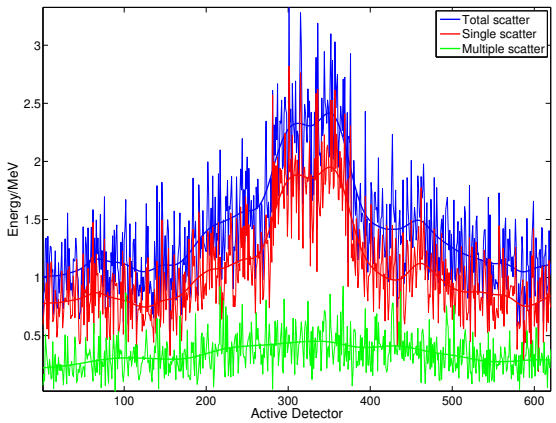

(a) Scatter and smoothed scatter

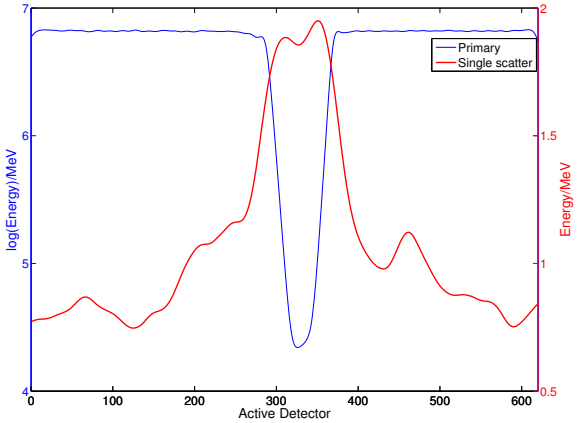

(b) Primary and single scatter

Figure 6.33: Aluminium object in air: Simulated data for source projection 512

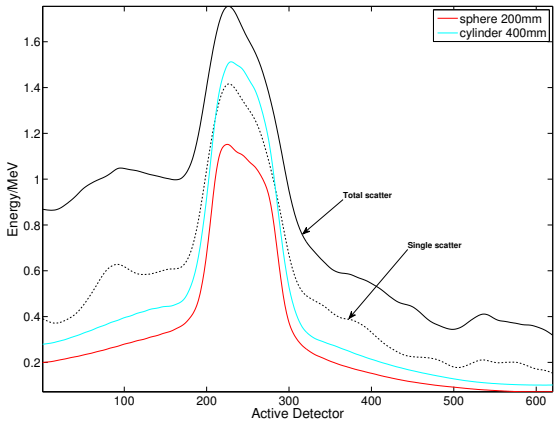

(a) Projection 0

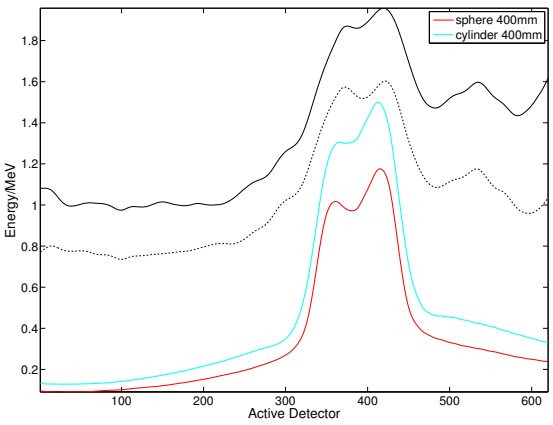

(b) Projection 256

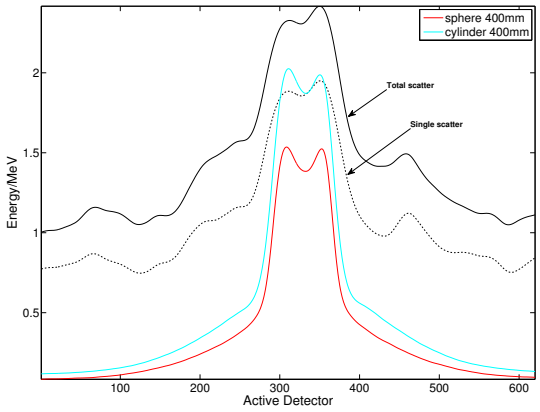

(c) Projection 512

Figure 6.34: Water object in air: Scatter approximation

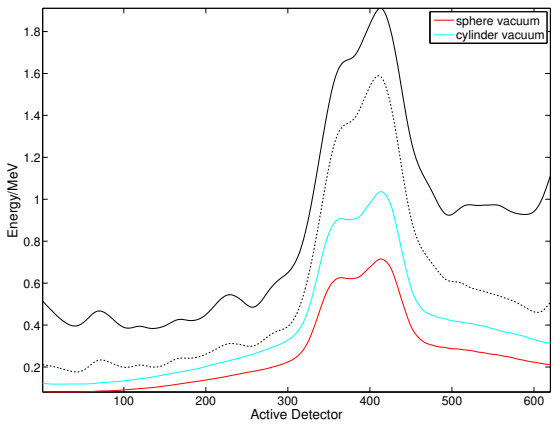

(a) Projection 48

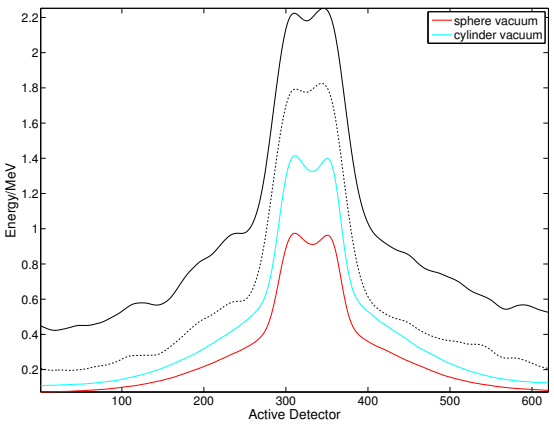

(b) Projection 96

Figure 6.35: Water object in a vacuum: Scatter approximation

6.6 Steel and lead objects

The steel and lead objects are expected to have a low scattered component as they are both highly attenuating objects. This results in only a low number of scattered photons escaping the object after scattering, particularly for lead which has a low forward scatter distribution. The voxel intensities in the area of the object are shown for voxel slices two and three in Fig. 6.36 for steel and for voxel slice two in Fig. 6.37 for lead. Very few of the voxels contribute a significant intensity in either case. Fig.6.38 displays the simulation results for the steel object. The scatter component is low but has a clearly defined distribution, and the primary beam is similarly low in the area behind the object. This leads to a high scatter-to-primary ratio and so it is important to obtain a good approximation to the scatter component for the steel object.

However, since the estimate is very sensitive to the intensity values and the objects do not fit within the scattering voxels, this leads to a very bad approximation, Fig. 6.38. Another effect that must be considered here is beam hardening. The low energy photons are preferentially absorbed and so there will be a shift in the spectrum of energies at points within the object. The scatter distributions at each energy must be multiplied by the fraction of photons that are present at that energy, $N(E)$, where E, in this case, is given in 10keV energy bins. Photoabsorption is the dominant effect in steel up to energies of over 110keV when Compton scatter becomes the dominant process. Therefore, the scatter distributions for steel increase with increasing energy.

Fig. 6.40 examines the change in the scatter estimate, for projection 256, by setting $N(E)$ at lower energies of E to be zero. The results are displayed for spectrums shifted to 100, 110, 120 and 130keV. The increase in the scatter estimate is clear, leading to a decrease of scatter by 25% in the area behind the object.

Fig. 6.41 displays the scatter contribution of the lead object in air and in a vacuum. As can be seen the lead object contributes barely any scatter to the image. It is therefore unnecessary to include the lead object in the scatter estimate.

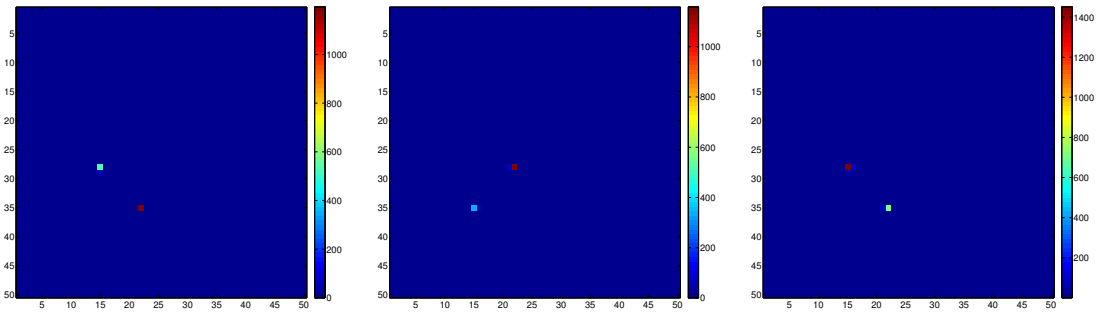

(a) Projection 0 (b) Projection 256 (c) Projection 512

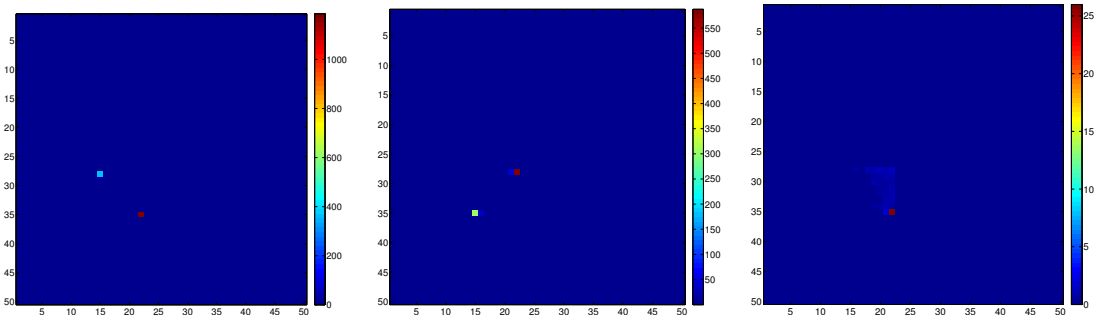

(d) Projection 0 (e) Projection 256 (f) Projection 512

Figure 6.36: Steel object in air: Scattering voxel intensities

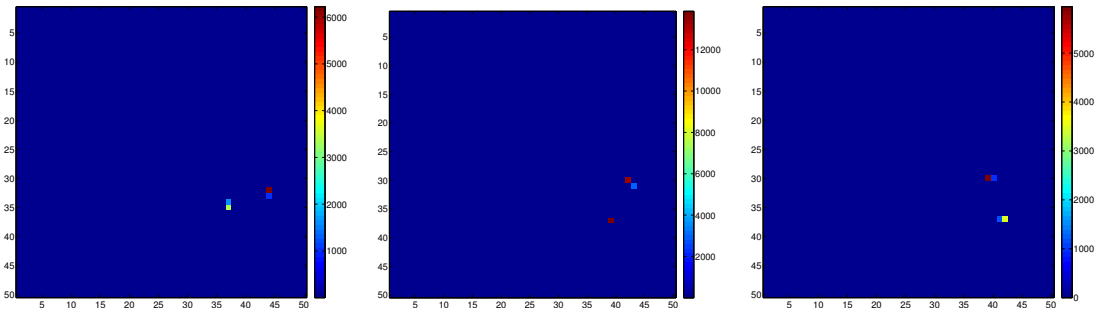

(a) Projection 0 (b) Projection 256 (c) Projection 512

Figure 6.37: Lead object in air: Scattering voxel intensities

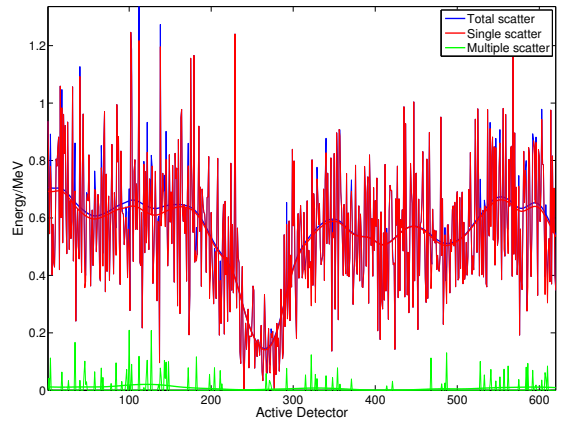

(a) Projection 256

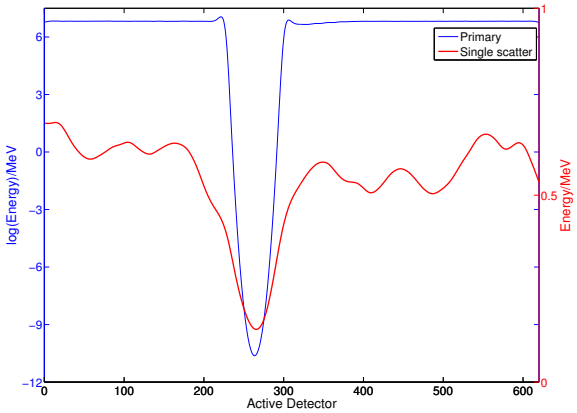

(b) Projection 256

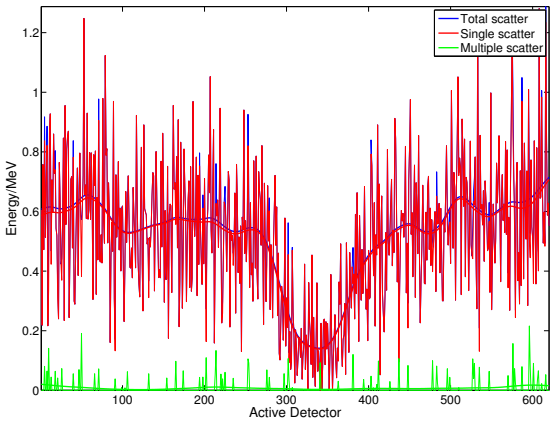

(c) Projection 512

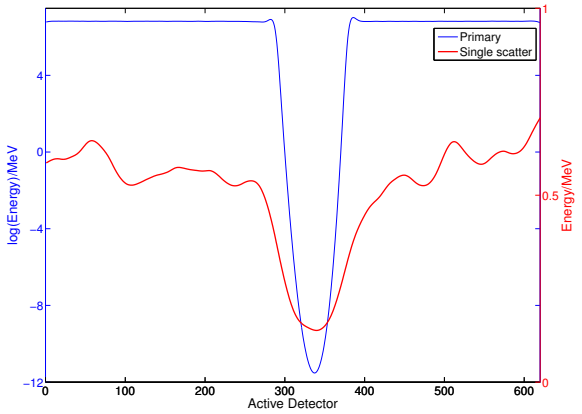

(d) Projection 512

Figure 6.38: Steel object in air: Simulated and smoothed scatter data

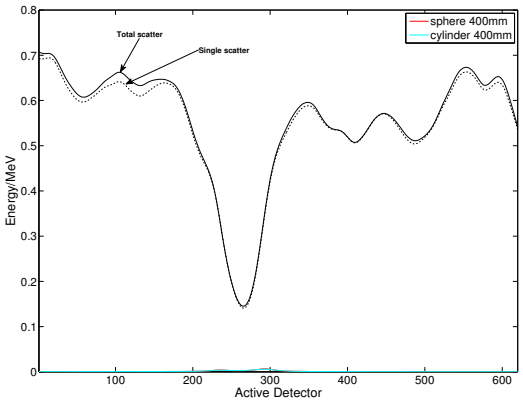

(a) Projection 256

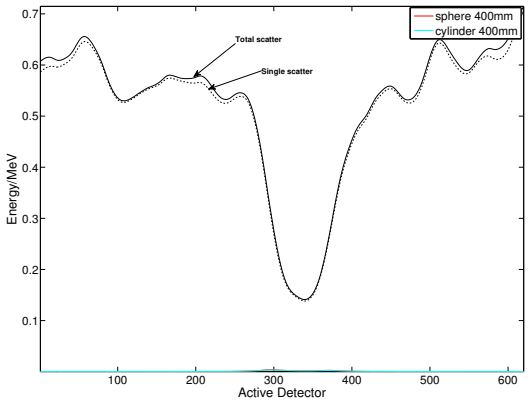

(b) Projection 512

Figure 6.39: Steel object in a air: Scatter approximation

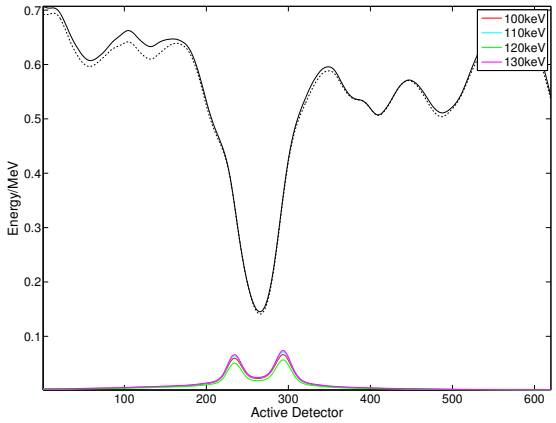

(a) Projection 256

Figure 6.40: Steel object in a air: Scatter estimate with the input spectrum shifted to higher energies

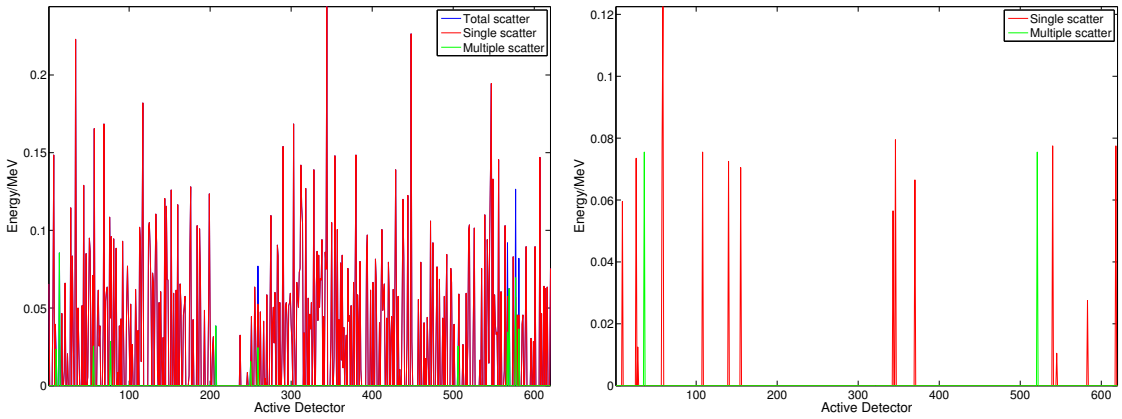

(a) Scatter in air

(b) Scatter in a vacuum

Figure 6.41: Lead object: Simulated scatter component in air and in a vacuum

6.7 Summary

In summary, the correction method is very sensitive to the intensity values, I_v, especially for highly attenuating objects where few scatter voxels contribute significantly to the scatter component. Inconsistencies in the true shape of the objects and the approximated shape of the objects cause errors in these intensity measurements, as well as inaccuracies in the calculation of the voxel shadows on the detector rings. However, even though the method needs further refinement, it has been shown to behave well in certain situations and provides the basis for a good scatter correction method.

Reconstructions were performed on both the water box and test suitcase simulated data, before and after scatter removal, using a conjugate gradient least squares method. Although the scatter estimate was good for the water box, the primary energy recorded in the detectors behind the object was still high, compared to the scatter, leading to a very low scatter to primary ratio. This was due to the high energy monoenergetic initial photon energies used in the simulation, with the intention of removing beam hardening effects. Therefore, when a reconstruction was performed, after subtracting the estimated scatter signal from the simulated data, the difference in reconstructed values was negligible showing no significant improvement.

When a reconstruction was performed on the test suitcase data the solution did not converge. Since the input spectrum is polyenergetic, and there are more highly scattering objects than the water box, this does provide high scatter to primary ratios in areas behind highly attenuating objects. However, since the recorded signal is low and only every fourth source projection is simulated, this does not provide enough information to determine a unique solution. More processing power would be required to perform a full revolution of the system for every source projection, as the current data took many weeks to acquire over multiple processors. For these reasons, unfortunately, no reconstructions can be provided.

In the following Chapter, conclusions of the work throughout this thesis and ideas for further work are presented.

Chapter 7

Conclusions and Further Work

Throughout this thesis, scattered radiation in a switched source multi-ring detector CT machine, with no detector collimation, has been investigated. Scattered radiation was shown to contribute significantly to the measured data in areas behind large objects where the measured primary signal was low. The results of the scatter investigation, based on simulated data, demonstrated the significant increase in detected x-ray scatter when moving from fan beam to cone beam imaging systems.

An overview of scatter correction methods in x-ray CT was given, which concluded that current methods were not suited to airport applications or the correction methods were slow and impractical. A new, faster scatter correction method has been proposed, whereby the scatter component is estimated in each detector, per projection, by summing the contribution of scatter from computerised $1cm^3$ voxels of the image.

The method was applied to two test objects, a homogeneous water box simulated with a monoenergetic spectrum and a test suitcase simulated with a polyenergetic spectrum. A good approximation to the single scatter component of the water box was found, where greater than 60% of the total scatter signal was reproduced. When the method was applied to the test suitcase, the reproduced signal was less than 20% of the simulated scatter data. When then method was applied to simulated data of the internal objects with the suitcase removed, the estimate was much improved showing that the assumption that low scatter voxels could be ignored is invalid.

The scatter estimate was very sensitive to the voxel intensities, which were incorrect due to the approximations of the shape of the objects and inaccuracies of the voxel shadows. The investigation into the proposed scatter correction method is by no means complete, but initial tests indicate that the method could be significantly improved with refinement. The following section presents some ideas of how the results could be improved.

7.1 Further work

One idea for further work is to differ the size of the scattering voxels over each scattering region. Smaller voxels at the object edges, so that the object shapes are better approximated, would remove some of the intensity errors whilst reducing the minimum size of a scattering object. Similarly, larger scatter voxels could be used to add the contribution of scatter from the low scattering cotton component, without increasing the computation time significantly. Better approximation of the voxel shadows would equally remove intensity errors.

To remove beam hardening effects, the spectrum of energies, $\bar{I}_p$, could differ depending on the scattering material. This involves analysing the primary beam spectrum detected in the scatter distributions for the different materials. More objects of differing shapes and sizes need to be simulated in order to test the method further.

In terms of speed, the algorithm is by no means optimised. In it's current form, all solid angles for each voxel-detector pair and all scatter angles for each voxel-detector pair in each projection are read in from file. By grouping together small changes in angles this would significantly reduce computation time. A reconstruction before and after scatter removal should be performed, given more time and processing power, to prove the effectiveness of the algorithm.

In the long term, with developments in computer processing power, the Geant4 Monte Carlo simulation could be implemented within the reconstruction loop providing scatter correction alongside the reconstruction. First, a reconstruction is required to approximate the attenuation coefficients then this information could be fed into

a Monte Carlo simulation leading to an approximation of the scatter signal. The scatter could then be removed from the original data and another reconstruction performed on the new data providing an improved approximation to the reconstructed attenuation coefficients, with these results being fed back into the Monte Carlo simulation. A better approximation to the scattered signal could then be simulation and subtracted from the original data and so on until a scatter free image is found. Of course, significant improvements in computer processing power would be required before this was feasible in a real scenario.

Bibliography

[1] S. Agostinelli, J. Allison, K. Amako, J. Apostolakis, H. Araujo, P. Arce, M. Asai, D. Axen, S. Banerjee, G. Barrand, et al. Geant4-a simulation toolkit. *Nuclear Instruments and Methods in Physics Research-Section A Only*, 506(3):250–303, 2003.

[2] J. Allison, K. Amako, J. Apostolakis, H. Araujo, P.A. Dubois, M. Asai, G. Barrand, R. Capra, S. Chauvie, R. Chytracek, et al. Geant4 developments and applications. *IEEE Transactions on Nuclear Science*, 53(1):270–278, 2006.

[3] K. Amako, S. Guatelli, V. Ivanchencko, M. Maire, B. Mascialino, K. Murakami, L. Pandola, S. Parlati, MG Pia, M. Piergentili, et al. Validation of Geant4 electromagnetic physics versus protocol data. In *Nuclear Science Symposium Conference Record, 2004 IEEE*, volume 4, pages 2115–2119. IEEE, 2005.

[4] K. Amako, S. Guatelli, V. Ivanchencko, M. Maire, B. Mascialino, K. Murakami, L. Pandola, S. Parlati, MG Pia, M. Piergentili, et al. Geant4 and its validation. *Nuclear Physics B-Proceedings Supplements*, 150:44–49, 2006.

[5] K. Amako, S. Guatelli, V.N. Ivanchenko, M. Maire, B. Mascialino, K. Murakami, P. Nieminen, L. Pandola, S. Parlati, M.G. Pia, et al. Comparison of Geant4 electromagnetic physics models against the NIST reference data. *Nuclear Science, IEEE Transactions on*, 52(4):910–918, 2005.

[6] DS Anikonov, AE Kovtanyuk, and IV Prokhorov. *Transport equation and tomography*. Vsp, 2002.

[7] J. Apostolakis, M. Asai, AG Bogdanov, H. Burkhardt, G. Cosmo, S. Elles, G. Folger, VM Grichine, P. Gumplinger, A. Heikkinen, et al. Geometry and physics of the Geant4 toolkit for high and medium energy applications. *Radiation Physics and Chemistry*, 78(10):859–873, 2009.

[8] E. Arimondo, P.R. Berman, and C.C. Lin. *Advances in Atomic, Molecular, and Optical Physics*. Academic Press, 2009.

[9] M. Bertero and P. Boccacci. *Introduction to inverse problems in imaging*. Taylor & Francis, 1998.

[10] M. Bertram, J. Wiegert, and G. Rose. Potential of software-based scatter corrections in cone-beam volume CT. In *Proceedings of SPIE*, volume 5745, page 259, 2005.

[11] K. Binder. Applications of Monte Carlo methods to statistical physics. *Reports on Progress in Physics*, 60:487, 1997.

[12] K. Binder and D.W. Heermann. *Monte Carlo simulation in statistical physics: an introduction*. Springer, 2010.

[13] J.M. Boone and J.A. Seibert. Monte Carlo simulation of the scattered radiation distribution in diagnostic radiology. *Medical physics*, 15:713, 1988.

[14] R.N. Bracewell. *The Fourier transform and its applications*. McGraw-Hill Science/Engineering/Math, 2000.

[15] A.V. Bronnikov. Cone-beam reconstruction by backprojection and filtering. *JOSA A*, 17(11):1993–2000, 2000.

[16] H. Bruder, M. Kachelrieß, S. Schaller, K. Stierstorfer, and T. Flohr. Single-slice rebinning reconstruction in spiral cone-beam computed tomography. *Medical Imaging, IEEE Transactions on*, 19(9):873–887, 2002.

[17] K.M. Case and P.F. Zweifel. *Linear transport theory*. Addison-Wesley Pub. Co., 1967.

[18] H P Chan and K Doi. The validity of Monte Carlo simulation in studies of scattered radiation in diagnostic radiology. *Physics in Medicine and Biology*, 28:109, 1983.

[19] BK Chatterjee, SC Roy, T. Suric, LA LaJohn, and RH Pratt. Asymmetry and the shift of the Compton profile. *Nuclear Instruments and Methods in Physics Research Section A: Accelerators, Spectrometers, Detectors and Associated Equipment*, 580(1):22–24, 2007.

[20] AP Colijn and FJ Beekman. Accelerated simulation of cone beam X-ray scatter projections. *Medical Imaging, IEEE Transactions on*, 23(5):584–590, 2004.

[21] J. Coursey, D. Schwab, and R. Dragoset. Atomic Weights and Isotopic Compositions (version 2.4. 1). *National Institute of Standards and Technology, Gaithersburg, MD*, 2005.

[22] K. Cranley, BJ Gilmore, GWA Fogarty, L. Desponds, and D. Sutton. Catalogue of diagnostic x-ray spectra and other data. *IPEM Report*, 78.

[23] D.E. Cullen, J.H. Hubbell, and L. Kissel. EPDL97: The evaluated photon data library,97 version. *Lawrence Livermore National Laboratory Report No. UCRL-50400*, 1997.

[24] M. Defrise, F. Noo, and H. Kudo. Rebinning-based algorithms for helical cone-beam CT. *Physics in Medicine and Biology*, 46:2911, 2001.

[25] M. Endo, T. Tsunoo, N. Nakamori, and K. Yoshida. Effect of scattered radiation on image noise in cone beam CT. *Medical Physics*, 28:469, 2001.

[26] A. Faridani et al. Introduction to the mathematics of computed tomography. *Inside Out: Inverse Problems and Applications*, 47:1–46, 2003.

[27] LA Feldkamp, LC Davis, and JW Kress. Practical cone-beam algorithm. *Journal of the Optical Society of America A*, 1(6):612–619, 1984.

[28] GH Glover. Compton scatter effects in CT reconstructions. *Medical Physics*, 9:860, 1982.

[29] W.R. Hendee and R. Stanton. The physical principles of computed tomography. *Physics Today*, 37:68, 1984.

[30] GT Herman. Image reconstruction from projections. *Real-Time Imaging*, 1(1):3–18, 1995.

[31] G.N. Hounsfield. Computerized transverse axial scanning (tomography): Part 1. Description of system. *British Journal of Radiology*, 46(552):1016, 1973.

[32] F. James. A review of pseudorandom number generators. *Computer Physics Communications*, 60(3):329–344, 1990.

[33] PC Johns and M. Yaffe. Scattered radiation in fan beam imaging systems. *Medical Physics*, 9:231, 1982.

[34] P.M. Joseph and R.D. Spital. The effects of scatter in x-ray computed tomography. *Medical physics*, 9:464, 1982.

[35] A.C. Kak and M. Slaney. Principles of computerized tomographic imaging. 1988.

[36] W. Kalender. Monte Carlo calculations of x-ray scatter data for diagnostic radiology. *Physics in Medicine and Biology*, 26:835, 1981.

[37] W.A. Kalender. *Computed Tomography: Fundamentals, System Technology, Image Quality, Applications*. Publicis MCD Verlag, 2000.

[38] H. Kanamori, N. Nakamori, K. Inoue, and E. Takenaka. Effects of scattered X-rays on CT images. *Physics in Medicine and Biology*, 30:239, 1985.

[39] A. Katsevich. Analysis of an exact inversion algorithm for spiral cone-beam CT. *Physics in Medicine and Biology*, 47:2583, 2002.

[40] A. Katsevich. Theoretically exact filtered backprojection-type inversion algorithm for spiral CT. *SIAM Journal on Applied Mathematics*, 62(6):2012–2026, 2002.

[41] A. Katsevich. An improved exact filtered backprojection algorithm for spiral computed tomography* 1. *Advances in Applied Mathematics*, 32(4):681–697, 2004.

[42] R.M. Kippen. The GEANT low energy Compton scattering (GLECS) package for use in simulating advanced Compton telescopes. *New Astronomy Reviews*, 48(1-4):221–225, 2004.

[43] H. Kudo, T. Rodet, F. Noo, and M. Defrise. Exact and approximate algorithms for helical cone-beam CT. *Physics in Medicine and Biology*, 49:2913, 2004.

[44] Y. Kyriakou, T. Riedel, and W.A. Kalender. Combining deterministic and Monte Carlo calculations for fast estimation of scatter intensities in CT. *Physics in Medicine and Biology*, 51:4567, 2006.

[45] A. Lechner, A. Mantero, M.G. Pia, and M. Sudhakar. Validation of Geant4 X-ray fluorescence transitions-validation of Geant4 electromagnetic models against calorimetry measurements in the energy range up to 1 MeV. In *Nuclear Science Symposium Conference Record, 2008. NSS'08. IEEE*, pages 2869–2876. IEEE, 2009.

[46] W.R. Leo. *Techniques for nuclear and particle physics experiments: a how-to approach*. Springer Verlag, 1994.

[47] L.A. Love and R.A. Kruger. Scatter estimation for a digital radiographic system using convolution filtering. *Medical physics*, 14:178, 1987.

[48] JS Maltz, B. Gangadharan, S. Bose, DH Hristov, BA Faddegon, A. Paidi, and AR Bani-Hashemi. Algorithm for X-ray scatter, beam-hardening, and beam profile correction in diagnostic (kilovoltage) and treatment (megavoltage) cone beam CT. *IEEE transactions on medical imaging*, 27(12):1791, 2008.

[49] M.F. Modest. *Radiative heat transfer*. Academic Pr, 2003.

[50] F. Natterer. *The mathematics of computerized tomography*. Society for Industrial Mathematics, 2001.

[51] R. Ning, X. Tang, and D. Conover. X-ray scatter correction algorithm for cone beam CT imaging. *Medical Physics*, 31:1195, 2004.

[52] B. Ohnesorge, T. Flohr, and K. Klingenbeck-Regn. Efficient object scatter correction algorithm for third and fourth generation CT scanners. *European Radiology*, 9(3):563–569, 1999.

[53] E.T. Quinto. An introduction to X-ray tomography and Radon transforms. *The radon transform, inverse problems, and tomography: American Mathematical Society short course, January 3-4, 2005, Atlanta, Georgia*, 63:1, 2006.

[54] J. Radon. On the determination of functions from their integral values along certain manifolds. *Medical Imaging, IEEE Transactions on*, 5(4):170–176, 2007.

[55] DE Raeside. Monte Carlo principles and applications. *Physics in Medicine and Biology*, 21:181, 1976.

[56] R. Ribberfors. Relationship of the relativistic Compton cross section to the momentum distribution of bound electron states. *Physical Review B*, 12(6):2067–2074, 1975.

[57] J. Rinkel, L. Gerfault, F. Esteve, and JM Dinten. A new method for x-ray scatter correction: first assessment on a cone-beam CT experimental setup. *Physics in Medicine and Biology*, 52:4633, 2007.

[58] I. Sabo-Napadensky and O. Amir. Reduction of scattering artifact in multislice CT. In *Proceedings of SPIE*, volume 5745, page 983, 2005.

[59] G.B. Saha. *Physics and radiobiology of nuclear medicine*. Springer Verlag, 2006.

[60] J.H. Siewerdsen and D.A. Jaffray. Cone-beam computed tomography with a flat-panel imager: Magnitude and effects of x-ray scatter. *Medical physics*, 28:220, 2001.

[61] L. Spies, M. Ebert, BA Groh, BM Hesse, and T. Bortfeld. Correction of scatter in megavoltage cone-beam CT. *Physics in Medicine and Biology*, 46:821, 2001.

[62] William Thompson. *Source firing patterns and reconstruction algorithms for a switched source offset detector CT machine.* PhD in applied mathematics, of Mathematics University of Manchester, 2011.

[63] H.K. Tuy. An inversion formula for cone-beam reconstruction. *SIAM Journal on Applied Mathematics*, 43(3):546–552, 1983.

[64] G. Wang, T.H. Lin, P. Cheng, and DM Shinozaki. A general cone-beam reconstruction algorithm. *Medical Imaging, IEEE Transactions on*, 12(3):486–496, 2002.

[65] J. Wiegert, M. Bertram, G. Rose, and T. Aach. Model based scatter correction for cone-beam computed tomography. In *Proceedings of SPIE*, volume 5745, page 271, 2005.

[66] WSC Williams. Nuclear and particle physics. 1991.

[67] W. Zbijewski and F.J. Beekman. Efficient Monte Carlo based scatter artifact reduction in cone-beam micro-CT. *Medical Imaging, IEEE Transactions on*, 25(7):817–827, 2006.

[68] L. Zhu, N. Strobel, and R. Fahrig. X-ray scatter correction for cone-beam CT using moving blocker array. In *Proceedings of SPIE*, volume 5745, page 251, 2005.

Appendix A

Example Code

The following code is the user defined Event Action class for the Geant4 Monte Carlo simulation of the RTT80 machine.

```
#include "G4Timer.hh"
#include "cxrModel_v20EventAction.hh"
#include "cxrModel_v20PrimaryGeneratorAction.hh"
#include "cxrModel_v20RunAction.hh"
#include "cxrModel_v20DetectorConstruction.hh"
#include "cxrModel_v20SensorsHit.hh"
#include "cxrModel_v20Histogram.hh"
#include "logFile.hh"

#include "G4Event.hh"
#include "G4EventManager.hh"
#include "G4HCofThisEvent.hh"
#include "G4VHitsCollection.hh"
#include "G4TrajectoryContainer.hh"
#include "G4Trajectory.hh"
#include "G4VVisManager.hh"
#include "G4SDManager.hh"
#include "G4UImanager.hh"
#include "G4UnitsTable.hh"
#include "G4ios.hh"
#include "G4RunManager.hh"
#include <fstream>
using namespace std;


cxrModel_v20EventAction::cxrModel_v20EventAction
```

```
(cxrModel_v20DetectorConstruction* DET, G4bool separateScatter):
                                                        detCon(DET)
{
 // timer
 RunTimer = new G4Timer();
 time = 0.0;
 scatter = separateScatter;

}

cxrModel_v20EventAction::~cxrModel_v20EventAction()
{
 delete  RunTimer;
 delete [] sensorsCollID;
}


void cxrModel_v20EventAction::BeginOfEventAction(const G4Event*)
{
 // Give each active detector a collection ID
 // for managing hit counts
 static G4int count = 0;

 if (count == 0)
 {
   noOfDetRings = detCon->GetNoOfDetRings();
   G4cout << "***noOfDetRings in eventAction****"
                                    << noOfDetRings << G4endl;

   sensorsCollID = new G4int[noOfDetRings][softDetsIn];

   char cxrColName[40];
   SDman = G4SDManager::GetSDMpointer();

   for (G4int k = 0; k < noOfDetRings; k++)
   {
     for (G4int i = 0; i < softDetsIn; i++)
     {
       sensorsCollID[k][i] = 0;
       sprintf(cxrColName,"cxrSDet%d/cxrDetCol",i+(k*softDetsIn));
       sensorsCollID[k][i] = SDman->GetCollectionID
                                       ((G4String)cxrColName);
     }
   }

 }
```

```
 totalE = 0.;
 RunTimer->Start();
 count++;
}


void cxrModel_v20EventAction::EndOfEventAction
                                      (const G4Event* evt)
{
 HCE = evt->GetHCofThisEvent();//point to event
 //CHC initialised for hits collection
 cxrModel_v20SensorsHitsCollection* CHC = 0;

 //set up pointers to enable use of histogramming
 pRunManager = G4RunManager::GetRunManager();
 pRunAction = (cxrModel_v20RunAction*)(pRunManager
                                          ->GetUserRunAction());
 G4bool histogram = pRunAction->histogram;


 /* Collect hits information for histogramming.  Options are:
    (1) Total energy all processes combined
    (2) Total energy for separate processes
    (3) Histogrammed hits all processes combined
    (4) Histogrammed hits of each process separately
 */
 if(scatter)//separate scatter
 {
   for (G4int k = 0; k < noOfDetRings; k++)
   {
     for (G4int i = 0; i < softDetsIn; i++)
     {
       // Find the number of hits for each process
       G4int noScatter = noOfHits[k*softDetsIn+i][0];
       G4int compton = noOfHits[k*softDetsIn+i][0]
                             + noOfHits[k*softDetsIn+i][1];
       G4int rayleigh = noOfHits[k*softDetsIn+i][2] + compton;
       G4int msc = noOfHits[k*softDetsIn+i][3] + rayleigh;

       // Get hit count of the event
       if (HCE) CHC = (cxrModel_v20SensorsHitsCollection*)(HCE
                                    ->GetHC(sensorsCollID[k][i]));
       if (CHC)
       {
         G4int nHit = CHC->entries();
         if (nHit > 0)
         {
```

```
G4double totalE;

if (noOfHits[k*softDetsIn+i][0] > 0)
{
  totalE = 0;

  for (G4int j = 0; j < noScatter; j++)
  {
    if(histogram)
    {
      totalE = (*CHC)[j]->GetEdep();
      pRunAction->energyHistogram[k][i]
                          ->histogramTheData(totalE);
      totalE = 0;
    }
    else totalE += (*CHC)[j]->GetEdep();
  }
  if (!histogram) pRunAction->energyHistogram[k][i]
                          ->totalDetectorEnergy(totalE);
}

if (noOfHits[k*softDetsIn+i][1] > 0)
{
  totalE = 0;
  for (G4int j = noScatter; j < compton; j++)
  {
    if(histogram)
    {
      totalE = (*CHC)[j]->GetEdep();
      pRunAction->comptonHistogram[k][i]
                             ->histogramTheData(totalE);
      totalE = 0;
    }
    else{  totalE += (*CHC)[j]->GetEdep();
    }

  }
  if(!histogram) pRunAction->comptonHistogram[k][i]
                           ->totalDetectorEnergy(totalE);
}

if (noOfHits[k*softDetsIn+i][2] > 0)
{
  totalE = 0;
  for (G4int j = compton; j < rayleigh; j++)
  {
    if(histogram)
```

```
              {
                totalE = (*CHC)[j]->GetEdep();
                pRunAction->rayleighHistogram[k][i]
                                  ->histogramTheData(totalE);
                totalE = 0;
              }
              else totalE += (*CHC)[j]->GetEdep();
            }
            if(!histogram) pRunAction->rayleighHistogram[k][i]
                                  ->totalDetectorEnergy(totalE);
          }

          if (noOfHits[k*softDetsIn+i][3] > 0)
          {
            totalE = 0;
            for (G4int j = rayleigh; j < msc; j++)
            {
              if(histogram)
              {
                totalE = (*CHC)[j]->GetEdep();
                pRunAction->mscHistogram[k][i]
                                    ->histogramTheData(totalE);
                totalE = 0;
              }
              else totalE += (*CHC)[j]->GetEdep();
            }
            if(!histogram) pRunAction->mscHistogram[k][i]
                                  ->totalDetectorEnergy(totalE);
          }

        }
      }
    }
  }
}
// All process data collected together
else
{
  for (G4int k = 0; k < noOfDetRings; k++)
  {
    for (G4int i = 0; i < softDetsIn; i++)
    {
      totalE = 0;
      if (HCE) CHC = (cxrModel_v20SensorsHitsCollection*)(HCE
                                  ->GetHC(sensorsCollID[k][i]));
      if (CHC)
      {
```

```
        G4int nHit = CHC->entries();
        if (nHit > 0)
        {
          for (G4int ii = 0; ii < nHit; ii++)
          {
            if(histogram)
            {
              totalE = (*CHC)[ii]->GetEdep();
              pRunAction->energyHistogram[k][i]
                                        ->histogramTheData(totalE);
              totalE = 0;
            }
            else totalE += (*CHC)[ii]->GetEdep();
          }
          if (!histogram) pRunAction->energyHistogram[k][i]
                                      ->totalDetectorEnergy(totalE);

        }
      }
    }
  }
}

if(scatter)
{
  for (G4int k = 0; k < noOfDetRings; k++)
  {
    for (G4int i = 0; i < softDetsIn; i++)
    {
      for (G4int j = 0; j < 4; j++)
      {
        noOfHits[k*softDetsIn + i][j] = 0;
      }
    }
  }
}

//activate the timer
event_id = evt->GetEventID();
RunTimer->Stop();
time += (RunTimer->GetRealElapsed() / (G4double)60.0);
time_mins = (G4int)time;
time_seconds = (G4int)((time - (G4double)time_mins)*(G4double)60);

if ((event_id+1)%10 == 0)
{
  G4cout << (event_id + 1) << " events completed in "
```

```
              << time_mins << " minutes "<< time_seconds
                        << " seconds." << G4endl;

   char theTime[200];
   logFile *myRecord = new logFile();
   fetchedName = pRunAction->GetLogFileName();
   myRecord->PublicSetLogName(fetchedName);
   sprintf(theTime,
          "Event Id: %d Real elapsed time: %d mins, %d secs",
                           event_id, time_mins, time_seconds);
   myRecord->AppendLogFile( &theTime[0]);
   delete myRecord;
 }

}

void cxrModel_v20EventAction::SetNoOfDetHits
                                     (G4int (*hits)[4], G4int stage)
{

 G4int j = stage;

 // Get hit counts for each process from stacking action
 if(!noOfHits)
 {
   noOfHits = new G4int[noOfDetRings*softDetsIn][4];
   for (G4int k = 0; k < noOfDetRings; k++)
   {
     for (G4int i = 0; i < softDetsIn; i++)
     {
       for(G4int j = 0; j < 4; j++)
       {
         noOfHits[k*softDetsIn + i][j] = 0;
       }
     }
   }
 }

 for (G4int k = 0; k < noOfDetRings; k++)
 {
   for (G4int i = 0; i < softDetsIn; i++)
   {
     noOfHits[k*softDetsIn + i][j] = hits[k*softDetsIn+i][j];
   }
 }

}
```

Appendix B

Additional Results

Additional results are displayed here for the water box and test suitcase. Specifically, they show the scatter estimate against the simulated scatter data for alternative source projections.

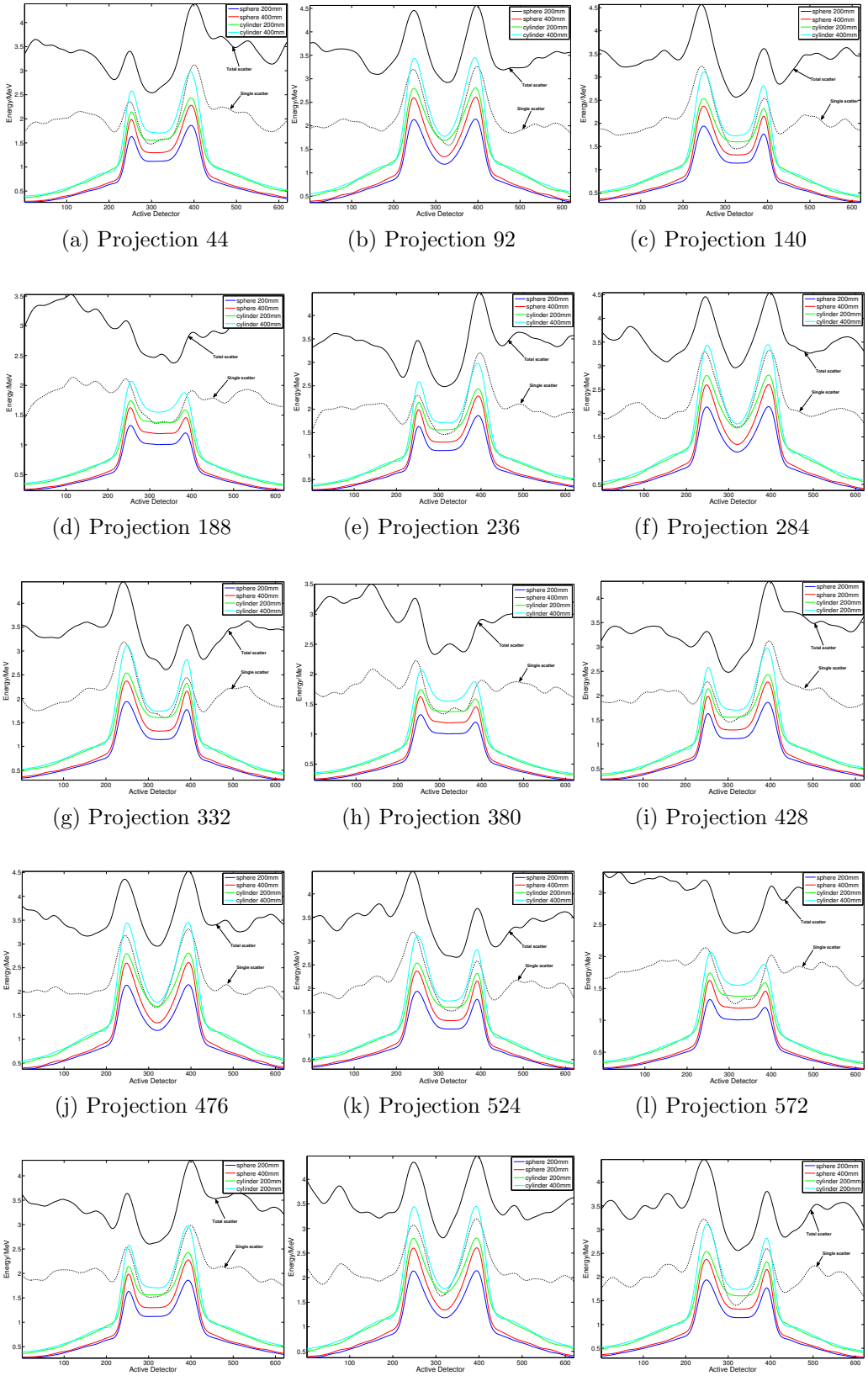

(a) Projection 44 (b) Projection 92 (c) Projection 140

(d) Projection 188 (e) Projection 236 (f) Projection 284

(g) Projection 332 (h) Projection 380 (i) Projection 428

(j) Projection 476 (k) Projection 524 (l) Projection 572

(m) Projection 620 (n) Projection 668 (o) Projection 716

Figure B.1: Water box: Scatter approximation for different projections

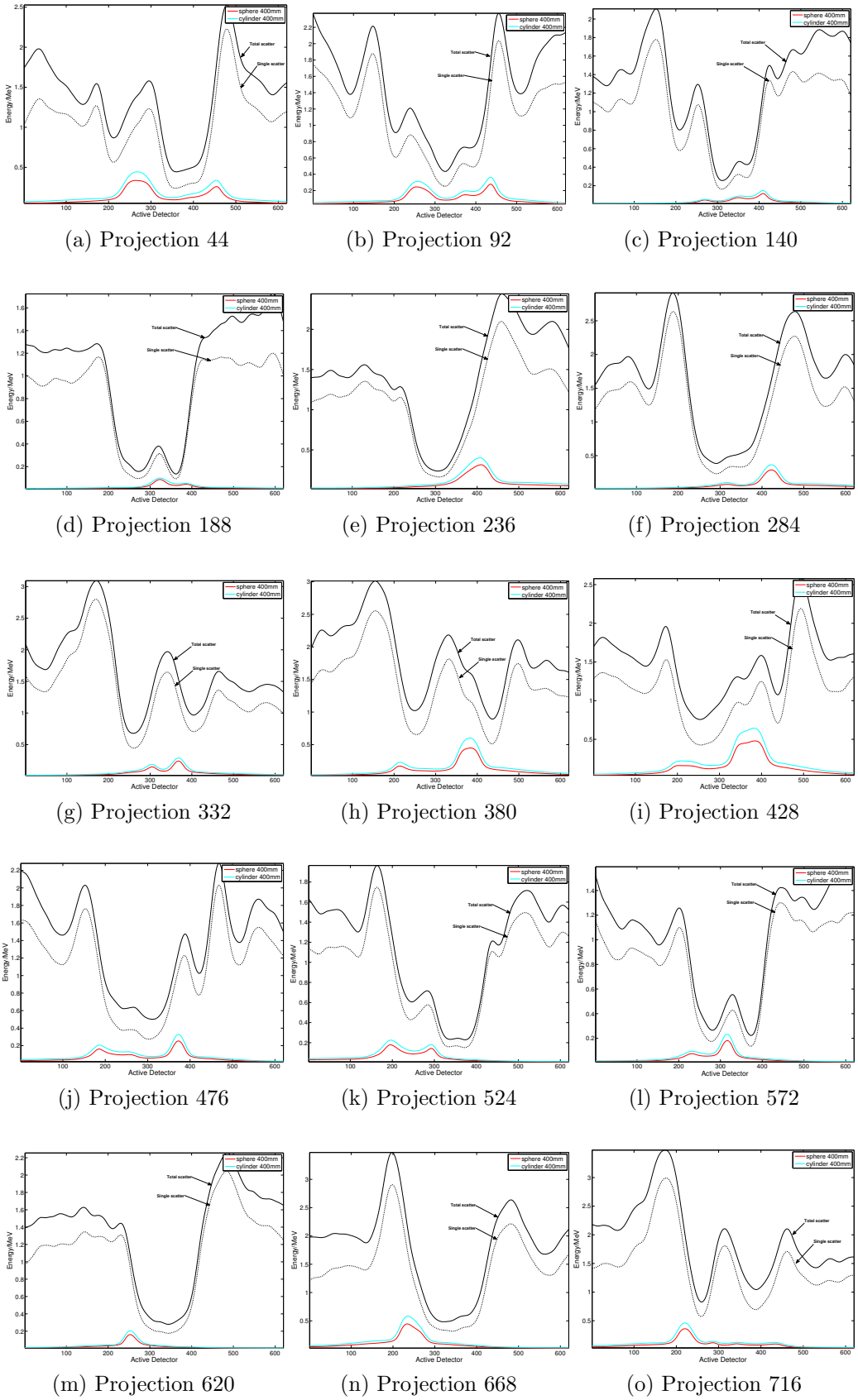

(a) Projection 44 (b) Projection 92 (c) Projection 140

(d) Projection 188 (e) Projection 236 (f) Projection 284

(g) Projection 332 (h) Projection 380 (i) Projection 428

(j) Projection 476 (k) Projection 524 (l) Projection 572

(m) Projection 620 (n) Projection 668 (o) Projection 716

Figure B.2: Test suitcase: Scatter approximation for different projections